



Novel approaches to topological order involving open boundaries in closed and open quantum systems

Der Fakultät für Mathematik und Physik
der Gottfried Wilhelm Leibniz Universität Hannover
zur Erlangung des akademischen Grades

Doktor der Naturwissenschaften
Dr. rer. nat.

genehmigte Dissertation von

M.Sc. Amit Jamadagni Gangapuram

2021

Referent : Priv.-Doz. Dr. Hendrik Weimer
Korreferenten : Prof. Dr. Tobias J. Osborne
: Prof. Dr. Roman Orus
Tag der Promotion : 29.01.2021

Abstract

The fundamental understanding of phases and their transitions has been a central theme in condensed matter physics. Until recently, it was largely believed that the Landau symmetry breaking principle was effective in distinguishing different phases of matter, with broken symmetries signaling the phase transition. But with the discovery of topological phases which are beyond the Landau symmetry breaking principle, the identification and classification of quantum phases at absolute zero has opened up new unexplored avenues thus leading to exciting theoretical discoveries further propelling technological advancement. Topological phases of matter are characterized by the notion of topological order and in this work we aim to explore and understand topological phases by introducing novel signatures which characterize topological order. The robustness of these phases to external perturbation makes them an ideal candidate to store and manipulate quantum information thus making them an unique and interesting prospect for realizing quantum computers.

There have been several signatures to characterize intrinsic topological order, for instance the invariance of the topologically ordered state under local operators, the dependence of ground state degeneracy on the underlying manifold and its robustness to external perturbation, topological entanglement entropy related to the quantum dimension of the supers-selection sectors, the inability to construct the topologically ordered state from a product state via constant depth unitary transformations. With toric code as the toy model, we analyze the robustness of topological order on a manifold supporting open boundaries by computing some of the above signatures which effectively detect a topological to trivial phase transition. We then probe the existence of a quantum criticality between distinct topological phases obtained by varying the underlying manifold. In these scenarios, most of the above signatures turn out to be ineffective in detecting the distinct phases leading to the introduction of a non-local order parameter whose construction is facilitated by the phenomenon of anyon condensation.

The signatures for quantitatively and qualitatively characterizing intrinsic topological order being highly scenario dependent and also with its definition for mixed states being elusive we introduce an operational definition based on concepts of topological error correction. We define a state to be topologically ordered if the errors in the state can be corrected by an error correction circuit of finite depth. To concretize the notion of topological to trivial

phase transition in an open setting we turn to nonequilibrium phenomenon, for example: Directed Percolation, with the change in percolation rate driving a dynamical phase transition between absorbing and active states with the former being topologically ordered while the latter being topologically trivial. Additionally, we explore the notion of topological phase transitions between distinct topological phases obtained by varying underlying topology in an open setting, analogous to the closed setting discussed earlier. To summarize, we have introduced various mixed states which exhibit topological order and also an operational definition to quantify topological order applicable across multitude of scenarios.

We extend the above operational definition to quantify and detect quantum phase transitions in the case of Symmetry Protected Topological (SPT) phases. To further validate the above notion, we consider the perturbed variants of the Su-Schrieffer-Heeger (SSH) models and detect quantum phase transitions to a high accuracy by employing the techniques from the framework of tensor networks. It is significant to note the distinction of the error correction algorithms applied earlier in the case of intrinsic topological order were independent of symmetry constraints while in the current scenario we impose additional symmetry constraints to accurately detect the phase transition. In addition, we also devise error correction strategies with respect to topologically trivial states to detect quantum phase transitions which do not involve topological phases. This gives rise to a very fundamental question on whether error correction statistics with a well defined error correction algorithm, not necessarily optimal, are capable of detecting a equivalence classes of phases and thereby acting as a reliable probe to effectively detect topological/quantum phase transitions?

From theoretical and numerical end of the spectrum we shift gears to explore possible experimental platforms with an aim to realize some of the quantum many-body phenomenon discussed earlier. While there have been several innovative experimental avenues to realize the above, one such promising candidate has been ultracold polar molecules setups that offer additional degrees of freedom due to the ro-vibrational degrees of freedom. Based on the chemical reaction between atoms and molecules which results in a quantum Zeno-based blockade, we devise several optimal strategies to efficiently detect molecules using atom as probe, we further extend the above technique to entangle the internal states of molecules and atoms. In addition, we also present optimal strategies for dissipative state engineering using the atom-molecule interactions.

Keywords

Topological Order

Quantum Phase Transitions

Topological Quantum Phase
Transitions

Open Quantum Systems

Quantum Error Correction

Symmetry Protected Topo-
logical Phases

Ultra-cold polar molecules

State preparation via Engi-
neered Dissipation

Toric Code, Absorbing State
models, SSH models

Contents

I	Introduction	11
	Preliminary remarks	13
1	Introduction to Topological Phases of Matter	19
1.1	Beyond Landau Symmetry Breaking Principle: Topological phases	19
1.1.1	Spontaneous Symmetry Breaking Principle	20
1.1.2	Transverse Field Ising Model	20
1.1.3	Toric Code Model	21
1.1.4	Toric code in the presence of perturbation: Beyond Symmetry Breaking	26
1.2	Notions of Topological Order	28
1.2.1	Robust degenerate ground state manifold	28
1.2.2	Local Unitary Transformation	29
1.2.3	Topological Entanglement Entropy	30
1.2.4	Modular matrices	31
1.2.5	Origins of topological order and topological order of other kinds	32
1.3	Topological Quantum Computation	33
2	Quantum Double Models and their Boundaries	37
2.1	Quantum Double Models	37
2.2	Boundaries of the Quantum Double	40
2.2.1	Boundaries between quantum double and vacuum	40
2.2.2	Generalized boundaries conditions	42
2.3	Quantum Double, $D(Z_2)$: Toric code model	43
2.3.1	Boundary I: Interface between $D(Z_2)$ and vacuum	45
2.3.2	Boundary II: Interface between $D(Z_2)$ and $D(Z_2)$	47
2.3.3	Summary	49

II	Robustness of intrinsic topological order in closed systems	51
3	Robustness of topological phases with open boundaries	53
3.1	Perturbation in the presence of boundaries	54
3.1.1	Exact Hamiltonians and Ising Hamiltonians	54
3.2	Characterizing the phase transition	57
3.2.1	Non Condensing case	57
3.2.2	Condensing case	59
3.3	A Closer look at the Condensing case	60
3.3.1	Ground state degeneracy, ΔE :	60
3.3.2	Topological Entanglement Entropy, γ :	61
3.3.3	Minimal Entangled States	65
4	Topological phases and underlying boundaries	69
4.1	Distinct Boundary conditions: Distinct Topological phases . .	69
4.2	$\tilde{G}_{\lambda=0} \neq \tilde{G}_{\lambda=1}$	73
4.2.1	Topology variation: Torus with no domain wall to a cylinder with a mixed boundary	73
4.2.2	Boundary variation: Cylinder with rough boundaries to a mixed boundary	78
4.3	$\tilde{G}_{\lambda=0} = \tilde{G}_{\lambda=1}$	81
4.3.1	Topology variation: Torus with domain wall to a cylinder with rough boundaries	81
4.3.2	Boundary variation: Cylinder with rough boundaries to smooth boundaries	85
4.4	Additional Remarks	87
4.4.1	Boundary variation: Interpolating between mixed boundaries on either end	87
4.4.2	Topology variation: Transition with the domain wall intact	88
4.4.3	Topology variation: Transition arising out of simultaneous dissection and gluing	90
III	Robustness of intrinsic topological order in open systems	91
5	TTPT's in an open quantum system	93
5.1	Open quantum systems - A review of key concepts	94
5.2	Interpolation via engineered dissipation	95

5.3	Dissipative interpolation via imperfect cooling	97
6	An operational definition of topological order	101
6.1	Perturbed Toric Code on a minimal lattice	103
6.1.1	Topological Signatures	103
6.2	Probing Topological Order via Error Correction Statistics . .	105
6.2.1	Mapping to the Ising 1D chain	106
6.2.2	Detecting topological phase transition in the perturbed minimal instance toric code	107
6.3	Absorbing State Models	110
6.3.1	Directed Percolation in 1D	110
6.3.2	Branching Annihilating Random Walks in 2D	111
6.4	Detecting topological phase transitions in an open quantum setting	111
6.4.1	Various approaches in identifying topologically trivial mixed states	112
6.4.2	Mapping Dissipative Toric Code models to Directed Percolation in 1D	113
6.4.3	Mapping Dissipative Toric Code models to BARW in 2D	119
IV	Robustness of symmetry protected topological or- der	125
7	Phase transitions in SSH models	127
7.1	SSH Model	127
7.1.1	Topological Invariants	129
7.1.2	Edge states	132
7.2	Error correction statistics to probe the phase transition	133
7.2.1	Excitation space	133
7.3	Error correction statistics via Matrix Product State simulations	135
7.3.1	Periodic Boundary	136
7.3.2	Open Boundary	136
7.4	Extended Bosonic SSH Model	138
7.4.1	Excitation space	138
7.4.2	Error Correction	140
V	Experimental realization via ultracold polar molecules	

	145		
8	Quantum Simulation using ultracold polar molecules		147
8.1	Detection of Molecules		148
8.2	Entangling Atom-Molecule interaction		151
8.3	Dissipative Quantum State Engineering		153
8.3.1	Dissipative Engineering via pulsed sequences		153
8.3.2	Dissipative Engineering via Lindbladian dynamics		155
VI	Conclusion		159
9	Summary and outlook		161
VII	Appendices		165
A	Condensation at the boundary of the quantum double		167
B	CNOT mechanism in the context of open boundaries		169
C	Error-Correction Statistics for 1D Ising chain		173
D	Monte-Carlo simulation of classical master equation		177
E	Extension of operational definition for fracton order		179
E.1	X-cube model		179
E.2	Cubic code model		181
	Bibliography		183
	Acknowledgements		202

Part I
Introduction

Preliminary remarks

Symmetries have been the cornerstone of physics in detecting different phases of matter. Landau symmetry breaking principle has been successful in classifying different phases using the notion of broken symmetries. The mathematical formalism of such symmetries and their breaking has been effectively captured by the concepts of group theory and it was largely believed until recently, that this theory of phase transitions was complete. In recent years, with the discovery of topological phases it has become quite apparent that broken symmetries alone are insufficient to quantify phase transitions as the nature of entanglement which captures quantum correlations plays a significant role. The discovery of such phases has once again thrown open the fundamental question of phases and their classification and this has led to a new classification scheme based on both symmetries and the pattern of the entanglement. In the ongoing process of classification, the discovery of intrinsic topologically ordered phases has been a major milestone due to its applications to quantum computation which involves storing and manipulation of quantum information. The ground state manifold of such topological phases are a haven for storing quantum memories as these are robust to local perturbations, i.e., quantum error correction can be efficiently implemented to correct the errors that corrupt the quantum memories. From the manipulation point of view, the quantum memories can be acted upon by unitaries which are realized by braiding of the anyonic quasiparticle excitations, a hallmark of phases with intrinsic topological order. Therefore, the study of topological phases is intriguing as it has both a fundamental significance in gaining insight into the phase transitions therefore aiming to structure the uncharted terrain of phases beyond the Landau symmetry breaking principle, while on the other hand, on the technological front, these systems provide a platform to efficiently store and manipulate quantum information thereby acting as a testbed for realizing quantum computers.

In this thesis, I explore the notion of intrinsic topological order in various setups. In Chap. 1, we begin by briefly introducing the general notion of Landau symmetry breaking principle followed by the study of phase transition in the context of transverse field Ising model. We then introduce the toric code model while discussing some of its salient features and further consider it in the presence of perturbation thereby introducing the notion of phases beyond Landau symmetry breaking principle. Having arrived at

an intuitive understanding, we explore various notions of topological order discussed in the literature, while concluding with the notion of topological quantum computation.

In Chap. 2, we further explore the notion of topological order in systems supporting open boundaries. We begin by defining the class of quantum doubles on a directed graph tiled on a general manifold both with periodic and open boundary conditions. We present a mathematical formulation of boundaries given the quantum double used to construct the bulk while introducing the behavior of excitations at boundary captured by the idea of anyon condensation. We recast the toric code model in the above formalism and derive the different boundary conditions of the toric code. The variants of these boundaries are central to the ideas discussed in the remaining chapters and therefore this chapter plays an important role in establishing some important fundamental concepts related to the construction of open boundaries.

Having introduced the basic ingredients of topological phases on different manifolds, in Part. II we analyze the robustness of topological phases under various perturbations in a closed environment. In Chap. 3, we consider the toric code on a cylinder in the presence of various perturbation resulting in a topological to trivial quantum phase transition. Due to the presence of the boundaries, the perturbed models can be effectively mapped to Ising models of the condensing and the non-condensing type. The non-condensing class sports a robust topological phase upto some perturbation strength while the topological phase in the condensing class breaks down as soon as the perturbation is turned on. We confirm this by computing numerical signatures like the lifting of the ground state degeneracy and Topological Entanglement Entropy (TEE) for the condensing case while benchmarking the numerical accuracy by comparing to the criticality of non-condensing scenario. We also introduce the notion of Minimal Entangled States (MES) as a signature capable of detecting the phase transition while also establishing its inaccuracy in predicting the exact critical strength.

In Chap. 4, we explore the sensitivity of the topological phase to the underlying manifold on which it is defined. The change in the boundary conditions induces a topological to topological phase transition (TTPT) with each boundary condition giving rise to a unique topological phase. We discuss the notion of Hamiltonian interpolation connecting various periodic boundaries to open boundaries effectively mapping a torus to a cylinder while also introducing the interpolation between different open boundaries on a cylinder. TEE, which was an effective signature in detecting the earlier introduced topological to trivial phase transition, becomes ineffective in detecting the different topological phases. On the contrary, the TEE remaining constant

implies that throughout the interpolation the phase is topologically ordered, thereby establishing the fact that the quantum phase transition is indeed a topological to topological phase transition. To effectively detect the criticality we introduce the notion of longest open loop operators, operators which sport excitations at their ends, whose expectation value captures the quantum criticality. We also note that these phase transitions are accompanied by broken symmetries in the excitation space and we establish appropriate conditions where the broken symmetries indicate the presence of a phase transition and vice-versa.

In Part. III, we explore various scenarios which encode topological phase transitions in an open setting. In Chap. 5, we explore the sensitivity of the topological order to the underlying boundaries in an open setting. To this extent, we engineer appropriate collapse operators with variable dissipative rates, which capture the interpolation as discussed in earlier in Chap. 4. These variable dissipative rates eventually control the diffusion dynamics of the excitations thereby resulting in different steady states which map to the ground states of the toric code on a torus and a cylinder, thus encoding a TTPT. We introduce two scenarios: one which involves pure cooling, that is, collapse operators which diffuses excitations without creating any new excitations while the other involves noisy cooling, where in addition to the diffusion the collapse operators induce new excitations. As in Chap. 4, the expectation value of the open loop operator effectively captures the phase transition. We also note that the open loop operator is an effective signature in scenarios which do not sport bulk excitations and/or support anyon condensation, therefore might not be applicable in a more general context.

From the earlier analysis, it is clearly evident that most of the signatures used to quantify topological phases and thereby detect different topological phase transitions are either scenario specific or inconsistent, i.e., while they are effective in few cases they seem to unreliable for the rest. In addition, the definitions based on local unitary transformations, connecting the ground state to a product state using finite depth quantum circuits seem to capture the essence of topological order they still remain elusive to numerically quantify topological order. Also, the understanding of topological order for mixed states has long remained an open question. Error correction being a trademark of the phases with intrinsic topological order, we try to quantify and arrive at a consistent operational definition for such phases by defining them as states whose errors can be corrected by a circuit of finite depth. In Chap. 6, we introduce a minimal instance of the toric code which under appropriate perturbation can be mapped to a 1D Ising chain. We introduce and verify the above definition for the perturbed minimal instance case benchmarking the results with respect to the well established 1D Ising chain. We further intro-

duce topological phase transitions in an open setup by engineering collapse operators to capture the nonequilibrium phenomenon of Directed Percolation (DP) in 1D and Branching Annihilating Random Walks (BARW) in 2D. The absorbing state, obtained at zero heating rate in the above processes maps to the steady state which is topologically ordered while at higher heating rates the steady state is mixed and maps to a active state is topologically trivial thereby inducing a dynamical topological phase transition. We compute the criticality related to the topological phase transition using the time statistics of the error correction schemes introduced as a part of the operational definition and observe that the criticality qualitatively resembles the thermodynamic transition in both 1D DP and 2D BARW.

Having analyzed phase transitions involving phases exhibiting topological order in various closed and open scenarios, in Part. III, we shift our focus to analyze phase transitions involving Symmetry Protected Topological (SPT) phases. To this extent, we consider the Su-Schrieffer–Heeger (SSH) model described by the hopping of particles on a 1D chain characterized by inter and intra-site hopping. In the limit of intra-site strength being dominant, the above model sports zero energy edge modes, a signature of SPT, while in the other limit the state is also a topological insulator sporting SPT order with no edge modes. By defining an appropriate excitation basis consisting of density and phase fluctuations along with an error correction algorithm which preserves the chiral symmetry, we extend the operational definition to accurately capture the phase transition. We extend the above analysis to a more generalized version of the SSH model, the Extended Bosonic SSH model, which hosts three distinct phases: anti-ferromagnetic and two distinct SPT phases. We consider the excitation basis as in the above SSH model along with a similar error correction algorithm and successfully quantify the distinct phases. One other significant result is that by considering the excitation space of domain walls with respect to the anti-ferromagnetic phase we successfully detect the phase transitions between the above phase and SPT phases.

In Part. IV, we turn our focus to possible experimental setups capable of realizing the quantum many-body phenomena discussed in the previous chapters. We turn to ultracold polar molecules and present various optimal strategies related to construction of basic building blocks which eventually lead to the realization of the delicate quantum many-body states. Based on the chemical reaction between atoms and molecules which induces a quantum Zeno-based blockade, we propose optimal strategies for the detection of molecules using atoms, entangling the internal degrees of freedom of the atoms and molecules, in addition, we also present optimal strategies for engineering dissipative dynamics.

Finally, in Chap. 9, we conclude by summarizing the key results which

Preliminary remarks

involve characterizing topological order in various closed and open setups. In addition, we also shed light on the exciting future directions which vary over a large spectrum from gaining fundamental insights into phase transitions, to the discovery of novel topological phases directed towards generating robust quantum memories.

Chapter 1

Introduction to Topological Phases of Matter

The classification of matter into different phases has helped gain a deeper insight into the understanding of the nature around us. In the classical context i.e., matter at $T > 0$, phases and their transitions have been classified based on the nature of symmetries they possess. For example, iron filings in the presence of a magnetic field: if the magnetic field strength is high these filings orient themselves in a particular direction, thereby breaking the continuous symmetry that they possess in the absence of a magnetic field. The simple observation of classifying matter based on notion of broken symmetries has been mathematically formulated in terms of group theory. Though this has been largely successful in classifying different phases, with the discovery of Berezinskii–Kosterlitz–Thouless (BKT) transition at $T > 0$ involving vortices and the discovery of certain quantum phases of matter [1], the theory based on symmetry breaking is no longer completely sufficient in classifying these phases and their transitions.

1.1 Beyond Landau Symmetry Breaking Principle: Topological phases

In this section, we introduce the notion of symmetries and thereby the concept of spontaneous symmetry breaking in the context of quantum phases. We then study these notions with respect to the transverse field Ising model which encodes a quantum phase transition between ferromagnetic and paramagnetic phases. We further introduce the toric code model in the presence of a perturbation and highlight the limitations of the Landau symmetry

breaking principle [2, 3, 4] leading to the introduction of topological phases characterized by new kind of order called *topological order*.

1.1.1 Spontaneous Symmetry Breaking Principle

As introduced earlier, phase transitions are marked by broken symmetries. We extend the above notion to the domain of quantum phases defined by a parameterized Hamiltonian, $H(\lambda)$. To this extent, we begin by defining the notion of symmetry with respect to a Hamiltonian, $H(\lambda)$ and its ground states in the thermodynamic limit.

Definition 1.1.1. *An unitary operator, U , is said to be a symmetry of a given Hamiltonian, H , if $[H, U] = 0$, implying that the unitary commutes with the Hamiltonian, $U^\dagger H U = H$.*

Definition 1.1.2. *A unitary operator, U , is said to be a symmetry of a state, $|\psi\rangle$, if it leaves the state invariant, $U|\psi\rangle = |\psi\rangle$.*

Consider the Hamiltonian, $H(\lambda)$, parameterized by λ such that $H(0)$ and $H(1)$ belong to distinct phases. Let U_s be the set of symmetries of the Hamiltonian $H(\lambda)$ for all λ with the ground states in the limit of $\lambda = 0$ and $\lambda = 1$ given by $|\psi\rangle$ and $|\phi\rangle$ respectively. The notion of spontaneous symmetry breaking is as follows: In the thermodynamic limit (system size $N \rightarrow \infty$) all the symmetries U_s of the Hamiltonian leave the ground state $|\psi\rangle$ invariant i.e., the symmetries of the Hamiltonian are symmetries of the ground state while the other ground state, $|\phi\rangle$ is not invariant under all the symmetries of the Hamiltonian. In other words, with change in λ , the ground state spontaneously breaks the symmetry of the Hamiltonian signaling the phase transition. In a more mathematical context, the symmetries of the Hamiltonian form a group, either continuous or discrete, while in one phase the group structure is preserved by the ground state while in the other the group structure is broken, which is the essence of Landau's symmetry breaking principle.

1.1.2 Transverse Field Ising Model

To illustrate the above principle, we consider a 1D ring with nearest neighbor Ising interaction in the presence of a transverse field. The Hamiltonian of the system is given by

$$H_{is}(\lambda) = - \sum_{i,j} \sigma_x^i \sigma_x^j - \lambda \sum_i \sigma_z^i \quad (1.1)$$

1.1 Beyond Landau Symmetry Breaking Principle: Topological phases

The above Hamiltonian is invariant under the following operation

$$\sigma_x \rightarrow -\sigma_x, \sigma_z \rightarrow \sigma_z$$

. The above operation is the inversion symmetry and can be achieved by $U = \otimes_i \sigma_z^i$, making U a symmetry operator for H_{is} . The above operator, U , along with $\mathbb{1}$, which is a trivial symmetry of H_{is} , forms a Z_2 group and we note that the Hamiltonian H_{is} is Z_2 symmetric at all λ .

We now discuss the ground states of the above Hamiltonian at various λ . At $\lambda = 0$, the ground state is ferromagnetic and doubly degenerate, while in the other extreme of $\lambda = 1$, the ground state is a paramagnet. In the σ_z basis, in the limit of $\lambda = 1$, the ground state is given by $|\psi\rangle = |000\dots 0\rangle$, where $|0\rangle, |1\rangle$ are eigenstates of σ_z . While in the limit of $\lambda = 0$, the ground state is double degenerate and given by either $|\phi\rangle = |+++ \dots +\rangle / |--- \dots -\rangle$, where $|\pm\rangle = \frac{1}{\sqrt{2}}(|0\rangle \pm |1\rangle)$. Therefore, for the transverse field Ising model in the limit of $\lambda = 1$, the ground state, $|\psi\rangle$, is invariant under the symmetry of the Hamiltonian while in the limit of $\lambda = 0$, the ground state, $|\phi\rangle$ breaks the symmetry of the Hamiltonian, as $\sigma_z|0\rangle = |0\rangle$, $\sigma_z|\pm\rangle = |\mp\rangle$. As we lower the perturbation strength, the ground state at some critical λ spontaneously chooses one of the ferromagnetically ordered ground states, spontaneously breaking the symmetry of the Hamiltonian, hence marking the presence of a phase transition from a trivial to a ferromagnetic phase. We also note that in the limit of $\lambda \rightarrow \infty$ the ground state preserves the Z_2 symmetry of the Hamiltonian where as in the limit of $\lambda \rightarrow 0$ the ground state itself is Z_2 symmetric but breaks the symmetry of the Hamiltonian.

1.1.3 Toric Code Model

It was largely believed that the every phase transition was accompanied by a broken symmetry and Landau symmetry breaking principle encompassed all the phase transitions. We now introduce the toric [5] code model which hosts an order that is beyond the above notion. Consider a square lattice with vertices (faces) denoted by $v(p)$ on a torus (periodic boundaries) with spins on the edges of the lattice as in Fig. 1.1. The Hamiltonian of the toric code is given by, H_{tc} , as in Eq. 1.2

$$H_{tc} = - \sum_v A_v - \sum_p B_p \quad (1.2)$$

where

$$A_v = \prod_{i=1}^4 \sigma_x^{(i)}, B_p = \prod_{j=1}^4 \sigma_z^{(j)} \quad (1.3)$$

where $i(j)$ belongs to the edges attached to the vertex (face), $v(p)$. We now discuss the ground state construction, the excitations in the system and further discuss the ground state degeneracy arising due to the action of the non-trivial loop operators on the ground state of the toric code.

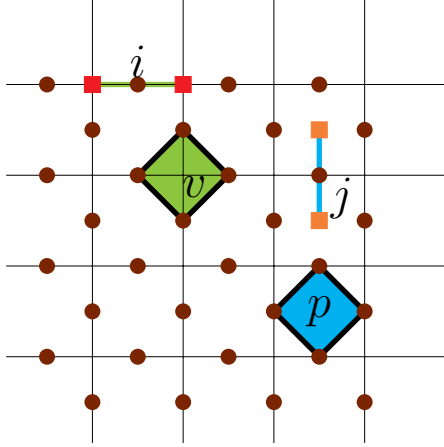


Figure 1.1: Toric code model. The A_v operator, denoted by the green diamond, acts on the spins attached to the vertex v . The B_p operator, denoted by the blue diamond, acts on the spins which form the face p . The red (orange) squares denote $A_v(B_p)$ violations which appear at the vertices(center of faces) and are generated by the action of $\sigma_{z(x)}^i$ which anti-commutes with the $A_v(B_p)$ operator.

Ground state of the toric code model

Let us denote the ground state of the toric code by $|\psi_{tc}\rangle$. To gain a better intuition, we present a pictorial representation of the ground state. To this extent, let us represent the two qubit states $|0\rangle, |1\rangle$ with a no-dash and dash (—) respectively. We begin by considering the no dash configuration at all sites on the lattice, $|\mathbf{0}\rangle = |00\dots 0\rangle$, which is the least energy eigenstate for all B_p operators, that is

$$B_p|\mathbf{0}\rangle = |\mathbf{0}\rangle, \forall p \quad (1.4)$$

The action of the A_v operator on the above state flips the qubits attached to the vertex, v , therefore, generating a loop around the vertex v , i.e., the no dash qubits around the vertex turn to dashed qubits generating a local loop. The ground state of the B_p operator and the above single A_v operator is a superposition of no loop configuration and a loop around vertex v . On

addition of one another vertex operator, say $A_{v'}$, the ground state of B_p, A_v and $A_{v'}$ is a superposition consisting no loop configuration, the individual loop configurations and combined loop of around v, v' . Extending this to include all the vertices the ground state is given by a loop gas structure, that is, the ground state is a superposition of all possible loop configurations and in the σ_z basis is given by $|\psi_{tc}\rangle = \mathcal{N} \prod_v (\mathbb{1} + A_v)|\mathbf{0}\rangle$, where \mathcal{N} represents the normalization factor [4].

Instead of considering the σ_z basis we could have considered σ_x basis, that is consider the state $|+\rangle = |++++\dots\rangle$ such that

$$A_v|+\rangle = |+\rangle, \forall v. \quad (1.5)$$

We can, thus, map the no dash, dash to $\{|+\rangle, |-\rangle\}$ qubits and generate a similar loop structure, as above, given by $\mathcal{N} \prod_p (\mathbb{1} + B_p)|+\rangle$.

The loop gas configuration observed in the above states signifies a specific entanglement pattern, and this pattern shall later be used to not only quantify the notion of topological order but also to distinguish between different topological phases i.e., different loop configurations in the superposition gives rise to distinct topological phases. We further introduce the notion of frustration-free Hamiltonian defined as follows:

Definition 1.1.3. *A Hamiltonian, $H = \sum_i h_i$, is said to be frustration-free if the ground state of the Hamiltonian, H , is ground state of each of h_i 's.*

It is clear that the above introduced toric code Hamiltonian, as in Eq. 1.2 is frustration-free, we shall invoke this fact at a later time to study the phase transitions between different Hamiltonians which are frustration-free.

Excitation space of the toric code model

We begin by noting the following anti-commutating relations

$$\{\sigma_z^{(i)}, A_v\} = 0, \{\sigma_x^{(j)}, B_p\} = 0 \quad (1.6)$$

where i, j denote the edges attached to the vertex v and face, p respectively. Consider the action of σ_x on the toric code ground state, $|\psi_{tc}\rangle$, say $|\psi_p\rangle$. We note the following

$$\begin{aligned} B_p|\psi_p\rangle &= B_p\sigma_x^{(i)}|\psi_{tc}\rangle \\ &= -\sigma_x B_p|\psi_{tc}\rangle \\ &= -\sigma_x|\psi_{tc}\rangle \\ &= -|\psi_p\rangle \end{aligned} \quad (1.7)$$

Therefore, the action of the anti-commutator on the edge i , $\sigma_{x(z)}^{(i)}$ generates a pair of excitations on neighboring faces shared by edge i . From the above, we note that the energy cost to create a pair of excitation is four units, for single excitation being 2 units. The excitations are particle like and are identified by at the center of the excited faces/vertices. The excitations once generated can be moved around freely in the lattice by applying additional anti-commutators with no additional energy cost. These long strings hosting two excitations at their ends, referred to as ribbon operators, leave the excitations deconfined which is a feature of such models. We fix the following terminology, $\sigma_{z(x)}$ generate vertex (face) excitations which we refer to as $A_v(B_p)$ violations and denote them by $e(m)$. We now discuss some important characteristics of the above introduced excitations:

Fusion rules:

We define the collective behavior of excitations in terms of the fusion rules. To concretize the idea, we introduce the notion of vacuum channel, denoted by 1 which is equivalent to no excitation being present. Consider a pair of A_v violations, the pair if considered as a single unit would project back to the ground state, therefore the collective behavior, fusion of these excitations results in the vacuum. For the case of the toric code, using the above notion we arrive at the fusion rules, as in Eq. 1.8, Fig. 1.2

$$\begin{aligned} e \times 1 &= e, & m \times 1 &= m \\ e \times e &= 1, & m \times m &= 1 \\ e \times m &= f, & m \times e &= f \end{aligned} \tag{1.8}$$

The fusion of e and m results in a composite particle f and thus the set of excitations of the toric code is complete with the inclusion of vacuum, 1, and the composite particle, f .

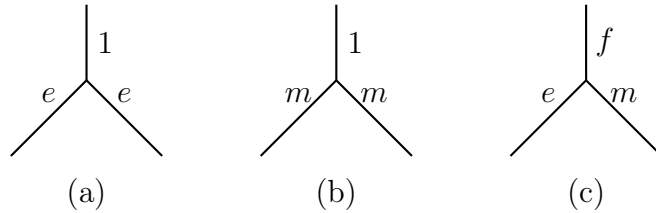


Figure 1.2: Graphical representation of the fusion rules.

Braiding:

As the excitations introduced above are particle like, we now study the exchange statistics. To compute the exchange statistics, we braid the excita-

tions one around the other due to which wave-function picks up a phase. In the case of $A_v(B_p)$ violations the wave-function remains invariant and thus these are bosonic in nature. While the composite particle obtained from the fusion of A_v, B_p violation picks up a factor of -1 and hence this is identified as a fermion. In a more general setting, it is possible that the wave-function picks up *any* phase due to the braiding and hence we term these excitations as *anyons*. Anyons come in abelian and non-abelian flavors, the former scales the wave-function by a scalar phase (as in the fermion or the boson) while the latter results in a unitary operator acting on the wavefunction.

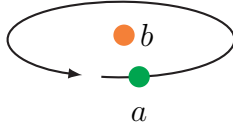


Figure 1.3: Braiding of anyons a type around b type results in the scaling of the wavefunction by a complex phase factor for abelian anyons, while in the case of non-abelian anyons braiding results in a unitary matrix acting on the wavefunction.

Ground state degeneracy

Having introduced the notion of creating long loops with no energy cost and fusing excitations to vacuum, we now explore the ground state degeneracy arising out of the underlying topology on which we construct the toric code model. We consider the lattice on a surface with periodic boundaries i.e., a torus. We define the non-trivial loops on the torus as curves which are not homotopically equivalent i.e., two curves are said to be homotopically equivalent if one can be smoothly deformed into the other, i.e., without breaking the curve. We construct the non-trivial loop operators by fusing the excitations to the vacuum along the non-trivial loops of the torus by the application of $\sigma_{x(z)}$ operators. The action of the non-trivial loop operators on $|\psi_{gs}\rangle$, defined in the earlier section, gives rise to orthogonal ground states, therefore the ground state manifold is degenerate. For example, consider the ground state $|\psi_{gs}\rangle = \mathcal{N}(\mathbf{1} + A_v)|\mathbf{0}\rangle$ in the σ_z basis. Let us consider the B_p violations which are generated by applying σ_x operators. Consider the non-trivial loops around the legs of the torus, L_x and L_y , and the operators corresponding to the loops given by L_x^x, L_y^x respectively. The ground state manifold is fourfold degenerate and is given by

$$|\psi_1\rangle = |\psi_{gs}\rangle$$

$$\begin{aligned} |\psi_2\rangle &= L_x^x |\psi_{gs}\rangle \\ |\psi_3\rangle &= L_y^x |\psi_{gs}\rangle \\ |\psi_4\rangle &= L_x^x L_y^x |\psi_{gs}\rangle \end{aligned}$$

The above recipe can be repeated for the σ_x basis, with loop operators formed by A_v violations, that is by applying σ_z operators, L_x^z, L_y^z along the loops L_x, L_y . We note that in the σ_z basis, the L_x^x, L_y^x operators generate the other degenerate ground states while the operators L_x^z, L_y^z leave the ground state invariant. In the σ_x basis, the operators L_x^z, L_y^z generate the degenerate ground state manifold while L_x^x, L_y^x leave the trivial ground state invariant. The linear transformation connecting the different ground states of σ_z and σ_x basis is given by mapping as in Eq. 1.9

$$\begin{bmatrix} |\psi_1\rangle \\ |\psi_2\rangle \\ |\psi_3\rangle \\ |\psi_4\rangle \end{bmatrix} = \frac{1}{2} \begin{bmatrix} 1 & 1 & 1 & 1 \\ 1 & -1 & 1 & -1 \\ 1 & 1 & -1 & -1 \\ 1 & -1 & -1 & 1 \end{bmatrix} \begin{bmatrix} |\psi'_1\rangle \\ |\psi'_2\rangle \\ |\psi'_3\rangle \\ |\psi'_4\rangle \end{bmatrix} \quad (1.9)$$

where $|\psi_i\rangle, |\psi'_i\rangle$ are the ground states in σ_z and σ_x basis respectively. The linear transformation connecting the ground states is the modular- S matrix which is an important signature of topological order which we shall introduce later.

To conclude the section, we note a known result connecting the genus of the surface on which the lattice is placed with the ground state degeneracy, which thereby signifies the importance of the underlying topology

Lemma 1.1.1. *Let S be a surface with genus g on which the lattice L with toric code Hamiltonian H_{tc} is wrapped. The total number of degenerate ground states is given by 4^g .*

For example, the number of degenerate ground states on a torus with single puncture, genus 1 torus, is four, while on sphere whose genus is 0 the ground state is unique. This ground state degeneracy plays an important role in efficiently encoding quantum memories. We shall elaborate on this in a later section, but we note that a torus with genus, n , has a ground state degeneracy of 4^n allowing the storage of $2n$ qubits.

1.1.4 Toric code in the presence of perturbation: Beyond Symmetry Breaking

Having discussed the toric code model, we now return to the notion of phase transitions beyond Landau symmetry breaking principle. To this extent, we

1.1 Beyond Landau Symmetry Breaking Principle: Topological phases

consider the toric code model in the presence of perturbation, we could have considered any perturbation but for brevity we analyze the case of toric code perturbed by a transverse field, $H_p^z = \sum_i \sigma_z^{(i)}$, as in Eq. 1.10

$$H_{tc}^p = J_{tc}H_{tc} + h_z H_p^z \quad (1.10)$$

In the limit of $J_{tc} \gg h_z$, the ground state is four fold-degenerate while in the other extreme of $h_z \gg J_{tc}$ we have a paramagnet and a non-degenerate ground state manifold. Therefore, at some point we expect a phase transition as in the former the ground state is highly entangled while in the latter the ground is a product state. The phases are completely distinct due to the entanglement in the ground state manifold of the ground states and hence varying the strength triggers a phase transition. To further consolidate the phase transition, we note that the excitations in the former limit are deconfined (long strings with excitations at the end cost finite energy) while the excitations in the other extreme are confined (long strings with excitations need infinite energy).

We now discuss the notion of symmetry breaking in the above scenario. The Hamiltonian, H_{tc}^p , as in Eq. 1.10 is Z_2 symmetric as it is invariant under $U = \otimes_i \sigma_z^i$ since $UH_{tc}U^\dagger = H_{tc}$, $UH_p^zU^\dagger = H_p^z$. The ground state in either phases respect the symmetry i.e., $U|\psi_{tc}\rangle = |\psi_{tc}\rangle$ this is due to the fact that each of the loop configurations in the ground state of the toric code has modulo 2 $|1\rangle$'s while the paramagnet remains invariant under the above unitary U . Hence we have established that the perturbed toric code phase is beyond the symmetry breaking principle, i.e., these phase transitions are not accompanied by any broken symmetries. The key difference between the toric code ground state and the paramagnet is that while the former is highly entangled the latter is a product state. The above implies that symmetry alone is insufficient to describe phases and the accompanying phase transitions but also the entanglement pattern of the ground state i.e., the pattern of superposition of the closed loop configurations in the ground state, play an important role. This entanglement pattern of the ground state gives rise to the notion of *intrinsic topological order* [6]. The gapped ground states (protected ground states, which we introduce in the next section), the degeneracy of the ground state manifold dependent on the topology of the underlying manifold, the deconfined excitations leading to non-zero expectation value of trivial loops (also known as Wilson loops), the area law scaling of entanglement entropy with a sub-leading constant term are all characteristics of *intrinsic topological order*. In the next section, we introduce and discuss some of the prominent signatures of *intrinsic topological order* leading to a potential definition of *intrinsic topological order*. In the future chapters, we discuss the merits and

shortcomings of the above notions in various scenarios and also propose an operational definition to characterize topologically ordered phases.

1.2 Notions of Topological Order

In the previous section, we have introduced that symmetries alone do not quantify different phases but the pattern of entanglement in the ground state plays an equally important role in quantifying different phases. The toric code ground state in the presence of perturbation is one such phase which is beyond the Landau symmetry breaking principle and in this section we aim to characterize such phases using the notion of *topological order*.

1.2.1 Robust degenerate ground state manifold

One of the key characteristic of topological order is the ground state degeneracy due to the underlying topology. In general, the fusion rules defined above, allow the the excitations to fuse to vacuum giving rise to the possibility of constructing non-local loop operators along the non-trivial loops (under the constraint that the underlying manifold supports the same). These non-local loop operators project the trivial ground state into orthogonal states giving rise to a degenerate ground state manifold. It is also interesting to note that the ground states are robust to local errors, consider the perturbed Hamiltonian, H_{tc}^p , as in Eq. 1.10, with the perturbed ground state given by $|\psi^p\rangle$, as in Eq. 1.11

$$|\psi^p\rangle = |\psi\rangle + GH_p^z|\psi\rangle + (GH_p^z)^2|\psi\rangle + \dots \quad (1.11)$$

where $|\psi\rangle$ is one of the four degenerate ground states and $G = \sum_n \frac{h_z |n\rangle \langle n|}{E_0 - E_n}$ [7] where $|n\rangle$ denotes the excited states of H_{tc} . The perturbative expansion remains similar for all the ground states of the degenerate manifold, resulting in perturbed states whose mixing with other degenerate ground states is exponentially suppressed. This is due to the fact that mixing of the ground states is only possible when perturbative terms of high orders, on the order of the system size, are included in the expansion. These higher order terms are capable of generating long strings which complete the non-trivial loop thereby projecting into other degenerate ground states. Therefore, due to the exponential suppression the ground manifold is robust and topological order can be characterized in general as follows

$$\langle \psi_i | L | \psi_j \rangle = C \delta_{ij} + \epsilon_{ij} \quad (1.12)$$

1.2 Notions of Topological Order

where $|\psi_i\rangle, |\psi_j\rangle$ are topologically ordered ground states, L is any local operator with $\epsilon_{ij} \rightarrow 0$ as system size, $N \rightarrow \infty$.

In other words, the above notion implies that the degenerate ground states of a topologically ordered system cannot be mapped to one other via local operators. Based on the above observation, the authors in [8, 9] have introduced Topological Quantum Order (TQO) conditions that are to be satisfied by a system exhibiting topological order. We motivate the TQO conditions by considering the toric code model, while we note that these conditions are defined in a more general setting in the above references and we refer the interested readers to the above for a more complete treatment. The TQO conditions are as follows

1. *TQO-1*: For any local operator O ,

$$POP = c_0 P, \quad (1.13)$$

where $P = \prod_v A_v \prod_p B_p$, with c_0 being a complex number.

2. *TQO-2*: Given two regions A, B on the lattice such that B is the smallest region that includes A . Then the kernel of the reduced density matrices $\rho_A = \text{Tr}_{A^c}(P)$ and $\rho_A^{(B)} = \text{Tr}_{A^c}(P_B)$ coincides, where $P_B = \prod_{v \in B} A_v \prod_{p \in B} B_p$ and A^c represents the complement of A .

We refer the reader to the above cited references for a general proof on the protection of spectral gap of a system satisfying the TQO conditions, in the presence of a perturbation. In Ref. [10], the authors have presented the proof for the gap protection in specific for the quantum double models which we introduce in the next chapter.

1.2.2 Local Unitary Transformation

The pattern of entanglement, as in the superposition of closed loop configurations in the ground state of the toric code can be qualified by the depth of the local unitary transformation connecting the above ground state to a product state. To this extent, we define the notion of local unitary, finite depth and then introduce the notion of long-range entanglement [11].

Definition 1.2.1. *An unitary operator, U , defined on a Hilbert space of n qubits, is said to be k -local, if it acts non-trivially on at most k qubits.*

Definition 1.2.2. *The depth, d , of a quantum circuit is given by the number of layers of non-overlapping local unitaries.*

Theorem 1.2.1. *A state, $|\phi\rangle$, is said to be long-range entangled if and only if it cannot be mapped to a product state via local unitaries of constant depth [11].*

Intuitively, the ground state of the toric code cannot be mapped to a product state via local unitaries of constant depth and hence is long-range entangled. On comparing the entangled state to the product state by imposing constraints on the unitaries connecting these states, it is possible to quantify the entanglement and therefore characterize topological order. We conclude that all *intrinsic* topological ordered states are Long-Range Entangled (LRE). Though, we define *intrinsic* topological ordered states as long-range entangled it is still difficult to quantify and detect such states, for which we later introduce a definition based on error-correction statistics.

1.2.3 Topological Entanglement Entropy

One of the key characteristics of topological order is the constant sub-leading term in the computation of entropy. Consider a region, A , with boundary of length L and with the reduced density matrix of the region given by ρ_A . For a long range entangled state the Von Neumann entropy given by S_A , satisfies an area law given by

$$S_A = aL - \gamma \quad (1.14)$$

where $S_{topo} = -\gamma$ is termed as Topological Entanglement Entropy (TEE) and is a signature of topological order. In a general setting, the above term can be captured by computing [12]

$$S_{topo} = S_A + S_B + S_C - S_{AB} - S_{BC} - S_{AC} + S_{ABC} \quad (1.15)$$

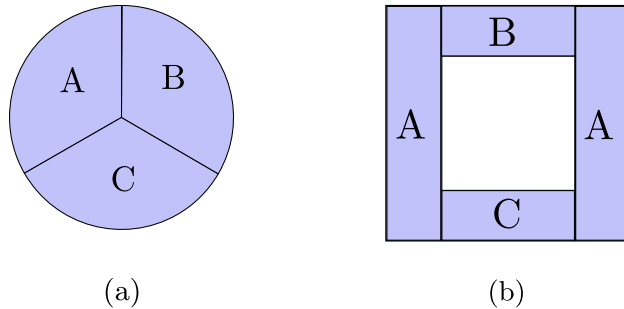
where S_X denotes the entropy of region X, with A,B,C as in Fig. 1.4(a) One other approach to compute the sub-leading constant term is by computing [13]

$$S_{topo} = S_{ABC} - S_{AC} - S_{AB} + S_A \quad (1.16)$$

with S_X as defined above and with A,B,C as in Fig. 1.4(b). It is also significant to note that the topological entanglement entropy is related to the quantum dimensions of the quasi-particle excitations of the topologically ordered state, i.e.,

$$\gamma = \log(D), \text{ where } D = \sqrt{\sum d_i^2} \quad (1.17)$$

with d_i denoting the quantum dimension of the quasi-particle of the i^{th} type. For the case of toric code, the quantum dimension of the four abelian anyons is equal to 1, therefore for the case of the toric code TEE, $\gamma = \log 2$. We note

Figure 1.4: Schemes used to extract S_{topo} .

that, though the above proposed schemes capture TEE in the thermodynamic limit, while for a finite system size these extraction schemes suffer from finite-size corrections. As an alternative, to effectively extract TEE, the authors of Ref. [14] have proposed a method which involves computing the entropy of a cylindrical region obtained by slicing the torus, thereby avoiding the corners which are inevitable in the above proposed schemes. We extend the above method to the case of open boundaries in Chap. 3.

1.2.4 Modular matrices

Modular- S and T matrices capture the mutual and self statistics of the quasi-particles excitations of a topologically ordered phase. The mutual statistics refer to exchange of excitations which in (2+1)D results in braiding, implying that the S and T matrices capture the braiding rules which can be further used to derive the fusion rules, as detailed in the Appendix. A. As each distinct topological ordered phase is characterized by unique quasi-particles excitations it is conjectured that modular- S and T matrices are central to the classification of *intrinsic* topological order [6]. These modular matrices are not only effective in detecting the topological to trivial phase transitions [15, 16, 17], but also are effective in distinguishing between different topological phases exhibiting the same topological order, for instance toric code and double semion topological phases as in Ref. [18]. The central theme in constructing modular matrices given the degenerate ground state manifold is the notion of Minimal Entangled States or Minimal Entropy States (MESs). MESs are states which minimize the entanglement entropy of a non-trivial region, for instance: cylinder on a torus. Further, in Ref. [15], the authors have established that these as eigenstates of the non-trivial loop operators which translate between different degenerate ground states. The unitary transformations between different MESs are related to the modu-

lar matrices, as these modular matrices are also known to connect different ground states as noted in Eq. 1.9. We discuss the algorithm used for extracting modular matrices, given a Hamiltonian in Chap. 3. In a more general context, modular matrices are defined in the context of Topological Quantum Field Theories (TQFT's). A (2+1)D TQFT assigns a Hilbert space to a 2D orientable surface, such that the Hilbert space remains invariant with respect to the deformations of the underlying topology. The Hilbert space encodes the information of the ground state manifold of some Hamiltonian, for instance the toric code Hamiltonian. The modular transformations are defined as linear transformations on the above introduced Hilbert space that preserve the ground state manifold. We note that the above discussion on TQFT's lacks mathematical rigor and we refer the interested reader to the following references [19, 20, 7, 21].

1.2.5 Origins of topological order and topological order of other kinds

In this section, we present a brief overview on the origins of topological order, while ending the section with the introduction of Symmetry Protected Topological (SPT) order. The topological order introduced in the earlier sections via the toric model is generally referred to as *intrinsic* topological order and the notions defined previously in the current section hold in the case of *intrinsic* topological order. We note that this section is heavily derived from the Refs. [6, 11].

We begin by introducing the Fractional Quantum Hall (FQH) state. Motivated by the idea to realize a electron crystal, experiments were setup where a 2D electron gas was subjected to high magnetic field at very low temperatures. Though, they failed to observe a electron crystal, instead they found a quantum liquid with strong interactions, this strongly correlated electron state was termed as a FQH state. FQH states are characterized by filling fraction, ν , which is given by the ratio of density of electrons to the applied magnetic field. The striking feature of the FQH states is that the filling fractions are given by exact rational numbers, which leads to precise computation of Hall resistance given by $\nu^{-1} \frac{h}{e^2}$, which has applications in quantum metrology. Different filling fractions correspond to distinct FQH states and therefore, the map of one to the other involves a phase transition [22]. With all the FQH states having the same symmetry properties, these phase transitions are not signaled by broken symmetries and therefore these phases are classified as phases beyond the Landau symmetry breaking principle.

FQH states being quantum liquids hints at the possibility that the elec-

1.3 Topological Quantum Computation

trons might have arranged themselves in a pattern. This can be further established by observing that (a) every electron has a quantized cyclotron motion due to the magnetic field (b) every electron takes quantized steps around another and (c) they tend to stay away from each other due to the Coulombic repulsion [6]. Due to these local patterns there emerges a global pattern or global order which is termed as *intrinsic* topological order. The global pattern of quantum fluctuations corresponds to a pattern of entanglement that is long ranged entangled [23], the precise definition of which we have introduced in the earlier section.

Prior to the discovery of FQH states, Integer Quantum Hall (IQH) states were discovered, states whose filling fraction results in an integer instead of a fraction as in the FQH states. As in the FQH case, IQH states are beyond the Landau symmetry principle as a phase transition between two distinct IQH states characterized by distinct filling fractions does not involve any broken symmetries. The distinction between the FQH and IQH states is that in the latter the Hall resistance is connected to a topological invariant known as the Chern number [24, 22]. The more striking difference is that these topological invariants are tied to some symmetry, in case of the IQH, this is the time reversal symmetry. That is, the existence of the topological invariant is in one-to-one correspondence of the underlying symmetry of the system, if the symmetry is broken the topological invariant ceases to exist leading to topological triviality. These phases are thus referred to as Symmetry Protected Topological (SPT) phases. In addition to IQH states, band and topological insulators exhibit SPT order [11]. One other significant difference between the SPT phases and phases exhibiting intrinsic topological order is that though both are gapped phases, the ground state degeneracy in the former is fixed irrespective of the underlying topology on which they are defined while in the latter the ground state degeneracy is a property of the underlying manifold [24]. SPT phases are short-range entangled, that is these phases can be mapped to a product state using local unitaries of finite depth with the local unitaries essentially breaking the symmetry unlike the long range entangled states which cannot be mapped to a product state using local unitaries of finite depth. On the classification front, bosonic SPT phases are classified by group cohomology theory while tensor categories are effective in classification of intrinsic topological order.

1.3 Topological Quantum Computation

From the classification paradigm we shift to the application side of topological phases of matter. Topological quantum computing [25, 26, 27, 28, 29,

[30, 31, 32] deals with the storage and manipulation of quantum memories using properties which are intrinsic to topological phases. The ground state manifold being degenerate can be effectively used to encode logical qubits, with the braiding of non-abelian anyons resulting in a unitary which can be used to manipulate the stored memories. In a general setting, the scheme involves the following: we encode the logical qubits in the degenerate ground state manifold, we generate non-abelian anyons from vacuum, braid them around to realize the required unitary finally fusing them back to vacuum as in Fig. 1.5. The most striking features of the above scheme include robustness of logical qubits to local errors and the braiding is path independent, paths that are homotopically equivalent can be traced by the anyons to realize the unitary, with no additional energy cost for the moving of the anyons as they are deconfined.

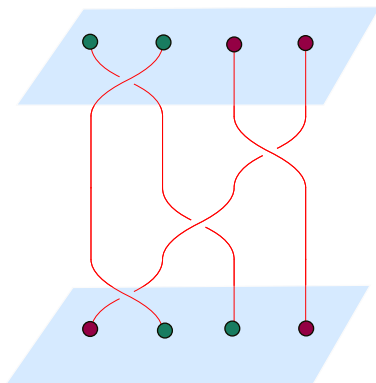


Figure 1.5: Schematic representing the braiding of non-abelian anyons. The scheme of topological quantum computer involves encoding the logical qubit in the ground state manifold. To perform an unitary operation on the logical qubit, we create a sea of non-abelian anyons, braid them and finally annihilate them.

We present the above ideas using Kitaev toric code and Kitaev 1D wire. For the toric code model, as introduced earlier the ground state manifold is fourfold degenerate which supports two qubits. Conventionally, though toric code does not support non-abelian anyons, it is possible to create twist defects [33] which give rise to non-abelian Ising anyons. From a practical point of view, the periodic boundaries which give rise to degenerate manifold might not be suitable for an experimental setup, this can be circumvented by considering toric code on a surface with punctured holes [34]. Therefore, a punctured surface code with twist defects is a suitable candidate for topological quantum computation.

1.3 Topological Quantum Computation

The other example we consider is the Kitaev 1D wire [35], which is an SPT phase similar to the one introduced later in Chap. 7. By expressing 1D chain in terms of coupled Majorana fermionic operators and further changing the strength on their intra-site coupling gives rise to unbounded zero edge modes. Due to the half-filling constraint, each pair of uncoupled Majorana fermions give rise to a qubit. By further varying the parameters of the Hamiltonian of a generalized 1D Kitaev chain (specifically the chemical potential) it is possible to create multiple unbounded Majorana pairs and therefore encode multiple qubits. These qubits are protected against local perturbation as the quantum memory is encoded in the fermion parity which are highly non-local. The Majorana fermions are non-abelian in nature with their exchange statistics resulting in a unitary. In a more general context, we note that it is possible to approximate any arbitrary unitary gate by braiding of non-abelian anyons, for instance using Fibonacci non-abelian anyons, further implying that non-abelian anyons are perfect platforms in realizing a universal quantum computer [36].

Chapter 2

Quantum Double Models and their Boundaries

In this section, we introduce the Kitaev quantum double models [5, 29, 7, 37] which are a generalization of the toric code model introduced earlier. We introduce these models on a directed graph tiled on a general manifold with periodic boundary conditions, later introducing the notion of open boundary conditions [38, 39, 40, 41, 42, 43, 44, 45, 46]. We outline a procedure to identify the distinct anyon types (also referred to as excitation/superselection sectors) given the group which characterizes the quantum double. Further, we introduce the notion of open boundaries with respect to the group that defines the bulk, thereby introducing the notion of anyon condensation [40, 47, 48]. Finally, we conclude by re-casting the toric code model as the quantum double of the Z_2 group, while also presenting the different boundary conditions of the same. We note that these class of models can be further generalized by twisted quantum doubles where the gauging is further scaled by a scalar (3-cocycle) [49]. The above models can further be generalized by the Levin-Wen string nets [50] which are obtained by the categorification of the quantum doubles. We also note that this section largely follows the discussion as in Refs. [5, 29, 7].

2.1 Quantum Double Models

We begin by considering a directed graph, D , with vertices v , directed edges, e , and faces, f , as in Fig. 2.1 along with a group, G , of order n . To each directed edge of the above graph we attach a qudit with a Hilbert space dimension of $|G|$ and identify it by the group element $|g\rangle$, where $g \in G$. We define a site, s , as a pair of vertex, v and face, p , $s = (v, p)$.

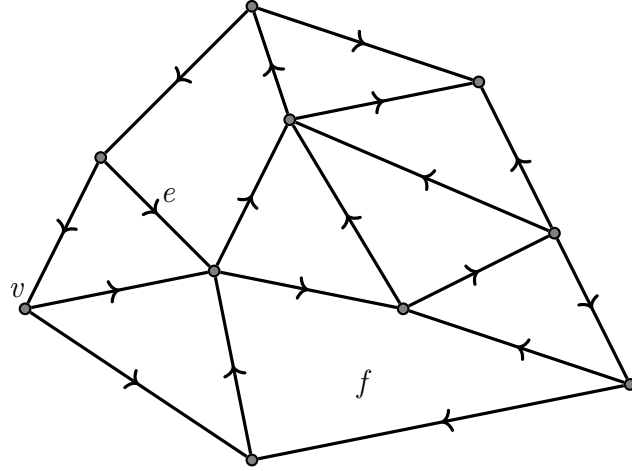


Figure 2.1: Directed graph, D , with vertices, v , directed edges, e and faces, f .

As in Ref. [5], we define the operators $L_+^g, L_-^g, T_+^h, T_-^h$ acting on the spins of the edges as in Eq. 2.1, where $g, h \in G$.

$$\begin{aligned} L_+^g|\alpha\rangle &= |g\alpha\rangle & T_+^h|\alpha\rangle &= \delta_{h,\alpha}|\alpha\rangle \\ L_-^g|\alpha\rangle &= |\alpha g^{-1}\rangle & T_-^h|\alpha\rangle &= \delta_{h^{-1},\alpha}|\alpha\rangle \end{aligned} \quad (2.1)$$

We define the operator $L^g(j, s) = L_\pm^g(j)$, if the oriented edge is pointed towards v we define $L^g(j, s) = L_-^g(j)$ and if it pointed away we define $L^g(j, s) = L_+^g(j)$ with $L_\pm^g(j)$ defined as the operator L_\pm acting on the spin- j attached to the edge. We now define the operators A_s^g as in Eq. 2.2, Fig. 2.2 where $g, h \in G$

$$A_s^g = \prod_{j \in v} L^g(j, s) \quad (2.2)$$

To define the B_s^h operators, we fix a direction either clockwise or anti-clockwise, here we set it to clockwise, for the face p of the site s and define $T^h(j, s) = T_\pm^h(j)$. If the directed edge is in the above fixed direction, we define $T^h(j, s) = T_+^h(j)$ else we define $T^h(j, s) = T_-^h(j)$. We define the B_s^h operator as in Eq. 2.3, Fig. 2.3

$$B_s^h = \sum_k \prod_{j \in p} T^{k_j}(j, s) \quad (2.3)$$

where k is the collection of all combinations such that the product of the elements in each combination is equal to h .

2.1 Quantum Double Models

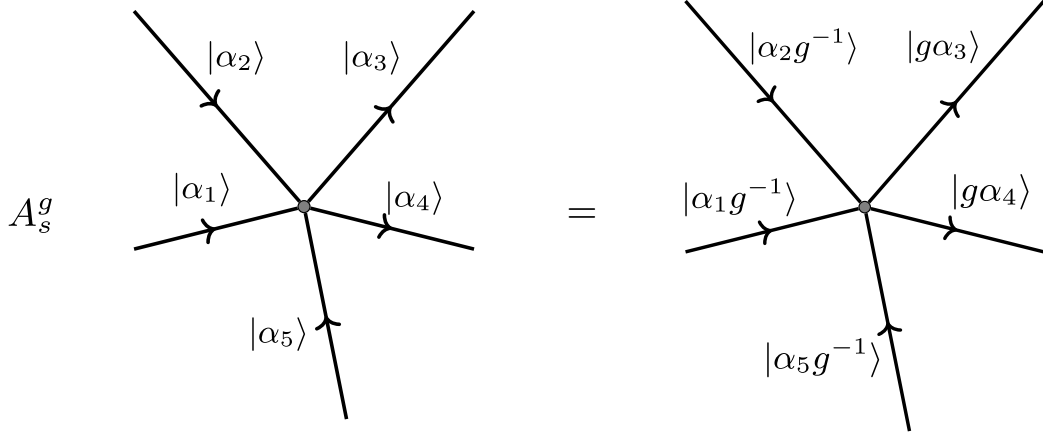


Figure 2.2: Definition of the A_s^g operator.

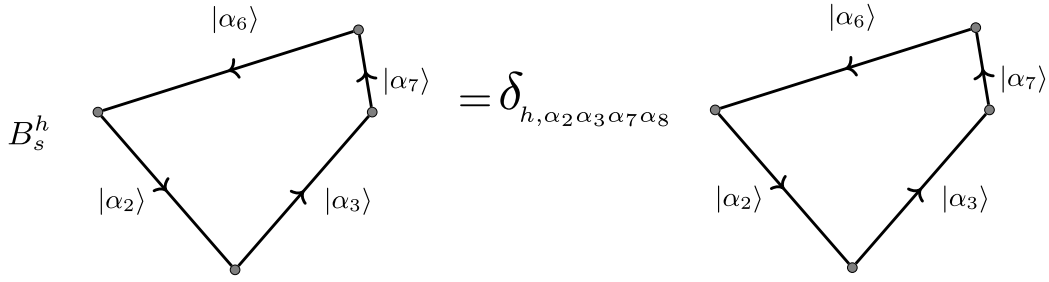


Figure 2.3: Definition of the B_s^h operator.

We note that there exists an isomorphism between the algebra of the operators at site s and the quantum double $D(G)$ [40] and hence these models are referred to as quantum double models.

We further define,

$$A_v = \frac{1}{|G|} \sum_{g \in G} A_s^g \quad (2.4)$$

$$B_f = B_s^e$$

where e is the identity of the group G . We note that the above operators are Hermitian which can be established using the properties of the quantum double $D(G)$ [40]. Using all the above ingredients, we construct the general

quantum double Hamiltonian, H_{qd} , given by

$$H_{qd} = - \sum_v A_v - \sum_f B_f \quad (2.5)$$

We note that the operators A_v and B_f commute (using Eqs. 2.2, 2.3), and the ground state, $|\psi_{qd}\rangle$ is a simultaneous ground state of all the local operators

$$A_v |\psi_{qd}\rangle = |\psi_{qd}\rangle \quad B_f |\psi_{qd}\rangle = |\psi_{qd}\rangle \quad \forall v, f \quad (2.6)$$

The excitations in the system are given by the violation of the A_v , B_p operators and are identified at the center of the vertices and faces respectively. The operators which generate these excitations are known as ribbon operators and these generate excitations in pairs [5]. The distinct anyon types are given by the irreducible representations of the quantum double, $D(G)$, which are in one-to-one correspondence with the irreducible representations (irreps) of the centralizers¹ of the conjugacy classes² of the group G . We also comment that the abelian/non-abelian nature of the group G is reflected in the anyons being abelian/non-abelian which we have defined earlier. Given that the anyons are given by irreps as above, it is straight forward to compute the S -matrix from which it is possible to compute the fusion rules using the Verlinde formula, see Appendix. A for details.

2.2 Boundaries of the Quantum Double

In this section, we extend the above analysis to various open boundary scenarios, where an open boundary is defined as the interface between the quantum double exhibiting topological order and vacuum, later we also introduce cases where we discuss interfaces between two quantum doubles. The following sub-sections are heavily derived from Ref. [40].

2.2.1 Boundaries between quantum double and vacuum

In the earlier section, we introduced the quantum double model on general directed graph, here, for the sake of clarity we consider a square lattice with an interface as in Fig. 2.4, the discussion can be easily extended to any general directed graph.

¹Given a group G , the centralizer of a subset $S \subset G$ is given by $C(S) = \{g \in G | gs = sg \forall s \in S\}$

²Given a group G , with $a \in G$, conjugacy class of a , \bar{a} , is given by $\bar{a} = \{gag^{-1} | g \in G\}$

2.2 Boundaries of the Quantum Double

As above, the directed edges of the graph in the bulk are labeled by the elements of the group G , used to construct the quantum double $D(G)$. The edges on the interface are decorated by the elements of the subgroup, $K \subseteq G$, therefore defining the open boundary. That is given a quantum double, $D(G)$, the possible boundaries are classified by distinct subgroups $K \subseteq G$. Due to the introduction of the open boundary, the A_v, B_p operators of the Kitaev Hamiltonian, as in Eq. 2.5, have to be modified to accommodate the boundaries. To this extent, we define the A_v^K, B_p^K operators as in Eq. 2.7

$$\begin{aligned} A_v^K &= \frac{1}{|K|} \sum_{k \in K} A_v^k \\ B_p^K &= \sum_{k \in K} B_p^k \end{aligned} \quad (2.7)$$

where A_v^k, B_p^k are defined as before as in Eqs. 2.2, 2.3. For the sake of brevity we redefine them in Fig. 2.4

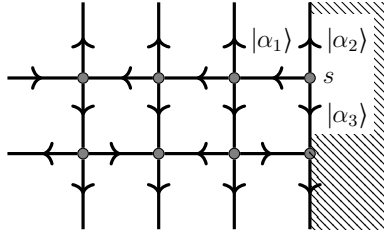


Figure 2.4: Definition of A_{vb}^k, B_{pb}^k at boundary site $s = (vb, pb)$, the slant region indicating the vacuum on the right side of the interface, with the left bulk given by the quantum double, $D(G)$. $A_{vb}^k |\alpha_1, \alpha_2, \alpha_3\rangle = |k\alpha_1, k\alpha_2, k\alpha_3\rangle$, $B_{pb}^k |\alpha_3\rangle = \delta_{k, \alpha_3} |\alpha_3\rangle$.

Therefore, the Hamiltonian, H_{qdb} in the presence of boundaries reduces to Eq. 2.8

$$H_{qdb} = - \sum_{v \in B} A_v - \sum_{f \in B} B_f - \sum_{vb \in B'} A_{vb}^K - \sum_{pb \in B'} B_{pb}^K \quad (2.8)$$

where B denotes the bulk and B' denotes the boundary.

Anyon Condensation

In this section, we study the behavior of the anyons at a given boundary. Given a particular boundary, a particular excitation can either *condense* or *non-condense*, that is in the former the excitation gets identified at the vacuum while in the latter the excitation is retained at the boundary. The

excitations are given by some irreps as defined above and we further define a irrep with respect to a given boundary. The (non)-condensing nature of an excitation is given by the (negative) positive sign of the inner product of the characters of the above irreps. We leave the details to Ref. [40] while reproducing the main results in the Appendix. A.

2.2.2 Generalized boundaries conditions

Generalized boundaries between quantum double and vacuum:

In the previous section, we introduced the boundary interfaces as being decorated by the elements of the subgroup, $K \subseteq G$. This boundary condition can further be generalized to include other boundaries by considering the subgroup K along with non-trivial 2-cocycle of K . We define a 2-cocycle of K as follows

Definition 2.2.1. *Let $\phi : K \times K \rightarrow \mathbb{C}$ be a function such that for every $k, l, m \in K$ we have*

$$\phi(kl, m)\phi(k, l) = \phi(k, lm)\phi(l, m). \quad (2.9)$$

then ϕ is called a 2-cocycle of K .

With the introduction of 2-cocycle, we further modify the A_v^k operator as in Fig. 2.5 which now includes a scaling factor dependent on 2-cocycle, ϕ , of K .

$$A_{v_0}^k \begin{array}{c} \vdots \\ \leftarrow |z\rangle \\ \bullet v_0 \\ \rightarrow |x\rangle \\ \vdots \end{array} = \phi(k, x)\phi(k, y)^{-1} \begin{array}{c} \vdots \\ \leftarrow |kz\rangle \\ \bullet v_0 \\ \rightarrow |kx\rangle \\ \vdots \end{array} \begin{array}{c} \vdots \\ \leftarrow |y\rangle \\ \bullet v_0 \\ \rightarrow |ky\rangle \\ \vdots \end{array}$$

Figure 2.5: Modified definition of $A_{v_0}^k$ at boundary site $s = (v_0, p_0)$ scaled by the 2-cocycle, ϕ .

Two 2-cocycles ϕ and ϕ' are said to be equivalent if there exists an arbitrary function $\alpha : K \rightarrow \mathbb{C}$ such that

$$\phi'(k, l) = \alpha(kl)^{-1}\alpha(k)\alpha(l)\phi(k, l)$$

where $k, l \in K$. We denote the set of equivalent 2-cocycles by $H^2(K, \mathbb{C})$. To summarize, given a quantum double, $D(G)$, the boundaries between $D(G)$

2.3 Quantum Double, $D(Z_2)$: Toric code model

and vacuum are characterized by subgroup, K of G along with the non-trivial 2-cocycles $H^2(K, \mathbb{C})$ whose Hamiltonian is given by Eq. 2.8 with A_v^K operators being modified as above to include the scaling due to the 2-cocycle. The excitations in the bulk are still given by the irreps as introduced earlier, with the irrep with respect to the given boundary now including the information of the 2-cocycle and therefore the condensation of a particular excitation is given by inner product of the characters of the irreps, as defined earlier, for more details see Appendix. A

Generalized domain walls:

In this section, we extend and generalize the above introduced boundary conditions between a quantum double and vacuum to define an interface between two quantum doubles. Consider a boundary interface as in Fig. 2.4 separating the quantum double $D(G_1)$ on the left and the vacuum on the right is now replaced by a quantum double, say $D(G_2)$. The above interface, also known as a *domain wall*, is characterized by the subgroup, $U \subseteq G_1 \times G_2$ along with a 2-cocycle, $\varphi \in H^2(U, \mathbb{C})$. That is the domain walls can be perceived as the boundaries between the lattice decorated by the quantum double $D(G_1 \times G_2)$ and vacuum. Following the earlier recipe, the excitations are given by the irreps of the product double, i.e., the excitations are given by the product of the individual excitations and the condensation rules are obtained by inner product between the characters associated to the product double and the boundary. The condensation properties of the folded quantum double can also be perceived as the tunneling of excitations through the double wall in the unfolded equivalent. For example, let us denote one of the excitations of $D(G_1)$ and $D(G_2)$ by A_l and B_r respectively. The excitation of the product double is given by $A_l B_r$ and using the condensation rules let us assume that the above composite excitation condenses on the interface between the product double and vacuum, that is in the folded version $A_l B_r$ is identified as 1 on the boundary. In the unfolded version, this can be perceived as A_l being identified as B_r as it passes through the domain wall.

2.3 Quantum Double, $D(Z_2)$: Toric code model

In this section, we realize the earlier introduced toric code model reformulated as $D(Z_2)$ quantum double model. We consider a square grid graph, i.e., a square lattice, tiled on a torus realizing periodic boundary conditions, with a spin-1/2 attached to each edge decorated by a group element, $|g\rangle$, where

$g \in Z_2^+$ (the group of integers under addition modulo 2). With the order of the group being 2 and also the group being abelian leaves the orientation of the edges irrelevant, allowing us to choose undirected edges for the underlying graph. We proceed to define the Hamiltonian on the above decorated graph, to this extent we note that the $L^g(j, s)$ operator introduced earlier reduces to σ_x operator acting on the spin on edge j . The A_v operator, as in Eq. 2.4 reduces as follows

$$\begin{aligned} A_v &= \frac{1}{2}(A_s^0 + A_s^1) \\ &= \frac{1}{2}(\mathbb{1} + \prod_{i \in v} \sigma_x^i) \end{aligned} \tag{2.10}$$

whereas the B_f operator, as in Eq. 2.4 reduces as follows

$$\begin{aligned} B_f &= B_s^0 \\ &= \sum_k \prod_{j \in k} P_j \end{aligned} \tag{2.11}$$

where k is the collection of four tuple (g_1, g_2, g_3, g_4) such that their sum is equal to identity, 0, of the group Z_2 with P_j being projector onto $|j\rangle$, where $j = 0, 1$. For instance, $(1, 0, 1, 0)$ is a valid tuple contributing to the sum with the product given by $P_1 P_0 P_1 P_0$ where $P_0 = \frac{1+\sigma_z}{2}$, $P_1 = \frac{1-\sigma_z}{2}$. Therefore, the B_f operator reduces as follows

$$B_f = \frac{1}{2} \prod_{j \in f} \sigma_z^j \tag{2.12}$$

Therefore, we retrieve the toric code Hamiltonian, as in Eq. 1.2, by substituting the above A_v , B_p operators into Eq. 2.5. The excitations of $D(Z_2)$ are characterized by the irreps, π , of the centralizers of the conjugacy class, \bar{a} , of Z_2 , denoted by the pair (\bar{a}, π) . The conjugacy classes of Z_2 are given by $\{\bar{0}, \bar{1}\}$ whose centralizers form a Z_2 group. The character table of Z_2 has a two irreps: one trivial and the other non-trivial denoted by π_1 and π_2 , therefore the excitations in the $D(Z_2)$ are given by $(\bar{0}, \pi_1)$, $(\bar{0}, \pi_2)$, $(\bar{1}, \pi_1)$, $(\bar{1}, \pi_2)$ which map to the vacuum, A_v violations (e), B_p violations (m) and the fusion of A_v , B_p violations (f). The fusion rules can be computed using the Verlinde formula using the entries of S -matrix indexed by the irreps, as in Appendix. A.

Having retrieved the main ingredients of the toric code model we introduce various boundaries of the toric code model. Here, we consider the interfaces between $D(Z_2)$ -vacuum and the domain walls between $D(Z_2)$ - $D(Z_2)$. To facilitate the construction of the open boundaries we consider either a cylinder or a planar surface tiled by a square lattice with undirected edges.

2.3.1 Boundary I: Interface between $D(Z_2)$ and vacuum

The boundaries are characterized by the subgroup, $K \subseteq Z_2$ along with a 2-cocycle, $\phi \in H^2(K, \mathbb{C})$. The 2-cocycles of the subgroups of Z_2 are trivial and therefore the interface is decorated with elements of the subgroup, $K = \{0, Z_2\}$ giving rise to the following boundary conditions

- $K = \{0\}$, Identity as boundary
- $K = Z_2$, Group as boundary

For the cylinder geometry/planar geometry we can decorate the boundaries with a mixture of the above boundary conditions and this leads us to mixed boundary conditions. For the rest of the analysis, we consider a cylinder geometry with open boundaries on the either end tiled by a square lattice decorated with Z_2 in the bulk, this could be easily be extended to planar surfaces which sport no periodicity, leading to the well known surface codes [51, 52, 34].

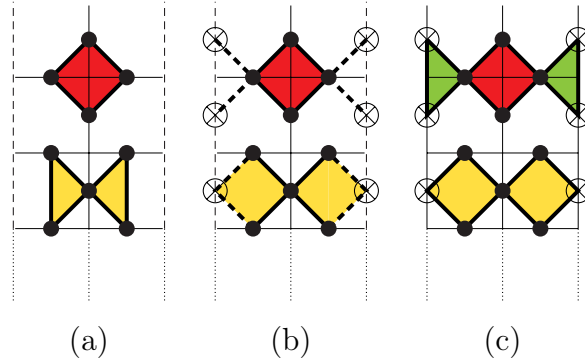


Figure 2.6: Identical boundary conditions on the cylinder (a) Identity as boundary on both ends with no boundary spins (b) Identity as boundary case with additional spins on the boundary projected onto identity, $|0\rangle$ (c) Group as boundary case decorated with elements of Z_2 .

$K = Z_2$, Group as boundary:

We decorate either of the open boundary edges with elements from the subgroup $K = Z_2$ as in Fig. 2.6(c). The A_v , B_p operators in the bulk are as in Eq. 2.10, 2.12 respectively, while at the boundary A_v^K , as in Eq. 2.7 at the

boundary reduces to A_v as in Eq. 2.10 given by $\prod \sigma_x$ where the product runs over the three edges attached to the boundary vertex. The B_p^K operator at the boundary reduces to identity as it is decorated by elements of Z_2 . Therefore, substituting the above operators in Eq. 2.8 we have the Hamiltonian, H_{gr} , where the boundary is decorated by the elements of the group Z_2

$$\begin{aligned} H_{gr} &= - \sum_{v \in B} A_v - \sum_{f \in B} B_f - \sum_{vb \in B'} \prod_{i \in vb} \sigma_x^i - \sum_{pb \in B'} \mathbb{1} \\ &= - \sum_{v \in B} \prod_{j \in v} \sigma_x^j - \sum_{f \in B} \prod_{k \in f} \sigma_z^k - \sum_{vb \in B'} \prod_{i \in vb} \sigma_x^i \end{aligned} \quad (2.13)$$

By comparing the character of the irrep of the excitations, $\chi_{(\bar{a}, \pi)}$ to the character of the irrep associated with the boundary, $\chi_{(\mathcal{A}(K), \pi)}$, we arrive at the conclusion that the irrep given by $\chi_{(\bar{0}, \pi_1)}$, $\chi_{(\bar{1}, \pi_1)}$ condenses on the boundary, that is, B_p violations (m -excitations) condense on the boundary while A_v violations (e -excitations) are retained at the boundary. In other words, the m -violations are identified with the vacuum, therefore termed as *condensing* excitations, while the e -violations are retained at the boundary, therefore termed as *non-condensing* excitations. This is also easy to perceive from the lattice structure as A_v violations are still possible at the boundary due to absence of the gauge constraints on the boundary spins while the B_p violations can no longer be generated in pairs by the action of σ_x on the boundary spins. The boundary can also be denoted by the direct sum of excitations that condense on it and is given by the label $1 \oplus m$.

$K = \{0\}$, Identity as boundary:

We decorate either of the open boundary edges with elements of the subgroup $K = \{0\}$ as in Fig. 2.6(b). As earlier, the Hamiltonian in the bulk is given by A_v and B_p operators as in Eq. 2.10, 2.12 respectively. The A_v^K at the boundary reduces to $\mathbb{1}$ on every edge, due to Eq. 2.7 while the B_p operator in the bulk which shares an edge with the boundary reduces to

$$B_f^o = \frac{1}{2} (\mathbb{I} \bullet \mathbb{I} \bullet \mathbb{I} \bullet + \sigma_z \bullet \sigma_z \bullet \sigma_z \bullet) \left(\frac{\mathbb{1} + \sigma_z}{2} \right)^\otimes \quad (2.14)$$

where the dots (\bullet) represent the spins in the bulk while the product (\otimes) represent the spin on the boundary. The B_p^K operator at the boundary reduces to the projector, $P_0 = \frac{\mathbb{1} + \sigma_z}{2}$. Therefore, the Hamiltonian, H_{id} with the boundary decorated by the identity of Z_2 is given by

$$H_{id} = - \sum_{v \in B} A_v - \sum_{f \in B} B_f - \sum_{vb \in B'} \prod_{i \in vb} \mathbb{1}^i - \sum_{f \in B'} B_f^o - \sum_{pb \in B''} P_0 \quad (2.15)$$

where B denotes the bulk vertices and faces which do not share an edge with the boundary interface while B' denotes the boundary vertices and bulk faces which share an edge with the boundary, with B'' denoting the edges on the boundary. Ignoring the projected spins on the boundary, as in Fig. 2.6(a) retains all the properties of the above Hamiltonian, Eq. 2.14, and therefore it can be recasted as

$$\begin{aligned}
 H_{id} &= - \sum_{v \in B} A_v - \sum_{f \in B} B_f - \sum_{f \in B'} B'_f \\
 &= - \sum_{v \in B} \prod_{j \in v} \sigma_x^j - \sum_{f \in B} \prod_{k \in f} \sigma_z^k - \sum_{f' \in B'} \prod_{m \in f'} \sigma_z^m
 \end{aligned} \tag{2.16}$$

The B'_f operator is a three body σ_z operator acting on the face adjacent to the boundary, as in Fig. 2.6(a).

As established earlier and in the appendix A, we compare the characters of the irreps associated with the excitations and of the boundary to gain an insight into the condensation properties associated with the particular boundary. In this case, we note that the A_v violations (e -excitations) condense on the boundary, while the B_p violations are retained. Intuitively, from Fig. 2.6(a) due to the absence of edges (gauge constrained, if present, as in Fig. 2.6(b)) there are no B_p violations that can be condensed at the boundary as well there are no vertices that can be violated along the boundary interface. Therefore, the identity as boundary denoted by $1 \oplus e$ has A_v violations condensing on the boundary with the B_p violations being retained.

We note that identity (group) as boundary are referred to as rough (smooth) boundaries in literature [53]. We also note that it is possible to formulate a Hamiltonian with different boundary conditions on either open boundaries of the cylinder leading to a mixed boundary scenario, the details of which, we leave to a later chapter.

2.3.2 Boundary II: Interface between $D(Z_2)$ and $D(Z_2)$

Having analyzed the interfaces between $D(Z_2)$ and vacuum we extend the boundary analysis to interfaces, termed as domain walls between two $D(Z_2)$ quantum doubles. To this extent, we consider the boundaries of the folded product double of $D(Z_2 \times Z_2)$ and vacuum. The boundaries are therefore characterized by the subgroups, $K \subseteq Z_2 \times Z_2$ along with the 2-cocycles, $\varphi \in H^2(K, \mathbb{C})$. To differentiate between the quantum doubles on either side of the interface, we decorate the graph on the left with Z_2^+ group under addition modulo 2 and the right with Z_2^\times group under multiplication modulo 2. The elements of the group Z_2^+ are given by $\{0_+, 1_+\}$ while Z_2^\times are given by

$\{1_\times, -1_\times\}$. We summarize the different possible interfaces along with the excitations that condense on the boundary in the following table and in Fig. 2.7

Boundaries (K, φ)	Condensate on the boundary
$K = \{(0_+, 1_\times)\}$	$1, e_l, e_r, e_l e_r$
$K = \{(0_+, 1_\times), (0_+, -1_\times)\}$	$1, e_l, m_r, e_l m_r$
$K = \{(0_+, 1_\times), (1_+, 1_\times)\}$	$1, e_r, m_l, m_l e_r$
$K = \{(0_+, 1_\times), (1_+, -1_\times)\}$	$1, e_l e_r, m_l m_r, f_l f_r$
$K = Z_2^+ \times Z_2^\times, \text{ Trivial } \varphi$	$1, m_l, m_r, m_l m_r$
$K = Z_2^+ \times Z_2^\times, \text{ Non-trivial } \varphi$	$1, e_l m_r, m_l e_r, f_l f_r$

where e_l, e_r denote the A_v violations (e -excitations) on the left and right side of the domain wall.

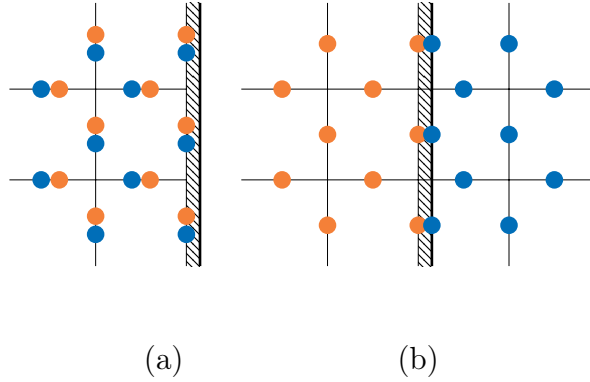


Figure 2.7: (a) Folded version of the product double $D(Z_2^+) \times Z_2^\times$ with the boundary decorated by some subgroup, $K \subseteq Z_2^+ \times Z_2^\times$. (b) Unfolded version of (a).

We note that in the above table the subgroups of order 2, $|K| = 2$, are isomorphic to Z_2 and hence the 2-cocycle is always trivial. The composite condensates, for example $e_l m_r$ can be perceived as e_l being mapped to m_r as it passes through the domain wall. In this context, the interface when decorated with the elements of the subgroup $K = \{(0_+, 1_\times), (1_+, -1_\times)\}$ leads to the condensates $1, e_l e_r, m_l m_r, f_l f_r$ implying that in the unfolded version the excitation type remains unchanged as it passes through the domain wall. In the case of $K = Z_2^+ \times Z_2^\times$ along with non-trivial 2-cocycle, the $A_v(B_p)$ violations on left get mapped to $B_p(A_v)$ violations on the right ($e_{l,r} \leftrightarrow m_{l,r}$).

2.3.3 Summary

To summarize, we introduced the quantum double model, $D(G)$, on a general directed graph tiled on a general periodic manifold. We then introduced the notion of open boundaries which are characterized by the subgroup, $K \subseteq G$, along with a 2-cocycle, $\varphi \in H^2(K, \mathbb{C})$. Having defined the quantum double in a general setting, we retrieve the details of the toric code by casting it as a quantum double of Z_2 . We then analyzed various boundary interfaces between the toric code and vacuum, further extending the notion of boundaries to define domain walls between two toric code quantum doubles. We summarize various boundary conditions introduced for the case of $D(Z_2)$ as in Fig. 2.8 as discussed in Ref. [53].

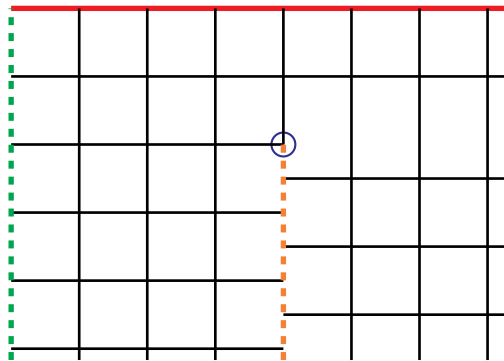


Figure 2.8: Various boundary conditions of the $D(Z_2)$ toric code as in Ref. [53]. Smooth boundary is denoted by red line on the top, rough boundary is denoted by dashed green line on the left, domain wall is denoted by the dashed orange line. There is an additional stabilizer denoted by the blue circle that gives rise to defects of codimension 2 as defined in the above reference.

By comparing the characters of the irreps associated with the excitations and the physical boundary, we have gained insight on whether an excitation condenses or is retained at the boundary, thereby introducing the notion of anyon condensation. Boundaries can also be classified by the anyons that condense on them and thus anyon condensation plays a significant role in understanding of the open boundaries. The notion of anyon condensation and thereby the notion of open boundaries has also been studied in the context of twisted quantum doubles [54], Levin-Wen string net models [53] and also in fractal phases [55] which are beyond the description of formal field theory framework used to classify intrinsic topological order. In the rest of the work, we mainly deal with the different variants of the smooth, rough,

mixed and domain wall boundaries introduced in the context of the $D(Z_2)$ toric code model.

Part II

Robustness of intrinsic topological order in closed systems

Chapter 3

Robustness of topological phases with open boundaries

Robustness of topological order has gathered significance in the recent past in the fields of condensed matter physics and quantum information science. In the former, the focus has been to gain interest into new phases of matter which are beyond the Landau symmetry breaking paradigm, while in the latter the focus has been to realize robust quantum memories. While periodic boundary scenarios in the presence of external perturbation have been explored before as in Refs. [56, 57, 58, 59, 60, 61], the notion of the same for open boundaries remains unexplored. Open boundary scenarios are of significant value both from a theoretical perspective as they exhibit exotic phenomenon such as anyon condensation while on the experimental side [62, 52, 63] open boundaries are easier to realize.

In this part we study the robustness of intrinsic topological order with respect to the ground states of various perturbed toric code Hamiltonians. In this chapter, we consider the toric code Hamiltonian on a cylinder with identical open boundaries on either end in the presence of external perturbation, as in Fig. 3.1. The external perturbation drives the topologically ordered phase to a topologically trivial phase resulting in a quantum phase transition. In the following chapter, we discuss phase transitions induced due to the change in the underlying boundary conditions, resulting in a quantum phase transition between distinct topological phases. In order to create a distinction between the above two notions, in the remaining of the work we term the latter as topological phase transitions. We also note that in the remaining of the work, in order to effectively capture the boundary effects we consider the toric code on a cylindrical geometry whose radius, R , diverges, with its length L remaining finite as we approach the thermodynamic limit

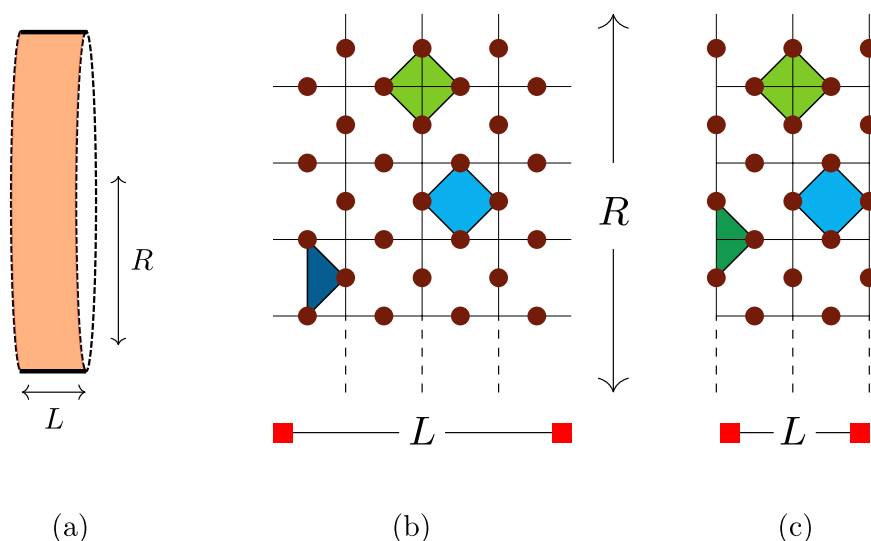


Figure 3.1: Toric code with open boundaries (a) on a cylinder with length L and radius R . (a) Toric code with identity as boundary. (b) Toric code with group as boundary

as in Fig. 3.1.

3.1 Perturbation in the presence of boundaries

We consider the case of open boundary conditions being perturbed by various magnetic fields given by $\sum_i \sigma_z^i$, $\sum_i \sigma_x^i$. We analyze the robustness of topological order when either one of the above perturbations is turned on at a given time. In the following, we introduce the exact Hamiltonians and the Ising mapped versions which help us gain insight into the nature of phase transitions.

3.1.1 Exact Hamiltonians and Ising Hamiltonians

The perturbed Hamiltonians in the physical spin picture, which we refer to as exact Hamiltonians, can be summarized as follows

$$\begin{aligned} H_{grpz(idpz)} &= H_{gr(id)} - h_x \sum_i \sigma_x^i \\ H_{grpx(idpx)} &= H_{id(gr)} - h_z \sum_i \sigma_z^i \end{aligned} \quad (3.1)$$

where H_{gr} , H_{id} are given by Eq. 2.13 and Eq. 2.16 respectively.

3.1 Perturbation in the presence of boundaries

Group as boundary, $K = Z_2$, with $\sum_i \sigma_x^i$ as perturbation

The Hamiltonian is given by H_{grpx} , Eq. 3.1, and as introduced earlier, in the group as boundary case, the B_p violations condense on the boundary. The perturbation, $\sum_i \sigma_x^i$ leaves the A_v space invariant while anti-commutes with the B_p operator, which results in the following relations

$$\begin{aligned} [H_p, A_v] &= 0, \forall v \in \text{bulk}, \\ [H_p, A_{v'}] &= 0, \forall v' \in \text{boundary}, \\ [H_p, B_p] &\neq 0 \end{aligned}$$

We shift to the B_p excitation subspace and identify the center of each face by a spin-1/2, thereby the effective Hamiltonian in the excitation space is given by

$$H_{isgb} = -h_x \sum_{p,q} \mu_p^x \mu_q^x - h_x \sum_{p' \in \text{boundary}} \mu_{p'}^x - \sum_p \mu_p^z. \quad (3.2)$$

The above equation is motivated by the fact that the perturbation generates B_p excitations in pairs in the bulk, resulting in the nearest neighbor Ising interaction, while at the boundary, due to the condensation the excitations can exist independently, resulting in the additional term $h_x \sum_{p' \in \text{boundary}} \mu_{p'}^x$, which breaks the Z_2 symmetry of the transverse field Ising model. The following summarizes the above map between the physical spins and the Ising spins in the excitation basis

$$\begin{aligned} H_{grpx} &= - \sum_p B_p - h_x \sum_i \sigma_x^i \\ &\quad \underbrace{\hspace{10em}} \\ H_{isgb} &= - \sum_p \mu_p^z - h_x \sum_{p,q} \mu_p^x \mu_q^x - h_x \sum_{p' \in \text{boundary}} \mu_{p'}^x \end{aligned}$$

Similarly for identity as boundary when perturbed with $\sum_i \sigma_z^i$ results in a condensing scenario. The perturbation leaves the B_p sector invariant and anti-commutes with the A_v operator, therefore we shift to the excitation space of A_v with the excitations being identified at vertices with a Ising spin-1/2. To summarize, group (identity) as boundary when perturbed with $\sum_i \sigma_{x(z)}^i$

maps to the following Hamiltonian in the excited basis and correspond to the condensing class

$$H_{ci} = -h_p \sum_{i,j} \mu_i^x \mu_j^x - h_p \sum_{k \in \text{boundary}} \mu_k^x - \sum_i \mu_i^z. \quad (3.3)$$

Group as boundary, $K = Z_2$, with $\sum_i \sigma_z^i$ as perturbation

The Hamiltonian is given by H_{grpz} , as in Eq. 3.1. The perturbation, $\sum_i \sigma_z^i$ leaves the B_p space invariant while anti-commutes with the A_v operator, which results in the following relations

$$\begin{aligned} [H_p, B_p] &= 0, \forall p, \\ [H_p, A_v] &\neq 0, \forall v \in \text{bulk}, \\ [H_p, A_{v'}] &\neq 0, \forall v' \in \text{boundary}, \end{aligned}$$

We shift to the A_v excitation subspace and identify the center of each face by a spin-1/2, thereby the effective Hamiltonian in the excitation space is given by

$$H'_{isgb} = -h_z \sum_{v,w} \mu_v^x \mu_w^x - \sum_v \mu_v^z. \quad (3.4)$$

The above equation is motivated by the fact that the perturbation generates A_v excitations in pairs in the bulk, resulting in the nearest neighbor Ising interaction, while at the boundary, as the excitations are contained and the nearest neighbor Ising interaction is retained. There is no support for isolated excitations at the boundary and the Z_2 symmetry of the Ising model is preserved. The following summarizes the above map between the physical spins and the Ising spins in the excitation basis

$$\begin{aligned} H_{grpz} &= - \sum_v A_v - h_z \sum_i \sigma_z^i \\ &\quad \underbrace{\hspace{1.5cm}} \quad \underbrace{\hspace{1.5cm}} \\ &\quad \downarrow \hspace{0.5cm} \downarrow \\ H'_{isgb} &= - \sum_v \mu_v^z - h_x \sum_{v,w} \mu_v^x \mu_w^x. \end{aligned}$$

Similarly, for identity as boundary case with $\sum_i \sigma_x^i$ as the perturbation results in a non-condensing scenario, where we move to the excitation space of B_p and identify the violations by a spin-1/2 sitting at the center of the

3.2 Characterizing the phase transition

face. To summarize, group (identity) as boundary under $\sum_i \sigma_{z(x)}^i$ map to the following Hamiltonian in the excited basis and correspond to the non-condensing class

$$H_{nci} = -h_p \sum_{i,j} \mu_i^x \mu_j^x - \sum_i \mu_i^z. \quad (3.5)$$

We validate the above results by using the Controlled-NOT mechanism as introduced in Ref. [64], which we summarize in Appendix. B. The CNOT map in the current context, is similar to the case of periodic boundaries, where, in addition to the nearest neighbor Ising interactions it introduces a vacancy and topological spin (associated to the non-trivial loops which project into different ground states as in Ref. [65]). In the case of group as boundary under $\sum_i \sigma_x^i$ perturbation, as in Eq. 3.1, the CNOT-map gives rise to additional terms given by $-h \sum_{p',q'} \mu_{p'}^x \otimes L_x \otimes \mu_{q'}^x$, where p', q' are Ising spins on either side of the boundary with L_x given by $L_x = \prod_{j \in L} \sigma_x^j$ with L being the shorter width of the cylinder, in addition to the vacancy. While in the thermodynamic limit, the contribution of these terms in capturing the criticality remains negligible, though, from a qualitative viewpoint they provide critical insights into the robustness of topological order.

3.2 Characterizing the phase transition

In the previous section, we mapped the perturbed Hamiltonian in the physical spin basis to an effective Ising model in the excitation basis. To gain a better understanding of the phase transition we study the behavior of magnetization, which acts as a local order parameter with respect to the perturbation strength, h .

3.2.1 Non Condensing case

We consider the H_{nci} Hamiltonian, as in Eq. 3.5, at different perturbation strength. In the limit of $h_p \rightarrow 0$ we have a paramagnet while in the other limit of $h_p \rightarrow \infty$ we have a ferromagnet. From the above we also infer that the topologically ordered phase of the exact model gets mapped to the paramagnet in the excitation basis while the topologically trivial phase gets mapped to the ferromagnet. To capture the phase transition we compute the absolute of magnetization, m , and its derivative, susceptibility, χ , given by

$$m = \frac{1}{N} \sum_{i=1}^N \mu_i^x \quad (3.6)$$

$$\chi = \frac{\partial m}{\partial h}$$

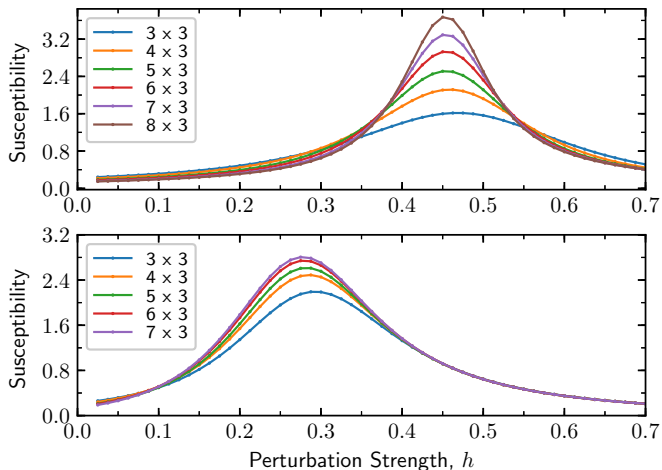


Figure 3.2: Susceptibility of the Ising model equivalent to the (Top) non-condensing case (Bottom) condensing case

where N is the total number of spins.

From Fig. 3.2, we note that the susceptibility curve diverges indicating the presence of a quantum phase transition. To precisely capture the critical strength we perform finite size scaling analysis whose expression is given by, as in Ref. [66]

$$m = N^{-\beta/\nu} \tilde{f}([h - h_c]N^{1/\nu}), \quad (3.7)$$

where h_c is the critical strength, m is the magnetization, N is the system size, ν, β are the critical exponents, \tilde{f} is a scaling function chosen as a degree 6 polynomial. Here m, g, N are known and hence we fit the data to determine the coefficients of the polynomial, \tilde{m} and g_c . From the fit, we note that the critical strength is given by $h_c = 0.453(1)$ and the critical exponents are given by, $\beta = 0.100(7)$, $\nu = 1.13(1)$ which are in good agreement with the critical exponents of the 2D Ising universality class ($\beta = 0.125$, $\nu = 1$) [67].

We note that the topological order in the non-condensing scenario is more robust in comparison to perturbed toric code on periodic boundaries where the critical strength is given by $h_c^{periodic} = 0.328$ [61]. This can be attributed to the fact that quantum fluctuations in the quasi-1D geometry play a significant role in comparison to the 2D case, as the disordered phase of the Ising transition corresponds to the topologically ordered phase and vice-versa. Therefore, cylindrical geometries are more viable avenues to store

3.2 Characterizing the phase transition

quantum memories, though a single qubit less in comparison to two qubits in the case of a torus.

3.2.2 Condensing case

The Hamiltonian for the condensing case is given by H_{ci} as in Eq. 3.4. As described earlier, the Z_2 symmetry of the conventional transverse field Ising Hamiltonian is broken as soon as the perturbation is turned on, this is due to the condensation properties of the excitations at the boundary. That is, with the introduction of the perturbation localized excitations appear at the boundary, with the break in symmetry hinting at the fact that the condensing scenarios do not give rise to robust topological phases. We further confirm the above picture by analyzing the topological coupling term obtained via the CNOT map, see Appendix. B. The effective Ising Hamiltonian including the above topological coupling is given by Eq. 3.8

$$\begin{aligned}
 H_{ci}^{\text{eff}} = & - \sum_i \mu_i^z - h_p \left(\sum_{i,j} \mu_i^x \mu_j^x + \sum_{k \in \text{boundary}} \mu_k^x \right. \\
 & \left. + \sum_{(p,q)} \mu_p^x \otimes L_x \otimes \mu_q^x \right). \tag{3.8}
 \end{aligned}$$

By performing a mean-field decoupling on the topological coupling term, we obtain $h_p \langle \mu_p^x \rangle \langle \mu_q^x \rangle L_x$. In the condensing scenario, as soon as the perturbation is turned on, the expectation value is non-zero thereby lifting the topological degeneracy resulting in a topologically trivial phase. In the non-condensing scenario, the expectation value is zero for $h < h_c$ thereby the ground state degeneracy remains intact and the phase is topologically ordered, in the case of $h > h_c$, the expectation value is again zero due to the ferromagnetic interactions and the phase is topologically trivial. Therefore, though in the thermodynamic limit the contribution of these terms is quantitatively negligible, from a qualitative perspective these Ising mapped models provide deep insight into the robustness of topological order.

Having analytically established the fact that topological phases are not robust in condensing scenarios, we turn to numerical analysis to consolidate the above picture. As in the non-condensing case, we compute the susceptibility as a function of the perturbation strength and observe that there is no divergence with increase in the system size, as in Fig. 3.2. Therefore, we revert back to the original model and study various numerical signatures of topological order. Given that we have already characterized the phase transition in the non-condensing scenario, allows us to not only benchmark our

numerics but also verify the above established analysis with respect to the condensing scenario.

3.3 A Closer look at the Condensing case

In this section, we verify the already established analysis for the condensing scenarios by examining the following signatures which encode the notion of topological order

1. Breaking of the ground state degeneracy
2. Topological Entanglement Entropy
3. Minimal Entangled States (Two minima in topologically ordered phase to one in trivial phase)

3.3.1 Ground state degeneracy, ΔE :

As introduced earlier, one of the important characteristics of topological order is the ground state degeneracy. For the case of toric code on a cylinder with identical boundaries, it has been established that the ground state degeneracy is two [68]. In the current analysis, setting the perturbation strength to zero should give us a degeneracy in the low energy spectrum. The degeneracy can be captured by analyzing the difference of the least two energy levels, (ΔE) i.e., the least two eigenvalues of the Hamiltonian spectrum. For the non-condensing case, as already established the critical strength is around 0.45, therefore we expect to observe a degeneracy in the low energy spectrum ($\Delta E \approx 0$) up to the above critical strength. With reference to Fig. 3.3, for the non-condensing scenario, we observe the above expected behavior in the energy gap, ΔE , of the least two energy levels. That is, ΔE is suppressed with increase in system size up to the critical strength and beyond the critical strength the energy gap starts to widen. Extrapolating to the thermodynamic limit, in the non-condensing case the ground state manifold is degenerate up to the critical strength, h_c , implying that the topological phase is robust up to h_c . Comparing the condensing case to the non-condensing case, as in Fig. 3.3 we note that there is no suppression in ΔE with increase in system size, rather $\Delta E > 0$ as soon as the perturbation is turned on. This is in agreement with the earlier established analysis, that in the condensing scenario there are no robust topological phases. The results in Fig. 3.3(a), (b) correspond to the case of identity as boundary with suitable perturbation resulting in non-condensing and condensing scenarios. As a consistency check

3.3 A Closer look at the Condensing case

we also compute ΔE for the case of group as boundary with perturbation resulting in condensing scenario as in Fig. 3.3(c) and note that ΔE is greater than zero as soon as the perturbation is turned on.

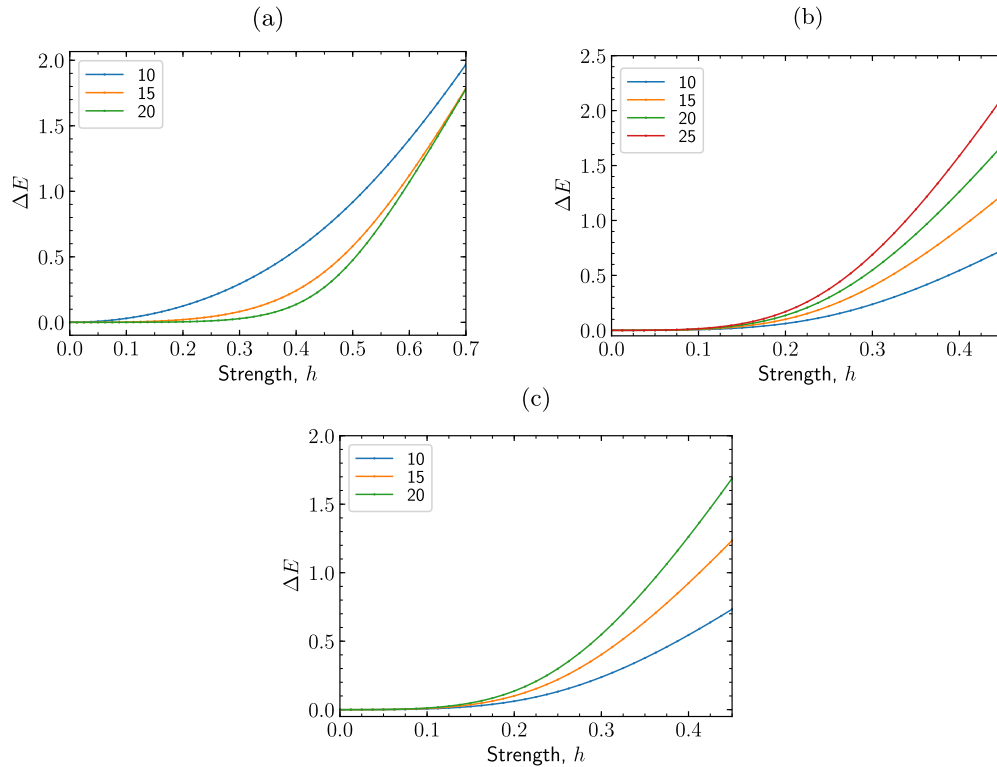


Figure 3.3: Energy Difference, ΔE , as function of the perturbation strength, h , with the identity as boundary perturbed by a relevant magnetic field resulting in (a) non-condensing (b) condensing scenarios. (c) ΔE as a function of the perturbation strength, h , with group as boundary perturbed by a relevant magnetic field resulting in a condensing scenario.

3.3.2 Topological Entanglement Entropy, γ :

As introduced earlier, an important diagnostic for topological order is TEE. As established earlier TEE, γ , is given by the constant sub-leading term in the computation of the von-Neumann entropy, S_A of a region A

$$S_A = aL - \gamma \quad (3.9)$$

where L is the length of the cut.

To compute γ , we consider a cut around the surface of the cylinder which includes the boundary, as in Fig. 3.4. We could have chosen a cut completely in the bulk but this would be ineffective as it would not capture the boundary effects (rather it would capture the boundary effects twice since $S_A = S_{A'}$). We briefly motivate the method as in Ref. [14] to compute γ . As our thermodynamic limit is given by $R \rightarrow \infty$ while L being fixed, that is the system size scales with the radius of the cylinder, so the entanglement cut scales with the radius of the cylinder. To compute TEE, γ , at a given perturbation strength, h , we compute the entropy with respect to the boundary cut and fit S_A versus R for different system sizes. The y-intercept of the linear fit results in the topological term, γ .

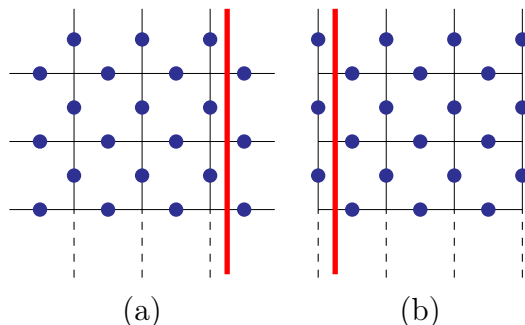


Figure 3.4: Different cuts used for the computation of entropy. (a) Cut for identity as boundary (b) Cut for group as boundary. The region used for the computation of entropy always includes the boundary and it can be either the region to the left or right of the cut as $S_A = S_{A'}$. For computational purposes, we choose the region to the right of cut in (a) and left of the cut in (b) for computing the entropy.

As in the earlier discussion, we begin by re-establishing the fact that there exists a robust topological phase in the non-condensing scenario using TEE. To this extent, we consider the identity as boundary Hamiltonian under relevant perturbation ($\sum_i \sigma_x^i$) resulting in a non-condensing scenario. To extract the TEE, we follow the above detailed procedure i.e., we compute the entropy for different system sizes with the entropy cut scaling with the radius, R , of the cylinder. For a given perturbation strength, h , we plot the entropy, S_A as a function of R and then compute the TEE (y-intercept) as in Fig. 3.4(a). From Fig. 3.4(b), we see that up to a strength of $h = 0.45$, the TEE is around $\log 2$ and it starts to deviate for higher perturbation strength which is in good agreement with the critical strength obtained from susceptibility divergence implying that the TEE is an effective parameter in

3.3 A Closer look at the Condensing case

detecting topological phases. From Fig. 3.4(b) we observe a dip in the TEE. We attribute the dip in the TEE around the transition point to the finite size effects which are particularly strong around the criticality.

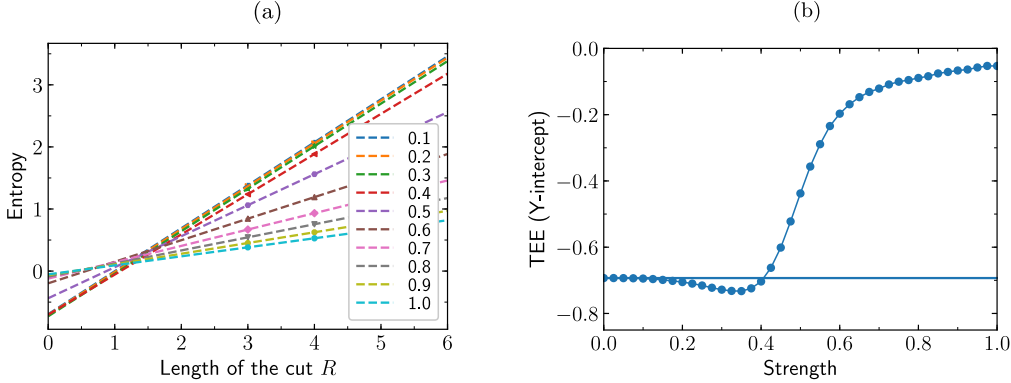


Figure 3.5: Extracting TEE in the non-condensing case. (a) For a given strength, we consider cuts of $R = 3, 4$ for computing the entropy, S_A , where region A is as in Fig. 3.4 and then fit S_A versus R to extract the TEE, which is the y-intercept of the fit. (b) TEE at different perturbation strengths. As the perturbation strength is increased, TEE scales from $\gamma = \log 2$ to $\gamma=0$, signaling a phase transition.

From the above analysis, it is evident that TEE is an effective tool in detecting a quantum phase transition involving a topological phase. We now turn to the case of condensing scenario, where we have analytically established that the phase is trivial as soon as the perturbation is turned on. To this end, we consider the identity as boundary Hamiltonian under a relevant perturbation, $\sum_i \sigma_z^i$, which gives rise to the condensing scenario. We compute γ using the method as established earlier for the non-condensing scenario which results in Fig. 3.5. From the above figure, it is clear that TEE drops to zero as soon as the perturbation is turned on, which is in strong agreement with the earlier established analysis. We further consolidate the above result by considering the other condensing scenario, i.e., group as boundary Hamiltonian with σ_x perturbation. From Fig. 3.7(a), (b), it is evident that the TEE drops to zero as soon as the perturbation is turned on.

In this section, we have thus established that Topological Entanglement Entropy, γ , is effective in detecting a quantum phase transition involving topological and trivial phases. To summarize, for the non-condensing scenario, we have reconfirmed the robustness of topological phase in the presence of a relevant perturbation while for the condensing scenario we have

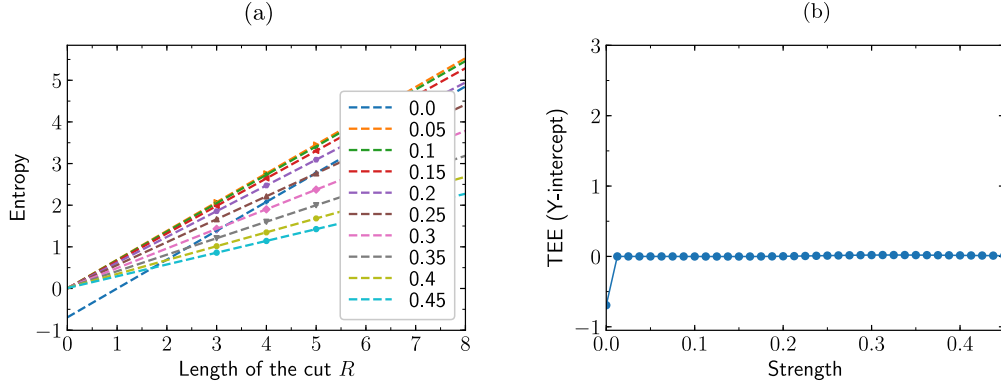


Figure 3.6: Extracting TEE in the condensing scenario with identity as boundary under σ_z perturbation. (a) For a given strength, we consider cuts of $R = 3, 4$ for computing the entropy, S_A , where region A is as in Fig. 3.4(a) and then fit S_A versus R to extract the TEE, which is the y-intercept of the fit. (b) As soon as the perturbation is turned on, the TEE drops to zero.

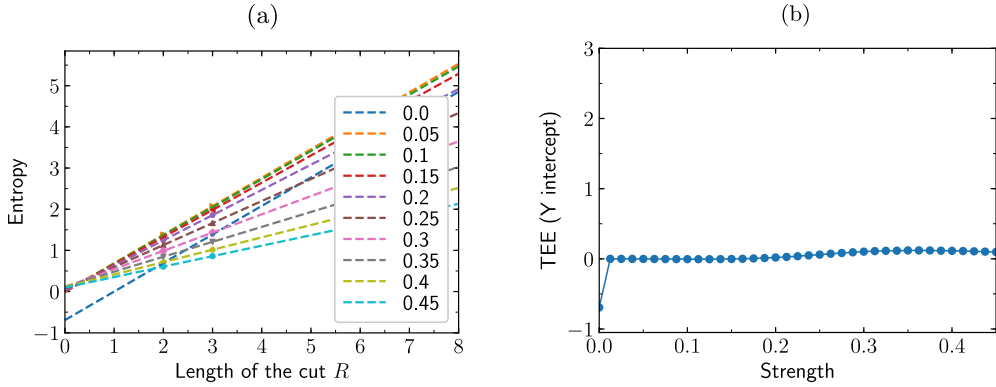


Figure 3.7: Extracting TEE in the other condensing scenario with group as boundary under σ_x perturbation. (a) For a given strength, we consider cuts of $R = 2, 3$ for computing the entropy, S_A and extract TEE as outlined above. (b) As in Fig. 3.6(b), TEE drops to zero as soon as the perturbation is turned on.

analytically and numerically consolidated the fact that the topological phase is trivial as soon as the perturbation is turned on. We note that, though we have been successful in extracting the TEE, the cut used in the current context might not always lead to the expected TEE in other scenarios [69]. In addition, we also note that choosing a cut along the length of the cylinder

connecting both the boundaries also leads to ambiguous results. Therefore, the choice of the cut is particularly important and is highly context specific. In the following part, we aim to use these results to benchmark one other method which is capable of detecting topological phases.

3.3.3 Minimal Entangled States

Modular- S and T matrices which encode the braiding statistics are central to the theory of topological order. The general outline of constructing modular matrices given a Hamiltonian has been extensively discussed in the Refs. [15, 16, 18]. Minimal Entangled States (MES) are central to the above numerical strategy, these states are obtained by observing the Renyi-2 entropy of the region trapped inside a non-trivial cut of the underlying manifold. In the current scenario, we have one non-trivial loop encircling the circumference of the cylinder and we use this to detect the states which are minimally entangled. In the limit of $h = 0$, we know that these are two in number while for higher values in the topologically trivial phase we have a single MES. This change in MES can therefore be used to detect quantum phase transitions as in the condensing scenario. The outline of the numerical procedure to detect phase transitions via MES for the case of H_{idpz} is as follows:

1. We begin with the linear superposition of ground states (as the ground state manifold is degenerate), $c_1|\psi_1\rangle + c_2e^{i\phi}|\psi_2\rangle$, where $|\psi_1\rangle, |\psi_2\rangle$ are the ground states with $c_2 = \sqrt{1 - c_1^2}$ and $0 \leq c_1 \leq 1, 0 \leq \phi < 2\pi$.
2. We compute c_1, ϕ such that the renyi 2-entropy given by $S_2 = -\log(\text{Tr}(\rho_A^2))$ is minimized.
3. By observing that the minima occur at $\phi = 0, \pi$, we can effectively minimize the entropy with c_1 as the parameter by fixing ϕ either at 0 or π .
4. We compute the strength at which the minima disappears (by observing the behavior of c_1) for different system sizes and thereby compute the critical strength in the thermodynamic limit by performing finite size analysis.

We compute the entropy as a function of (c_1, ϕ) as in Fig. 3.8 at various perturbation strength. As outlined above, we note that the minima occur at $\phi = 0, \pi$. Instead of considering the two parameter optimization, we optimize with respect to c_1 for different perturbation strength, as in Fig. 3.9 while considering the strength at which the minimum collapses as the critical

strength for a given system size. From Fig. 3.10, by performing finite size analysis we infer that the critical strength at which the transition occurs is given by $0.12(1)$ which is off from the expected value of zero. Therefore, we conclude that in this case, the MES method fails to effectively detect the critical strength and thereby is inaccurate in quantifying the robustness of topological phases leading to qualitative incorrectness by classifying a trivial phase as ordered phase.

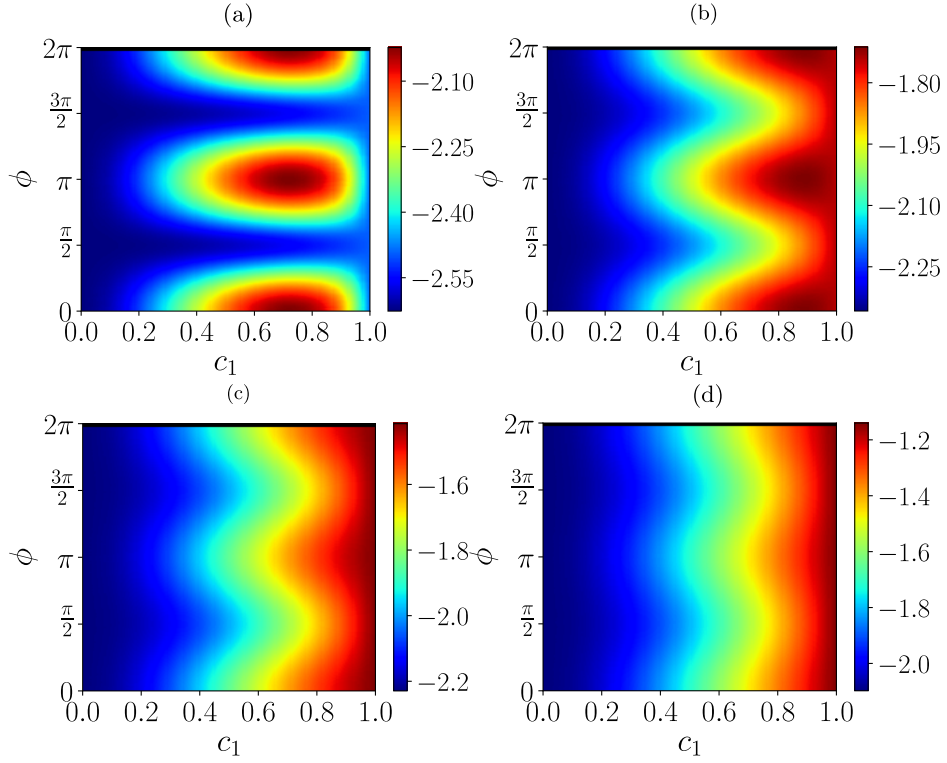


Figure 3.8: Negative of Renyi-2 entropy of the state $|\eta\rangle = c_1|\psi_1\rangle + c_2e^{i\phi}|\psi_2\rangle$ depending on c_1 and ϕ at a perturbative strength of (a) $h = 0.15$, As the perturbation is increased to (b) $h = 0.25$, (c) $h = 0.29$, and at (d) $h = 0.33$, we notice that the two minima collapse minimum at $\phi = 0, \pi$. ($N=20$ spins)

3.3 A Closer look at the Condensing case

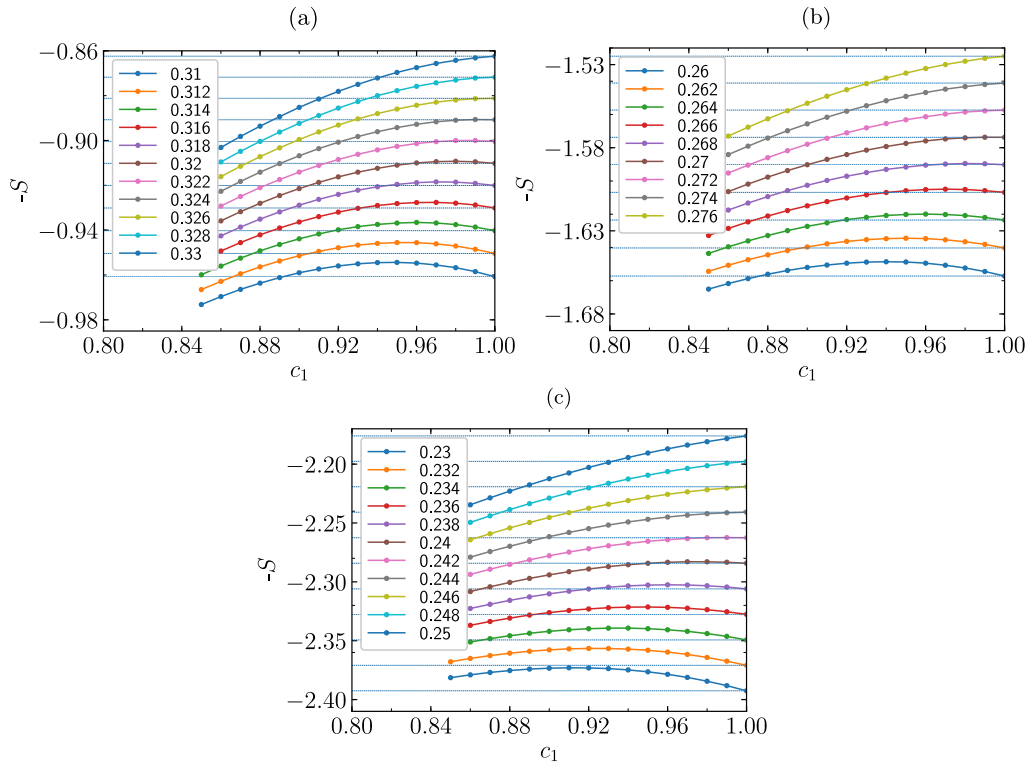


Figure 3.9: Renyi-2 entropy versus c_1 at different strengths, captured for different lattice sizes (a) 15, (b) 20, (c) 25. In the case where the entropy at $c_1=1$ forms a tangent to the entropy versus c_1 curve results in the critical strength due to the disappearance of the second minima.

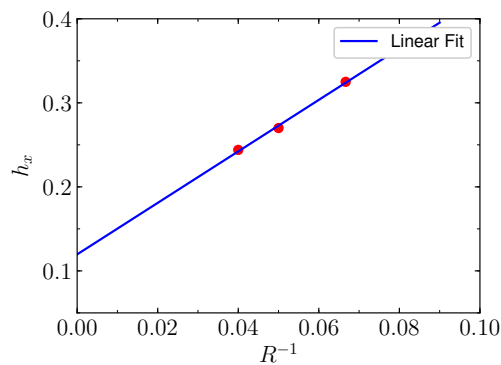


Figure 3.10: Finite size scaling of the critical strength where the second minimum in the Renyi-2 entropy disappears.

Chapter 4

Robustness of topological phases to underlying boundary conditions

In the previous chapter, while having analyzed the quantum phase transition involving topological and trivial phases, in this chapter we introduce quantum phase transitions between two distinct topological phases, leading to the introduction of topological to topological phase transitions (TTPTs) [18, 70, 71, 72]. We consider a parameterized Hamiltonian which at either ends reduces to a frustration-free toric code Hamiltonian with different boundary conditions. In this chapter, we analyze various scenarios where the above Hamiltonian interpolation [73] connecting two different Hamiltonians induces a TTPT.

4.1 Distinct Boundary conditions: Distinct Topological phases

In this section, we would like to establish the fact that each boundary condition gives rise to a unique topological phase due to the condensing properties at the boundary. We define the open boundaries on the cylinder in the limits introduced previously, i.e., L being fixed and $R \rightarrow \infty$, that is the boundary scales with system size. We also note that due to the mixing of different anyonic sectors, the mapping to the equivalent Ising models is not as straightforward as in the earlier case and therefore, we restrict our analysis to the exact models. Consider two topological phases, say T_1, T_2 , with different open boundary conditions characterized by the same topological order i.e.,

the topological order in the bulk is locally indistinguishable (TEE remains invariant) while the open boundaries are decorated by different subgroups. We now introduce the notion of uniqueness of a topological phase according to the following theorem as in Ref. [11]

Theorem 4.1.1 (Equivalence of topological phases). *Two gapped ground states, belong to the same phase if and only if they are related by a local unitary (LU) transformation.*

Consider the ground states of the Hamiltonians which encode the above topological phases T_1, T_2 as $|\psi_{t1}\rangle, |\psi_{t2}\rangle$ respectively. If the two topological phases T_1, T_2 were equivalent then according to the above theorem it would imply that there exists a local unitary transformation connecting the states $|\psi_{t1}\rangle$ and $|\psi_{t2}\rangle$. This would imply that the excited states generated due to the action of some local unitary are equivalent, implying that the condensation properties at the distinct boundaries of T_1 and T_2 are equivalent up to a unitary. The above scenario is not physically feasible as the unitary maps a condensing excitation to a non-condensing excitation or vice-versa. Therefore, two different physical boundaries give rise to distinct topological phases. For example, consider the case of toric code on a torus being mapped to toric code on a cylinder with mixed boundary conditions. The ground state degeneracy in the periodic boundary conditions is four while on a cylinder with mixed boundaries is non-degenerate. The change in degeneracy is already an indication of the presence of a transition point. Using the above arguments, if they belonged to the same phase it would imply the existence of unitary connecting the degenerate ground space of the former to the non-degenerate ground state of the latter. The existence of a local unitary would also imply that, condensation which is favored in the mixed boundary conditions is also possible in the periodic boundary case where such a phenomenon is physically infeasible due to the absence of boundaries which support condensation. Therefore, due to the absence of local a unitary connecting the ground states the two phases though topologically ordered are yet distinct topological phases. The above analysis can also be extended to case of mapping a cylinder with identical boundaries on either side to a different boundary conditions on either side. The degeneracy in this case is the same, but invoking the above argument if there exists a local unitary then it would mean that condensation is promoted at a boundary where it is not supported. Therefore, due to the absence of the local unitary transformation connecting the ground states, though degenerate and topologically ordered, they give rise to distinct topological phases.

The fact that different boundary conditions refer to distinct topological phases can be re-established observing the ground states of different bound-

4.1 Distinct Boundary conditions: Distinct Topological phases

aries. In general, as mentioned earlier, the ground state of the toric code is given by an equal weight superposition of loop configurations. In this scenario, the loop configurations concerning different boundaries are distinct, thereby giving rise to distinct ground states and further distinct topological phases. For example: consider the ground state of the toric code on a torus and on a cylinder with mixed boundaries, the former can never host open loop configurations as there is no physical boundary supporting anyon condensation while in the latter open loop configurations are possible due to the boundary. In the current context of quasi-1D cylinder (L finite, $R \rightarrow \infty$), the open loop configurations are on the same order of the closed loops and hence cannot be neglected, leading to distinct ground states.

In addition, to further validate the above fact that these topological phases with different boundaries are distinct, we extend the notion of quantum phase transition as in Ref. [74] to the current scenario. In the above reference, the author has introduced the notion of quantum phase transition between two frustration-free Hamiltonians H_A and H_B as follows

Two frustration-free Hamiltonians H_A and H_B belong to different quantum phases if and only if there is no parameterized Hamiltonian $H(\epsilon)$ (with ϵ as the parameter) which connects H_A and H_B without closing an energy gap or changing the number of ground states.

The toric code Hamiltonians with different boundary conditions are frustration free and as there exists no parameterized Hamiltonian which can connect them without closing an energy gap or change in ground state degeneracy are distinct quantum phases. These quantum phases being topologically ordered, implies the Hamiltonian interpolation encodes a topological to topological phase transition (TTPT).

As introduced earlier, in a conventional setting, phase transitions are characterized by spontaneous symmetry breaking where the ground state no longer respects the symmetry of the Hamiltonian. Topological phase transitions are beyond this conventional notion of conventional Landau symmetry breaking principle as the ground state respects the symmetry of the Hamiltonian as we drive across the transition. Though, the ground state respect the symmetries of the Hamiltonian, the symmetries of the excitation space are not always preserved. These accompanying broken symmetries of the excitation space further consolidate the presence of a criticality between two topological phases. For the cases to be introduced in the later sections, we shall analyze the following symmetries of the excitation space, with respect to the toric code model:

Parity Conservation:

The excitations in the toric code with periodic boundaries (with no domain walls) always appear in pairs. Due to the introduction of the various boundary conditions, it is always possible to draw single excitations from the boundary.

Anyonic Symmetry [33, 75]:

One other symmetry in the toric code model is the notion of anyonic symmetry, where the fusion and the braiding rules of excitations remain invariant under the exchange of the labels of the excitations. For the case of toric code with periodic boundary conditions, the anyonic symmetry is retained (to the presence of a domain wall) while in the open boundary context the anyonic symmetry is broken due to the change in fusion rules at the boundary. In other words, denoting the A_v and B_p excitations by e and m respectively, the fusion rules given by $e \times e = 1$, $m \times m = 1$, $e \times m = f$ where f is a fermion, remain invariant under the exchange of e and m , $e \leftrightarrow m$, similarly the braiding rules remain invariant under the exchange.

We note that to encode a TTPT, it is sufficient that either one of the symmetries is broken but it is not necessary that every TTPT is accompanied by a broken symmetry. The above statement can be made more complete, at least in the context of toric code models and may be extended to abelian anyonic systems by imposing additional constraints on the symmetries, which we shall discuss later in this section.

Having introduced the notion of topological phases, their equivalence and also the concept of topological phase transition we now turn to specific realizations of the above induced by varying the boundary conditions of the toric code model. By tuning the A_v , B_p interactions we vary the boundary conditions thereby mapping between different boundary Hamiltonians by interpolation. The general form of Hamiltonian interpolation between Hamiltonians H_1 and H_2 parameterized by the interpolation strength, λ , is given by

$$H(\lambda) = \lambda H_1 + (1 - \lambda) H_2 \tag{4.1}$$

As different boundary conditions encode distinct topological phases we expect to observe a topological phase transition as we vary λ . To keep track of the possible scenarios, we use the ground state degeneracy (\tilde{G}_λ) at either ends of the interpolation to broadly classify the possible transitions into the following classes:

1. $\tilde{G}_{\lambda=0} \neq \tilde{G}_{\lambda=1}$
2. $\tilde{G}_{\lambda=0} = \tilde{G}_{\lambda=1}$

4.2 $\tilde{G}_{\lambda=0} \neq \tilde{G}_{\lambda=1}$

In this section, we analyze phase transitions characterized by the change in the ground state degeneracy at either end of the interpolation. The phase transitions being induced by the change in the boundary conditions encompasses the following cases:

1. Topology variation: The underlying topology is varied by mapping from periodic boundary conditions (on a torus) to mixed open boundary conditions (on a cylinder).
2. Boundary variation: The underlying topology is a cylinder and the boundaries at the open end of the cylinder are varied.

4.2.1 Topology variation: Torus with no domain wall to a cylinder with a mixed boundary

In this section, we map the toric code Hamiltonian on a torus with no domain wall to toric code on a cylinder with mixed boundary conditions. We tune the A_v , B_p operators which effectively break the periodicity of the torus and gives rise to a cylinder with mixed boundary conditions as in Fig. 4.1. The mapping is appropriately scaled by the interpolation strength, λ which gives rise to the Hamiltonian, as in Eq. 4.2

$$\begin{aligned}
 H_{pm}(\lambda) = & - \sum_v A_v^\blacklozenge - \sum_p B_p^\blacklozenge \\
 & - (1-\lambda) \sum_{v'} A_{v'}^\blacklozenge - (1-\lambda) \sum_{p'} B_{p'}^\blacklozenge \\
 & - \lambda \sum_{v'} A_{v'}^\blacktriangleleft - \lambda \sum_{p'} B_{p'}^\blacktriangleright,
 \end{aligned} \tag{4.2}$$

where $A_v^\blacklozenge = \prod_{i=1}^4 \sigma_x^{(i)}$ ($B_p^\blacklozenge = \prod_{j=1}^4 \sigma_z^{(j)}$) act on the four edges attached to the respective vertices (faces) in the bulk, while $A_v^\blacktriangleleft = \prod_{i=1}^3 \sigma_x^{(i)}$ ($B_p^\blacktriangleright = \prod_{j=1}^3 \sigma_z^{(j)}$) act on the three edges attached to the respective vertices (faces) at the boundary, as elucidated in Fig. 4.1(b), (c).

From Eq. 4.2 it is clear that $H_{pm}(0)$ represents the toric code Hamiltonian on a torus, while $H_{pm}(1)$ represents the toric code Hamiltonian on a cylinder with mixed boundary conditions. In the limit of $\lambda = 0$, the ground state degeneracy is four while in the limit of $\lambda = 1$ the ground state manifold is non-degenerate [68]. The change in the ground state degeneracy indicates

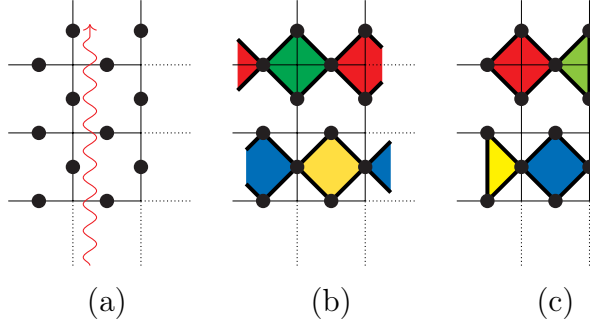


Figure 4.1: (a) The red snake represents the interpolation cut. (b) TC with periodic boundaries i.e., on a torus. (c) TC with mixed boundaries on a cylinder. The red (blue) diamond represents the A_v^\blacklozenge (B_p^\blacklozenge) interaction whose interaction strength is unperturbed by the interpolation. As a result of interpolation the dark green (yellow) full diamonds get mapped to light green (light yellow) half diamonds and thereby the interaction is given by $(1 - \lambda)A_v^\blacklozenge - \lambda A_v^\blacktriangleleft$, $[(1 - \lambda)B_p^\blacklozenge - \lambda B_p^\blacktriangleright]$.

the presence of a critical point at which the transition occurs. The above fact can be further consolidated by the analyzing the break in the symmetries of the excitation space as discussed earlier. In the limit of $\lambda = 0$, both $A_v(e)$ and $B_p(m)$ excitations occur in pairs while in the limit of $\lambda = 1$ it is possible to draw single excitations from the boundary, thereby the parity conservation is broken. In the limit of $\lambda = 0$, anyonic symmetry, $e \leftrightarrow m$, is retained as the labels of $A_v(e)$ excitations can be exchanged with the $B_p(m)$ excitations, while at the other extremum, $\lambda = 1$, anyonic symmetry is no longer retained as the boundary condensation distinguishes the different excitations i.e., the boundary at which A_v excitations condense, B_p excitations are non-condensing and vice-versa. If the anyonic symmetry were to be retained then under the exchange it would imply a map between condensing and non-condensing excitations which is not possible. Therefore, the phase transition between the two topological phases is accompanied by broken symmetries of parity conservation and anyonic label exchange.

From the above, the presence of a topological criticality is evident. In an attempt to characterize the transition in terms of the critical strength we numerically analyze the following signatures:

1. Energy gap in the degenerate ground state manifold
2. Topological Entanglement Entropy

3. Expectation value of the open loop operator

Energy gap in the degenerate ground state manifold

As established in the earlier chapter, the gap opening in the degenerate manifold is an effective signature to re-confirm the presence of criticality. Although in the previous chapter, we had analyzed the gap opening to detect a quantum phase transition between topological and trivial phase, in the present scenario gap opening is still a valid signature as the degeneracy in the ground state manifold at the extremal limits of interpolation strength, λ , is distinct. This is easy to see as the ground state both in the limits of $\lambda = 0$ and $\lambda = 1$ can be represented by $\mathcal{N} \prod_v (\mathbb{1} + A_v) |\mathbf{0}\rangle$ where the product is modified to include the vertices in the respective limits. In the limit of $\lambda = 0$, the ground state degeneracy is four due to the non-trivial loop operators which wrap around the legs of the torus, while in the other limit the ground state is unique (the non-trivial loops around the cylinder leave the ground state invariant). Therefore, with increase in the interpolation strength of λ with reference to the Eq. 4.2 we expect to see a gap opening in the low energy manifold, as in Fig. 4.2(a). As in the previous chapter, we observe that the energy gap ΔE between the generate ground states is suppressed until the criticality and then starts to increase with increase in the interpolation strength, λ , as in Fig. 4.2(b). From the derivative of the ΔE we note that the critical interpolation strength is around 0.5, $\lambda_c \approx 0.5$.

Topological Entanglement Entropy

As established previously, topological entanglement entropy, γ , a constant sub-leading term in entropy is a key signature characterizing topological order. We follow the procedure, outlined earlier, in computing γ by considering one of the cuts as in Fig. 4.4. In the limit of periodic boundary, $\lambda = 0$, the cut includes a strip on the torus while in the limit of $\lambda = 1$, the cut includes either one of the boundary with the cut scaling with the radius of the cylinder in the limit of $\lambda = 1$. From Fig. 4.3, we note that the topological entanglement entropy is almost a constant, $\log 2$ for almost the entire domain of the interpolation strength, λ , with some deviations around the criticality which we attribute to finite size effects being predominant around the supposed criticality, $\lambda_c = 0.5$. This is in agreement with previously established result that topological entanglement entropy is ineffective in detecting phase transitions between topological phases exhibiting the same topological order, here in this case Z_2 topological order [18]. In fact, the value of topological entanglement entropy remains almost constant all along the interpolation further justifies

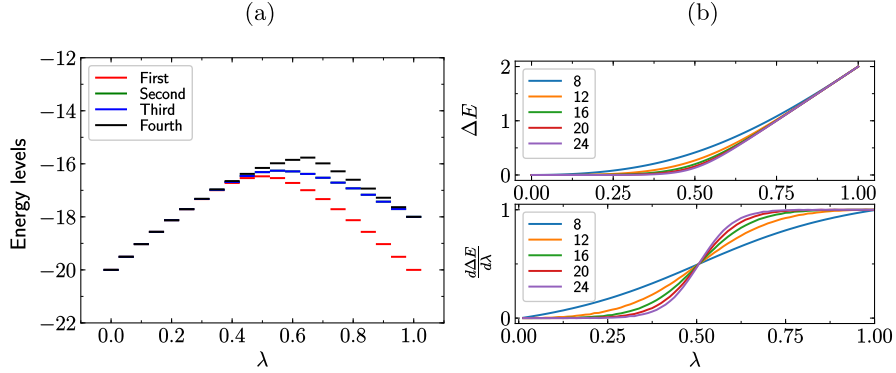


Figure 4.2: (a) The least energy levels for a system size of $N = 20$. At $\lambda = 0$, we see that the ground state spectrum is degenerate, while in the limit of $\lambda = 1$ we have a unique ground state. (b) Difference between the least two energy levels, ΔE (Bottom) $\frac{d\Delta E}{d\lambda}$. As mentioned earlier, the radius, R , of the cylinder scales with the system size, for the rest of the discussion, we fix $L = 2$ and vary R from 2 to 6.

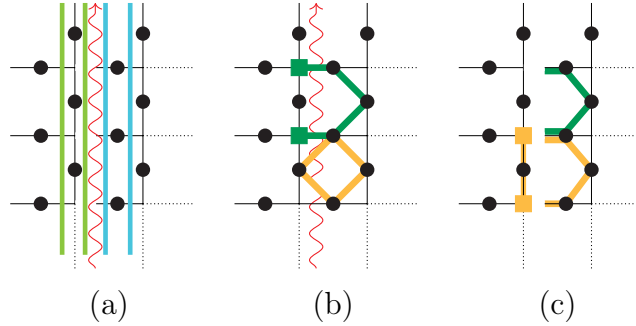


Figure 4.3: (a) The cuts used in the computation of TEE, the green and blue regions capture a strip on the torus while in the mixed boundary scenario, the green region captures the smooth boundary and the blue region captures the rough boundary. (b) TC on a torus, the green string represents the σ_z open-loop operator while the golden string represents the trivial Wilson loop operator. (c) Due to the condensation of the excitation at the boundary the green string reduces to a trivial open string while the Wilson loop splits into two open strings, one identical to the green string while the other sporting two excitations at its ends.

the notion that for all λ the phase is Z_2 topologically ordered.

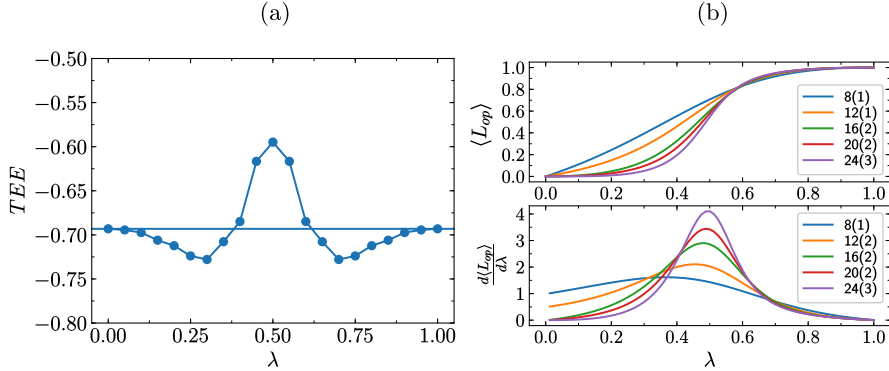


Figure 4.4: (a) Topological Entanglement Entropy (TEE) as a function of the interpolation strength, λ . (b) (Top) Expectation value of the longest open-loop operator (Bottom) Derivative of the expectation value with respect to λ . The labels denote different system sizes with the value in the parentheses indicating the maximal possible separation between the excitations used for the construction of the longest open loop operator.

Expectation value of the open loop operator

From the gap opening in the ground state manifold the presence of criticality is evident and with topological entanglement entropy being ineffective in capturing the same, we introduce a new signature, open loop operators which effectively detect the distinct topological phases. Open loop operators are truncated Wilson loop operators generated by a string of $\sigma_{x(z)}$ operators acting on adjacent spins resulting in a non-local operator. These open loop operators are marked with excitations at their ends, this property can be used to distinguish different phases as the expectation value with respect to the ground state in the extremities of λ is either zero or one depending on whether the excitations condense or non-condense. The TTPTs discussed in the current scenario always involve a boundary so it is always possible to construct a open loop operator involving a boundary, whose expectation value with respect to the ground state vanishes in one phase while is non-zero in the other due to the condensation properties.

In the present context, where we map the toric code from periodic to open boundaries the open loop operator can be constructed by a sequence of σ_z operators, denoted by L_z^r as in Fig. 4.3(c), with the corresponding Wilson loop operator in the context of periodic boundaries as in Fig. 4.3(b). The expectation value of the above open loop operator with respect to the ground state in the limit of $\lambda \rightarrow 0$ is zero, this is due to the fact that the open loop

operator sports two excitations (there is no relevant boundary to support condensation), projecting the ground state into an excited state, thereby the expectation value is zero, $\langle \psi_{gs}^{\lambda=0} | L_z^r | \psi_{gs}^{\lambda=0} \rangle = 0$. While in the limit of $\lambda = 1$, the condensation is supported due to the open boundaries leaving the ground state invariant, therefore the expectation value is one, $\langle \psi_{gs}^{\lambda=0} | L_z^r | \psi_{gs}^{\lambda=1} \rangle = 1$. The choice of the open loop operator is such that the excitations in the non-condensing phase are farthest apart. We refer to this particular choice of the open loop as the longest open loop and is effective in detecting the TTPT. From Fig. 4.4(b) and performing finite size analysis, we infer that the derivative of the expectation value diverges at a critical strength of $\lambda_c = 0.53(3)$, thereby signaling a phase transition.

4.2.2 Boundary variation: Cylinder with rough boundaries to a mixed boundary

In this section, we fix the underlying topology on which the lattice is defined to a cylinder and vary the boundary conditions on one open end of the cylinder leaving the boundary on the other fixed. As above, we consider the toric code Hamiltonian on a cylinder with one end fixed by as a rough boundary while the other end being mapped between rough and smooth boundary conditions. The above mapping results in the interpolation Hamiltonian as in Eq. 4.3

$$\begin{aligned}
 H_{rm}(\lambda) = & - \sum_v A_v^\blacklozenge - \sum_p B_p^\blacktriangleright \\
 & - (1 - \lambda) \sum_{p \in R} B_p^\otimes - (1 - \lambda) \sum_{\otimes \in R} |0\rangle\langle 0| \\
 & - \lambda \sum_{v \in R} A_v^\blacktriangleleft - \lambda \sum_{p \in R} B_p^\blacklozenge,
 \end{aligned} \tag{4.3}$$

where A_v^\blacklozenge , B_p^\blacklozenge , A_v^\blacktriangleleft , B_p^\blacktriangleright are as defined in previous section. Unlike the Hamiltonian in the previous section, where the boundary terms did not include addition spins, here we decorate the interpolating boundary with additional spins to realize the mapping. The additional spins included at the interpolating boundary (denoted by \otimes as in Fig. 4.5(a)) give rise to additional terms of the projector $|0\rangle\langle 0|$ and B_p^\otimes as in the Eq. 4.3, with B_p^\otimes given by

$$B_p^\otimes = \frac{1}{2} (\mathbb{I}^\bullet \mathbb{I}^\bullet \mathbb{I}^\bullet + \sigma_z^\bullet \sigma_z^\bullet \sigma_z^\bullet) \left(\frac{\mathbb{1} + \sigma_z}{2} \right)^\otimes \tag{4.4}$$

where \bullet indicates the action on the spins from the bulk and \otimes indicates the action on the spin of the interpolating boundary. In the limit of $\lambda = 0$, these terms realize the rough boundary conditions on the interpolating boundary

and the Hamiltonian $H_{rm}(0)$ maps to toric code with rough boundaries on either end. In the other limit of $\lambda = 1$, the Hamiltonian $H_{rm}(1)$ maps to toric code with mixed boundaries, where the projection on the right boundary spins is lifted and B_p^\diamond maps to B_p^\blacklozenge operator. As in the earlier section, the ground state degeneracy at either ends of the interpolation is different, 2 in the case of the identical rough boundaries ($\lambda = 0$) while 1 in the case of mixed boundaries ($\lambda = 1$) signaling the presence of criticality as the interpolation strength, λ , is varied. The phase transition is also accompanied by the break in the symmetries of the excitation space, while in the limit of $\lambda = 0$, the B_p -violations, m , appear in pairs, where as in the limit of $\lambda = 1$, it is possible to draw single B_p excitations due to the smooth boundary on the right, thereby breaking the parity conservation. The anyonic exchange symmetry is not conserved due to the possible condensation at the boundaries, if the symmetry were to be conserved it would immediately imply that the B_p violations condense at the rough boundary which is not supported.

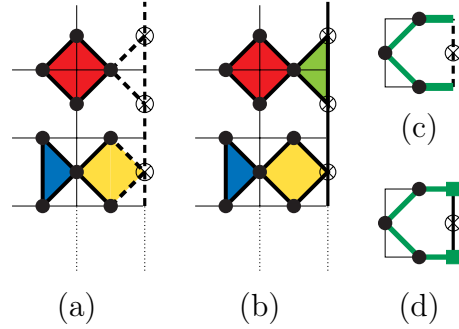


Figure 4.5: (a) TC on a cylinder with a rough boundary on both ends ($\lambda = 0$). Additional spins are added on the right boundary, represented by \otimes . (b) TC on a cylinder with mixed boundaries. In both (a), (b) the red diamond remains unperturbed with action on the attached edges given by A_v^\blacklozenge , the dark blue half diamond also remains unperturbed with the action on the attached edges given by B_p^\blacktriangleright . The yellow diamond in (a) represents the B_p^\diamond which translates to B_p^\blacklozenge in (b), while the uncolored dashed half diamond in (a) maps to A_v^\blacktriangleleft in (b) due to the interpolation. The action of open-loop operator at the boundary at (c) $\lambda = 0$, (d) $\lambda = 1$.

Energy gap in the degenerate ground state manifold

The phase transition is characterized by the change in the ground state degeneracy, at both the extremum the ground state retains the representation

introduced in the earlier section with the product suitably being modified to include the respective vertices. In the limit of $\lambda = 0$, the ground state degeneracy is two, generated by the action of the two non-trivial loop operators: one connecting either boundaries, the other being the loop operator winding the cylinder. In the limit of $\lambda = 1$, the ground state manifold is non-degenerate [68]. As we increase the interpolation strength, λ , as observed in the previous section, there is a gap opening in the degenerate manifold, as in Fig. 4.6(a). We also note that up to the critical interpolation strength, λ_c , there is a suppression in the energy gap, ΔE , of ground state manifold with increase in system size, and results in a qualitatively similar plot as in Fig. 4.2 indicating the presence of criticality around 0.5, $\lambda_c \approx 0.5$.

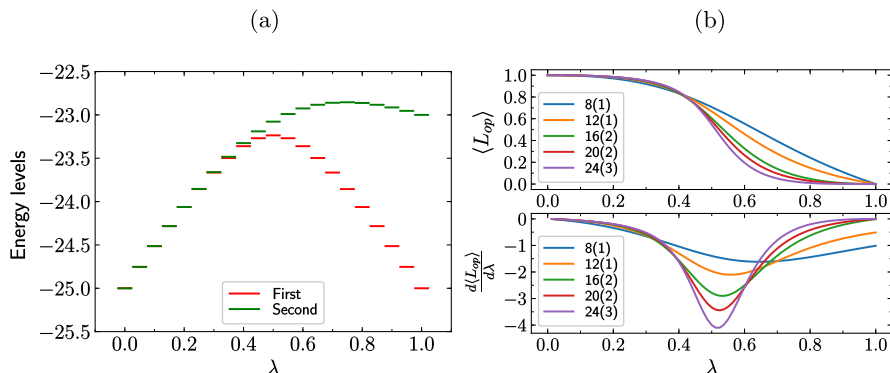


Figure 4.6: (a) Low energy spectrum of the interpolating Hamiltonian $H_{rm}(\lambda)$ for a system size of $N = 20$ spins. (b) (Top) Expectation value of the longest open-loop operator with respect to the interpolation strength, λ . (Bottom) Derivative of the expectation value of the open-loop operator with respect to λ . The labels denote the different system sizes with the value in the parantheses as defined above in Fig. 4.4.

Expectation value of the open loop operator

As in the earlier case, we compute the expectation value of the longest open loop operator to capture the critical interpolation strength, λ_c . We consider the loop operator, a sequence of σ_z connecting two different vertices on the right boundary as in Fig. 4.5(c). In the limit of $\lambda = 0$, the loop operator leaves the ground state invariant as the A_v excitations condense on the boundary while in the limit of $\lambda = 1$, due to the change in the boundary conditions, the A_v excitations are retained at the boundary (non-condensing) projecting it to an excited state. Therefore, in the limit of $\lambda = 0$, the expectation value is

4.3 $\tilde{G}_{\lambda=0} = \tilde{G}_{\lambda=1}$

1 while in the other limit of $\lambda = 1$, the expectation value is 0. We observe the expected behavior as in Fig. 4.6(b) and by performing finite size analysis we note the expectation value diverges at a critical strength of $\lambda_c = 0.48(4)$.

To conclude this section, we have analyzed TPTs induced by change in the boundary conditions realized by changing the underlying topology as well as the boundary conditions on the cylinder. Both of the phase transitions are characterized by change in ground state degeneracy with the energy gap, ΔE opening providing an estimate on the critical interpolation strength, λ_c . While topological entanglement entropy confirms that at all interpolation strength, λ , the phases are topologically ordered it is ineffective in detecting the distinct topological phases. To detect the criticality, we therefore, introduce the open loop operators whose expectation values captures the phase transition providing an estimate on the critical interpolation strength, λ_c .

4.3 $\tilde{G}_{\lambda=0} = \tilde{G}_{\lambda=1}$

As introduced earlier, quantum phase transitions are characterized either by change in the ground state degeneracy or the closing of the gap between the ground state (non-degenerate) manifold and the first excited state. In the previous section, we analyzed TPTs of the former kind while in this section, we introduce and analyze various scenarios of the latter kind. The phase transitions are induced by varying the boundary conditions which include topology variation and boundary variation with the ground state degeneracy remaining constant at either end of the interpolation in both of the above variations.

4.3.1 **Topology variation: Torus with domain wall to a cylinder with rough boundaries**

Domain walls are boundaries of the folded toric code $D(Z_2 \times Z_2)$ i.e., the boundary is characterized by the subgroup, $D(Z_2 \times Z_2)$, along with a non-trivial 2-cocycle of the same, as introduced in the earlier chapter. The folded toric code with the above boundary conditions when unfolded results in the scenario as illustrated in Fig. 4.7(a). The resulting Hamiltonian with the domain wall is given by $H_{dr}(0)$, where the B_p^\diamond is given by Fig. 4.7(d). We interpolate between toric code Hamiltonian with a domain wall to a cylinder with rough boundaries at both ends. The interpolating Hamiltonian is given by Eq. 4.5,

$$\begin{aligned}
 H_{dr}(\lambda) = & - \sum_v A_v^\blacklozenge - \sum_p B_p^\blacklozenge \\
 & - (1 - \lambda) \sum_{p'} B_p^\blacklozenge \\
 & - \lambda \sum_{p''} B_p^\blacktriangleleft - \lambda \sum_{p''} B_p^\blacktriangleright,
 \end{aligned} \tag{4.5}$$

where A_v^\blacklozenge , B_p^\blacklozenge , B_p^\blacktriangleright are as defined in the earlier section, while B_p^\blacktriangleleft is qualitatively identical to B_p^\blacktriangleright . The phase transition is accompanied by break in both, parity and anyonic symmetry. In the limit of $\lambda = 1$, $B_p(m)$ violations appear in pairs while in the limit of $\lambda = 0$, it is possible to draw single $B_p(m)$ violations from the domain wall with the other end of the open loop operator being identified as $A_v(e)$ violation across the domain wall, therefore in the limit of $\lambda = 1$, the parity symmetry with respect to the $B_p(m)$ violations is preserved while in the other extremum the symmetry is broken. The anyonic exchange symmetry is preserved in the limit of $\lambda = 0$, while in the limit of $\lambda = 1$, the symmetry is broken due to the (non)-condensation of the (B_p) , A_v violations.

Low energy spectrum

We analyze the low energy spectrum to gain an understanding on the criticality of the phase transition. In the limit of $\lambda = 0$, the ground state can be represented by $\mathcal{N} \prod_v (\mathbb{1} + A_v) \prod_p (\mathbb{1} + B_p^\blacklozenge) |\mathbf{0}\rangle$ where as in the limit of $\lambda = 1$ can be represented by $\mathcal{N} \prod_v (\mathbb{1} + A_v) |\mathbf{0}\rangle$. The ground state degeneracy in both the limits is two, in the limit of $\lambda = 0$ the non-trivial loop operator running parallel to the domain wall projects the above state into an orthogonal ground state. Any non-trivial loop operator running perpendicular to the domain wall, eventually passes through the domain wall does not generate any states which contribute to the ground state manifold as the ends of such open loops are identified with different type of excitations (a fermion), thereby the ground state degeneracy is two in the limit of $\lambda = 0$. From Fig. 4.8(a), for a system size of $N = 20$ spins, we notice that the ground state manifold is two fold degenerate in the extreme limits of λ , while at intermediate λ , around $\lambda \approx 0.5$, we observe the following:

1. A gap opening, ΔE , in the ground state manifold
2. The merging of the first and the second excited state

From Fig. 4.8(b), we notice that the gap opening is suppressed with increase in system size. Extrapolating to the thermodynamic limit, by performing finite size analysis, we note that the ground state manifold is two fold

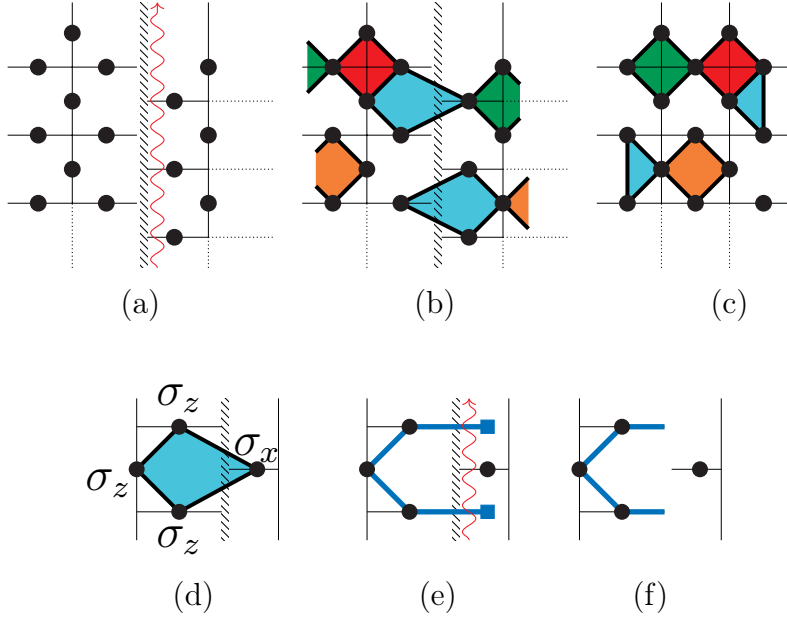


Figure 4.7: (a) The interpolation cut, denoted by the red snake dissects along the domain wall. (b) At $\lambda = 0$, TC on a torus with a domain wall, denoted by the short slant interface. (c) At $\lambda = 1$, TC on a cylinder with a rough boundary on both ends. (d) B_p^\diamond operator at the domain wall. (e) Open-loop operator with a pair of excitations projecting the ground state at $\lambda = 0$ into an excited state. (f) Open-loop operator whose excitations have condensed at the boundary leaving the ground state at $\lambda = 1$ invariant under the loop action.

degenerate at all strength, λ . The above conclusion, along with the merger of the first and second excited state at $\lambda \approx 0.5$ implies that there is a gap closing in the thermodynamic limit, possibly resulting in an energy spectrum as in Fig. 4.8(c). Therefore, the closing of the gap establishes the presence of a criticality, further confirming the notion that the two topological phases are distinct.

Expectation value of the open loop operator

In order to capture the critical interpolation strength, λ_c , we compute the expectation value of the longest open loop operator. We consider the open loop operator as in Fig. 4.7(e), (f) generated by the action of a sequence of σ_z operators. In the limit of $\lambda = 0$, the above loop operator projects the ground state into an excited state as the σ_z operator creates B_p excitations on

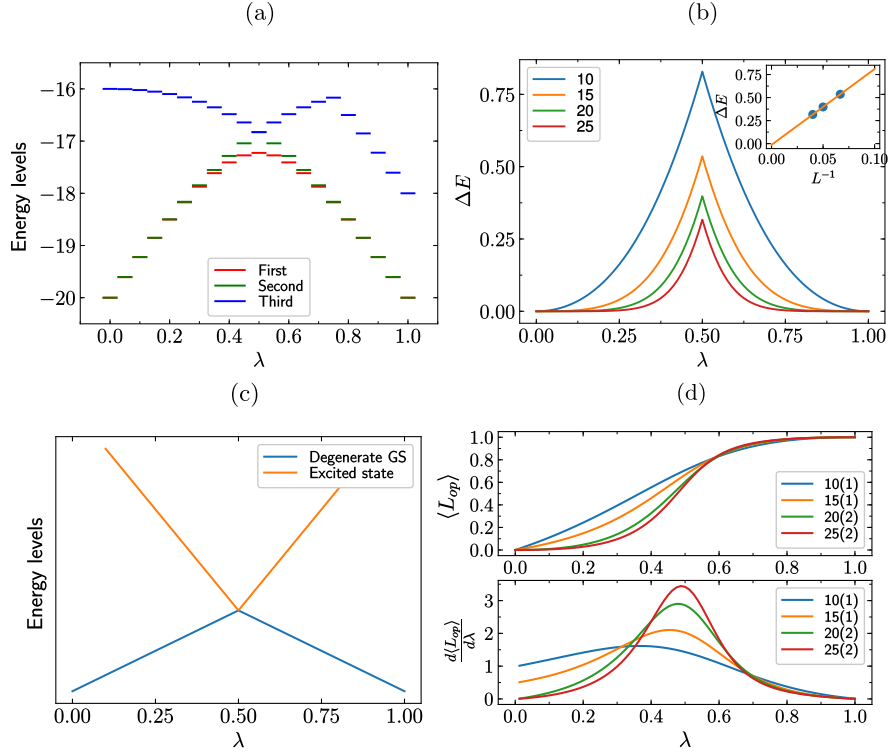


Figure 4.8: (a) The least energy levels for a system size of $N = 20$. At $\lambda = 0$ and $\lambda = 1$, we note that the ground state manifold is degenerate, while around $\lambda = 0.5$, we note the split in the degeneracy along with the merging of the first and second excited states. (b) Energy difference between the first two energy levels as a function of the interpolation strength, λ , with the labels denoting the different system sizes (Inset) Extrapolating the energy difference at $\lambda = 0.5$, to the thermodynamic limit by performing finite-size analysis. (c) Sketch of the energy spectrum in the thermodynamic limit as a function of the interpolation strength, λ . The gap closing between the degenerate ground state manifold and the first excited state indicates the presence of the phase transition. (d) (Top) Expectation value of the longest open-loop operator with respect to different interpolation strength, λ . (Bottom) Derivative of the expectation value with respect to λ . The labels denote the different system sizes with the value in the parentheses as defined earlier.

the other side of the domain wall, as in Fig. 4.7(e), thereby the expectation value of the loop operator is zero. While in the other limit of $\lambda = 1$, the string of σ_z operators create no new excitations in the system as the A_v violations generated condense on the boundary, leaving the ground state

invariant, thereby the expectation value of the loop operator is one. From Fig. 4.8(d) and by performing finite size scaling analysis, we note that the critical interpolation strength, $\lambda_c = 0.53(4)$.

4.3.2 Boundary variation: Cylinder with rough boundaries to smooth boundaries

We now consider the boundary variation of the above scenario, that is we fix the underlying topology to be a cylinder while varying both the open boundaries. We map the toric code on a cylinder with rough boundaries on either end to smooth boundaries on either end, as in Fig. 4.9(a), (b) with the interpolation Hamiltonian give by Eq. 4.6

$$\begin{aligned}
H_{rs}(\lambda) = & - \sum_{v \in I} A_v^\blacklozenge \\
& - (1 - \lambda) \sum_{p \in R} B_p^\blacklozenge - (1 - \lambda) \sum_{p \in L} B_p^\blacklozenge \\
& - (1 - \lambda) \sum_{\otimes \in R} |0\rangle\langle 0| - (1 - \lambda) \sum_{\otimes \in L} |0\rangle\langle 0| \\
& - \lambda \sum_{v \in R} A_v^\blacktriangleleft - \lambda \sum_{v \in L} A_v^\blacktriangleright \\
& - \lambda \sum_{p \in R} B_p^\blacklozenge - \lambda \sum_{p \in L} B_p^\blacklozenge,
\end{aligned} \tag{4.6}$$

where A_v^\blacklozenge , A_v^\blacktriangleleft , A_v^\blacktriangleright , B_p^\blacklozenge , B_p^\blacklozenge as defined earlier, with B_p^\blacklozenge as defined in Eq. 4.4, with I denoting the interior bulk region, R and L denoting the right and left boundary respectively. The phase transition is accompanied by the break in parity conservation, in the limit of $\lambda = 0$, the $B_p(A_v)$ violations appear in pairs (singly) while in the limit of $\lambda = 1$, the $B_p(A_v)$ violations appear singly (in pairs) due to the rough and smooth boundary conditions in the respective limits. Anyonic symmetry is absent in either of the phases due to the different condensation properties in either limits.

Low energy spectrum

The ground state degeneracy is same (equal to 2) in the extremal limits of $\lambda = 0$ and $\lambda = 1$. As in the topology variation scenario, we analyze the gap closing of the ground state manifold and the first excited state. From Fig. 4.10(a), it is evident that the first excited state and second excited state merge at $\lambda \approx 0.5$ for a system size of $N = 20$ spins. The gap between the ground state manifold and the first excited state is qualitatively similar to the topology variation case, as in Fig. 4.8(b). Therefore, the conjugation of

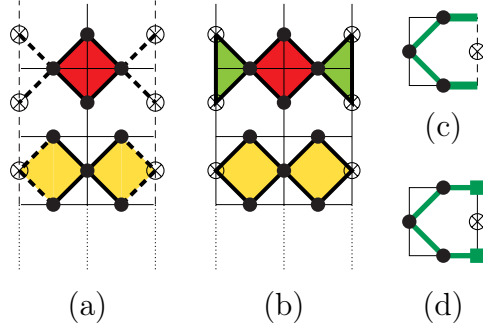


Figure 4.9: TC on a cylinder with (a) rough boundary, (b) smooth boundary on both ends. The red diamond belongs to the interior region, I , which remains unperturbed while the transparent half diamonds in (a) translate to half filled green diamonds A_v^{\blacktriangleleft} , $A_v^{\blacktriangleright}$ at either boundaries L and R respectively as λ varies from 0 to 1. Similarly, the golden yellow diamonds represent B_p^{\diamond} in (a) and map to B_p^{\blacklozenge} in (b) with increase in λ . The action of the open-loop operator at the boundary at (c) $\lambda = 0$, (d) $\lambda = 1$.

the merger between the excited states with the suppressed energy gap with increase in system size, results in a thermodynamic spectrum as in Fig. 4.8(c), thereby confirming the presence of criticality due to the closing of the gap.

Expectation value of the open loop operator

As in the other cases, we compute the expectation value of the longest open loop operator. We construct the open loop operator by a sequence of σ_z connecting the rough boundary at two distinct points, as in Fig. 4.9(c), (d). In the limit of $\lambda = 0$, the A_v violations condense on the boundary leaving the ground state invariant, therefore the expectation value is 1. While in the limit of $\lambda = 1$, the A_v violations do not condense on the boundary, therefore the loop operator projects the ground state into an excited state, thereby the expectation value is 0. From Fig. 4.10(b), we observe the above behavior, from the divergence of the expectation value of the loop operator and by performing finite size analysis we predict the phase transition occurs at $\lambda_c = 0.46(3)$.

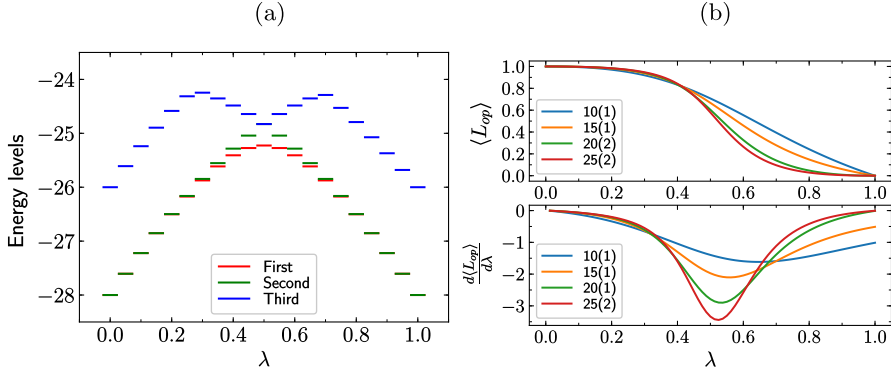


Figure 4.10: (a) Least energy levels for a system size of $N = 20$ spins. Both at $\lambda = 0$ and $\lambda = 1$, the ground state manifold is degenerate. At $\lambda = 0.5$, we note the merging of the first and the second excited energy levels. (b) (Top) Expectation value of the longest open-loop operator with respect to λ . (Bottom) Derivative of the expectation value with respect to λ . As noted earlier, the labels denote the different system sizes.

4.4 Additional Remarks

In this section, we introduce other possible scenarios of boundary variations which induce a topological phase transition. In the previous sections, we introduced the notion that to encode a topological phase transition it is sufficient that either one of the parity conservation or anyonic symmetry is broken but it is not necessary that every phase transition is accompanied by a broken symmetry. We aim to gain further insight into the above statement and make it more complete by introducing additional constraints. To this extent, we discuss the case of interpolation obtained by swapping the mixed boundaries on either side. Additionally, we also discuss TTPTs induced by topology variation with the domain wall being intact and also the scenario which involves simultaneous dissection and gluing of the underlying lattice.

4.4.1 Boundary variation: Interpolating between mixed boundaries on either end

In this section, we discuss the case of swapping the mixed boundaries on either sides by interpolation i.e., mapping identity (group) as boundary, $\lambda = 0$, to group (identity) as boundary on the left (right) boundary, $\lambda = 1$, as in Fig.4.11(a), (b). The TTPT is characterized by the gap closing at $\lambda = 0.5$,

belonging to the $\tilde{G}_{\lambda=0} = \tilde{G}_{\lambda=1}$ class. In the limit of $\lambda = 0$ and $\lambda = 1$, both A_v and B_p violations can be drawn singly from either of the boundaries leaving the parity conservation broken. The anyonic exchange symmetry also remains broken in both the limits due to the different condensation properties at either of the boundaries. From the above discussion, it is not necessary that every topological transition is accompanied by a broken symmetry. However, we can further refine the parity symmetry where we include the physical boundary which retains/breaks the parity, thereby completing the necessary condition. That is, in the limit of $\lambda = 0$, the parity of the $A_v(B_p)$ violations is conserved with respect to the right (left) boundary while in the limit of $\lambda = 1$, the parity conservation is broken due to the change in the boundary conditions. Therefore, specifying the particular physical boundary results in the following bi-implication:

Either a break in the parity with respect to a particular physical boundary or break in the anyonic symmetry is necessary and sufficient to characterize the presence of a TTPT.

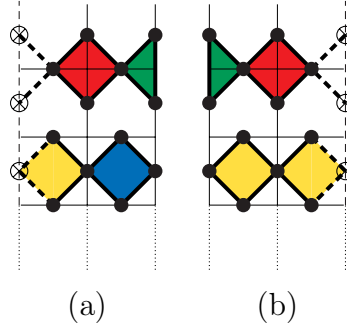


Figure 4.11: Toric Code on a cylinder with mixed boundary conditions (a) rough boundary on the left and smooth boundary on the right (b) smooth boundary on the left and rough boundary on the right.

4.4.2 Topology variation: Transition with the domain wall intact

Previously, we considered the interpolation between the toric code on a torus with a domain wall to a toric code on a cylinder with rough boundaries achieved by dissecting along the domain wall. In this section, we analyze a similar case, instead of dissecting the torus along the domain wall we consider the case of dissection along a different rail thereby mapping the torus with a

4.4 Additional Remarks

domain wall ($\lambda = 0$), as in Fig. 4.12(a) to a cylinder with mixed boundaries and a domain wall ($\lambda = 1$), as in Fig. 4.12(b).

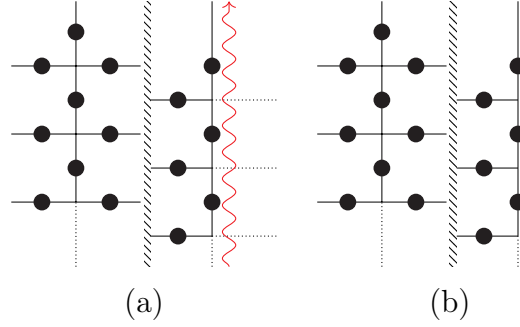


Figure 4.12: (a) Toric Code on a torus with a domain wall. The red snake represents the interpolation cut which breaks the periodicity along some other rail other than the domain wall leading to (b) Toric code on a cylinder with mixed boundaries on either end with the domain wall intact.

The phase transition is characterized by the change in the ground state degeneracy at either ends of the interpolation, as in the limit of $\lambda = 0$, the ground state degeneracy is two while in the other limit it is four. With the introduction of the domain wall the ground state manifold jumps to four, with the four ground states being generated by the action of the following non-trivial loop operators on the trivial ground state, given by the product representation as in the earlier sections:

1. The non-trivial loop operator encircling the cylinder
2. The non-trivial loop operator connecting the physical boundaries, the A_v violation condensing on the left boundary map to a B_p violation as it crosses the domain wall which condenses on the right boundary
3. A combination of the above two loop operators
4. Absence of a non-trivial loop operator (or one of the above two non-trivial loop operators acting twice)

The phase transition falls into the category of $\tilde{G}_{\lambda=0} \neq \tilde{G}_{\lambda=1}$. It is also worth noting that in the current scenario the phase transition is accompanied solely by breaking the anyonic symmetry while parity conservation remains broken in both the phases. In the limit of $\lambda = 0$, the anyonic symmetry is preserved due to the presence of the domain wall as discussed earlier, and in the limit

of $\lambda = 1$, this is broken due to the introduction of the boundaries. Also, it is always possible to create single A_p , B_p violations due to the domain wall in the limits of $\lambda = 0$ and due to the boundaries in the limits of $\lambda = 1$ leaving the parity conservation broken on either side of the transition.

4.4.3 Topology variation: Transition arising out of simultaneous dissection and gluing

In all of the above scenarios, the phase transitions arising out of the topology variation involved dissection or gluing (the case where the interpolation limits are inverted). In this section, we introduce a scenario which involves simultaneous dissection and gluing of the underlying topology. To this extent, we interpolate between toric code on a cylinder with mixed boundaries and a domain wall ($\lambda = 0$) to a cylinder with rough boundaries and no domain wall ($\lambda = 1$). In the limit of $\lambda = 0$, we dissect along the domain while gluing the mixed boundaries, as in Fig. 4.13(a), mapping to a cylinder with rough boundaries, in the limit of $\lambda = 1$, as in Fig. 4.13(b).

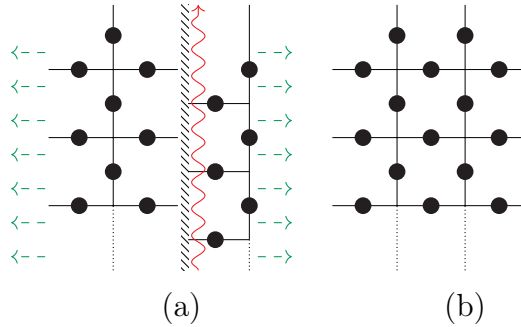


Figure 4.13: Interpolating via simultaneous dissection and gluing, the red snake represents the dissection while the dashed green arrows represent the gluing action. (a) Toric Code on a cylinder with mixed boundaries and a domain wall (b) Toric Code on cylinder with rough boundaries on either end.

The transition is characterized by change in the ground state degeneracy as in the limit of $\lambda = 0$, the ground state degeneracy is four, while in the limit of $\lambda = 1$, the ground state manifold is two fold degenerate. We also note that the phase transition is accompanied by the break in the parity conservation as in the limit of $\lambda = 0$, the B_p violations appear singly while in the other extremum they appear in pairs. The anyonic symmetry is broken in both phases due to the different condensation properties at the boundary.

Part III

Robustness of intrinsic topological order in open systems

Chapter 5

Topological to topological phase transitions in an open quantum system

In this chapter, we extend the analysis of the TTPT's of the previous chapter to an open quantum system. We begin by reviewing some of the key notions behind open quantum systems which are described by the Lindblad master equation involving collapse operators which interact with the environment. We then introduce the notion of a phase transition between two different topological phases obtained by engineering suitable dissipative collapse operators. To draw parallels with the closed setup, the effective cooling rate associated with the dissipative collapse operators map to the interpolation strength, with the steady states at the extremities of interpolation getting mapped to the respective ground states of the closed system. While in the closed setup the phase transition was a property of the ground states parameterized by the interpolation strength, in the current open scenario, the topological phase transition is a property of the steady state [76, 77, 78, 79, 80, 81, 82] parameterized by effective cooling rate of the dissipators facilitating the effective change in boundary conditions. As in the closed setup analysis, we analyze the behavior of the expectation value of the open loop operator as a function of the effective dissipative rate to capture the criticality.

5.1 Open quantum systems - A review of key concepts

In this section, we briefly review the Lindblad master equation which governs the dynamics of open quantum systems. We note that the following discussion is based on the Ref. [83] and for a more elaborate discussion we refer the reader to Ref. [84].

It is known that the dynamics of closed system described by the Hamiltonian, H_S , is governed by the Schrödinger equation given by

$$i\hbar \frac{d}{dt} |\psi(t)\rangle = H_S |\psi(t)\rangle \quad (5.1)$$

In a more realistic setting, for example in the case of experimental setups, the interaction (I) with environment (E) is almost inevitable. The total Hamiltonian, H_t which describes the entire setup is given by

$$H_T = H_S + H_I + H_E \quad (5.2)$$

The state vector in this formalism is now represented as a statistical ensemble of pure states, known as density matrices, ρ , which are given by

$$\rho = \sum_i p_i |\psi_i\rangle \langle \psi_i| \quad (5.3)$$

where p_i represents the probability of observing ρ in the state $|\psi_i\rangle$. The dynamics of the system described by H_T is governed by the von Neumann equation given by

$$i\hbar \frac{d}{dt} \rho = [H_T, \rho] \quad (5.4)$$

which results in the unitary evolution of the entire system and the environment given by

$$\rho(t) = U_{SE} \rho(0) U_{SE}^\dagger \quad (5.5)$$

As we are interested in the dynamics of the system alone, we perform a partial trace over the environment degrees of freedom. We further assume that the system (S) and environment (E) are separable, that is we assume that the initial state of the system and the environment are completely uncorrelated which results in the following

$$\rho_S(t) = \text{Tr}_E(U_{SE}(\rho_S(0) \otimes \rho_E(0))U_{SE}^\dagger) \quad (5.6)$$

Using the formalism of dynamical maps, say \mathcal{V} , which map the $\rho_S(0)$ onto other density matrices involving only the system, in addition, to performing

5.2 Interpolation via engineered dissipation

the spectral decomposition of the density matrix of the environment, results in the Kraus sum representation of the density operator $\rho_S(t)$, given by

$$\rho_S(t) = \mathcal{V}(\rho_S(t)) = \sum_k M_k \rho_S(0) M_k^\dagger \quad (5.7)$$

where M_k are the Kraus operators given by $M_k^{i,j} = \langle i, k | U_{SE} | j, 0 \rangle$, with $\{|k\rangle\}$ being an orthonormal basis for H_E , which satisfy the criteria $\sum_k M_k M_k^\dagger = \mathbf{1}$, due to U_{SE} being a unitary. The Kraus operators preserve the positivity, unit trace and Hermitian properties of the density matrices.

Motivated by the differential equation for coherent evolution (Schrödinger equation for closed systems), we now proceed to discuss if a similar equation can be derived for the system dynamics involving the environment which promotes decoherence. In other words, we aim to arrive at $\rho_S(t + \delta t)$ which does not necessarily only depend on $\rho_S(t)$ as information dissipated into the environment can flow back into the system at later times. If the above back flow of information is restricted, implying the density matrix at $\rho_S(t + \delta t)$ is solely dependent on $\rho_S(t)$ (in other words the environment is memoryless) then in this approximation it is possible to arrive at a master equation which describes the dynamics of the system which includes decoherence. We note that such an approximation is referred to as Markov approximation. In the Markovian approximation, the Kraus sum which captures the non-unitary evolution of the system can be written as $\rho(t + \delta t) = \sum_k M_k(\delta t) \rho(t) M_k^\dagger(\delta t)$, which results in the Lindblad master equation given by

$$\dot{\rho}_S = -\frac{i}{\hbar} [H_S, \rho_S] + \sum_n C_n \rho_S(t) C_n^\dagger - \frac{1}{2} [\rho_S(t) C_n^\dagger C_n + C_n^\dagger C_n \rho_S(t)] \quad (5.8)$$

where C_n are the dissipative operators that capture the interaction of the system with the environment. We note that in the long time limit ($t \rightarrow \infty$), the system stabilizes giving rise to steady states, that is $\dot{\rho}_S = 0$. The properties associated with these steady states characterize different phases, with the divergence in these properties signaling the presence of a criticality or a phase transition in an open quantum system.

5.2 Interpolation via engineered dissipation

In this section, we aim to interpolate between the two steady states given by the ground state of toric code on a torus ($\lambda = 0$) and on a cylinder ($\lambda = 1$). To facilitate the interpolation, we introduce collapse operators as in Eq. 5.9 which are parameterized by the cooling rate, λ . We analyze the steady states,

$\rho(\lambda)$ at different cooling rates, λ , obtained by solving the Lindblad master equation in a purely dissipative setup ($H = 0$). For clarity, we split the collapse operators into three classes:

- (a) Collapse operators acting on the permanent vertices (faces) given by $c_{v(f)}^p$
- (b) Collapse operators acting on the periodic boundary given by $c_{v(f)}^t$
- (c) Collapse operators acting on the open boundary given by $c_{v(f)}^o$

and define them as in Eq. 5.9, Fig. 5.1

$$\begin{aligned}
 c_v^p &= \frac{\sqrt{\gamma_v}}{2} \sigma_z^{(i)} (\mathbb{1} - A_v^\blacklozenge), \\
 c_f^p &= \frac{\sqrt{\gamma_f}}{2} \sigma_x^{(j)} (\mathbb{1} - B_f^\blacklozenge), \\
 c_v^t(\lambda) &= \frac{\sqrt{\gamma_v}}{2} (1 - \lambda) \sigma_z^{(i)} (\mathbb{1} - A_v^\blacklozenge), \\
 c_f^t(\lambda) &= \frac{\sqrt{\gamma_f}}{2} (1 - \lambda) \sigma_x^{(j)} (\mathbb{1} - B_f^\blacklozenge), \\
 c_v^o(\lambda) &= \frac{\sqrt{\gamma_v}}{2} \lambda \sigma_z^{(i)} (\mathbb{1} - A_v^\blacktriangleright), \\
 c_f^o(\lambda) &= \frac{\sqrt{\gamma_f}}{2} \lambda \sigma_x^{(j)} (\mathbb{1} - B_f^\blacktriangleleft),
 \end{aligned} \tag{5.9}$$

where γ_v, γ_f are the cooling rates of the vertex and face excitations, while λ is the interpolation strength, $A_v^\blacklozenge, B_f^\blacklozenge, A_v^\blacktriangleright, B_f^\blacktriangleleft$ operators are as defined in the earlier sections.

Intuitively, in the vicinity of $\lambda = 0$ the collapse operators diffuse the excitations around the lattice, the excitations perform a random walk until they fuse with an excitation of the same type, i.e., the collapse operators impose the fusion rules cooling the product state to the entangled ground state of the toric code on a torus. In the other limit of $\lambda = 1$, due to the open boundaries conditions, appropriate collapse operators promote the condensation of the relevant excitations at a given boundary while allowing the diffusion of excitations in the bulk. Due to the different cooling properties because of the open boundary, the cooled steady state is equivalent to the ground state of the toric code on a cylinder with mixed boundaries. At intermediate λ , the dynamics is captured by the competition between the cooling operators that promote the diffusion of the excitations along the periodic boundary and the cooling operators which promote a biased diffusion resulting in a restricted diffusion, effectively capturing the break in topology.

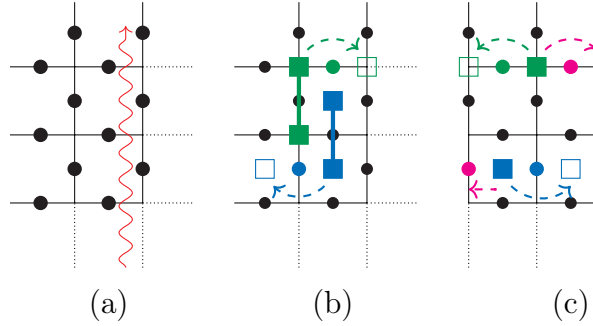


Figure 5.1: (a) The red snake represents the interpolation cut. The dissipative dynamics induced by the collapse operators by diffusing excitations on (b) a torus (c) a cylinder with mixed boundaries. (b) Excitations always appear in pairs and the collapse operators diffuse the excitations (represented by dashed green and blue arrows) or cool them by fusing (represented by thick green and blue lines). (c) Excitation parity is not conserved because of the boundary, thereby allowing the excitations to condense at the boundary (represented by dashed magenta arrows), in addition to the diffusion and pair cooling as noted in (b).

To detect the phase transition between the two topological phases we compute the expectation value of the longest loop operator with respect to the steady states, $\rho(\lambda)$, parameterized by the cooling rate, λ , which controls the interpolation. The steady states at a given λ are computed by the MCWF method [85]. The longest open loop operator, L , we consider in the current scenario is given by a sequence of $\sigma_{z(x)}$ operators which sport A_v (B_p) violations at it ends. In the vicinity of $\lambda = 0$ the loop operator projects the ground state into an excited state and hence the expectation value is zero, that is the $\text{Tr}(\rho_\lambda L) = 0$, while in the limit of $\lambda = 1$, the excitations condense on the boundary with the expectation value going to one. We compute the critical cooling rate, $\lambda_c = 0.637(4)$, by performing finite size analysis as in Fig. 5.2(a).

5.3 Dissipative interpolation via imperfect cooling

The general form of the collapse operators considered in the previous section is given by $\gamma C(1 - D)$, where the D operator probes the presence of an excitation and C diffuses the excitation with γ being the cooling rate. In

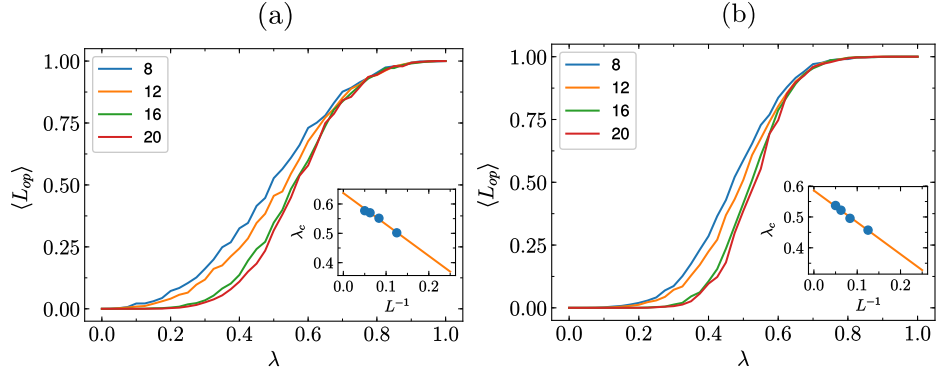


Figure 5.2: Expectation value of the longest open-loop operator parameterized by the cooling rate, λ , (with $\gamma_v = \gamma_f = 1$), and the labels denoting the different system sizes for (a) perfect cooling (b) imperfect cooling. (Inset) Finite size scaling to obtain the critical cooling rate, λ_c .

this section, we introduce collapse operators of the form $\gamma C(\mathbb{1} - \gamma D)$, as in Eq. 5.10. In the presence of excitations, in the former, the action of the check operator does not introduce any additional scaling but in the latter the check operator introduces additional scaling which further facilitates the cooling rate. In the absence of excitations, in the former, the collapse operators leave the state invariant, while in the latter the collapse operators induce additional excitations leading to a noisy setup.

$$\begin{aligned}
 c_v^t(\lambda) &= \frac{\sqrt{\gamma_v}}{2}(1-\lambda)\sigma_z^{(i)}(\mathbb{1} - (1-\lambda)A_v^\blacklozenge), \\
 c_f^t(\lambda) &= \frac{\sqrt{\gamma_f}}{2}(1-\lambda)\sigma_x^{(j)}(\mathbb{1} - (1-\lambda)B_f^\blacklozenge), \\
 c_v^o(\lambda) &= \frac{\sqrt{\gamma_v}}{2}\lambda\sigma_z^{(i)}(\mathbb{1} - \lambda A_v^\blacktriangleright), \\
 c_f^o(\lambda) &= \frac{\sqrt{\gamma_f}}{2}\lambda\sigma_x^{(j)}(\mathbb{1} - \lambda B_f^\blacktriangleleft),
 \end{aligned} \tag{5.10}$$

We compute the steady states, $\rho(\lambda)$, parameterized by the cooling rate, λ , using the MCWF method. As established in the earlier scenario, we compute the expectation value of the longest open loop operator with respect to the above steady states. As above, in the vicinity of $\lambda = 0$, the expectation value is zero while in the limit of $\lambda = 1$, the expectation value is one. We compute the critical cooling rate, $\lambda_c = 0.586(1)$, by performing finite size analysis as in Fig. 5.2(b). We note that the critical cooling rate is lowered compared to the above case implying the cooling is effective in the current scenario in

5.3 Dissipative interpolation via imperfect cooling

comparison to the previous case.

To conclude, we have introduced TTPT's in an open quantum system by appropriately tailoring the collapse operators which cool to different toric code ground states depending on the rate of cooling. As in the previous chapter, the expectation value of the open loop operator effectively captures the TTPT. We note that the open loop operators are effective in the current scenario due to the fact that the bulk excitations are excluded by the open loop operator, as we consider a quasi-1D geometry. In a more general context, for example a more general perturbation, the bulk excitations might vary the expectation value of the open loop leaving the notion of open loop operator to detect topological phases ambiguous. In addition, the construction of open loop operators is limited to scenarios which support open boundaries, as the definition of the open loops require the notion of anyon condensation which is absent in the case of periodic boundaries. Therefore, due to the above limitations and also to uniformly quantify topological order across varied scenarios, in the following chapter we introduce an operational definition of topological order.

Chapter 6

An operational definition of topological order

In the previous part, we have studied various scenarios which host topological phases and have analyzed the order using a variety of signatures. TEE was an effective probe in detecting quantum phase transitions while it remained ineffective in identifying different topological phases. In a more general context, the equivalence between TEE, SPT order and intrinsic topological order still remains ambiguous. For example, the ground state of the Kitaev ladder, as in Fig. 6.1, which exhibits SPT order has no TEE [86]. In addition, TEE does not always capture the distinction between symmetry protected topological order and intrinsic topological order. One such example is the construction by Bravyi in Ref. [87]: Consider a 1D zigzag chain as in Fig. 6.1 with qubits on each vertex of the chain interacting via the Hamiltonian

$$H = - \sum_k \sigma_{k-1}^z \sigma_k^x \sigma_{k+1}^z \quad (6.1)$$

We consider the ground state of the above zigzag Hamiltonian, also known as a cluster state and compute the TEE by considering a cut as in Fig. 6.1 such that it includes half of the chain by following the Kitaev-Preskill prescription as introduced in Chap. 1. The TEE remains $\log 2$ yet the ground state is topologically trivial as it can be prepared from a product state using Controlled-Z (CZ) gates defined by

$$CZ|k_1, k_2\rangle = \begin{cases} -|k_1, k_2\rangle & \text{for } k_1 = k_2 = 1 \\ |k_1, k_2\rangle & \text{otherwise} \end{cases} \quad (6.2)$$

(finite depth unitaries). In addition, in Ref. [88] it was observed that topologically trivial states in 3D exhibit non-zero TEE. Also, the extraction of

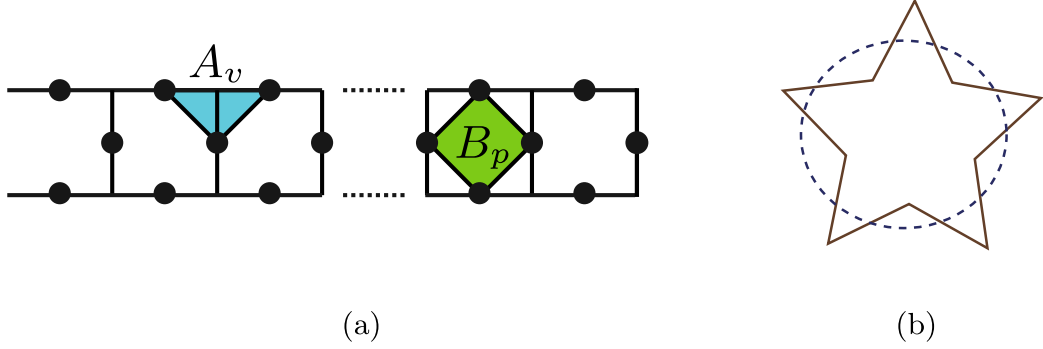


Figure 6.1: (a) Kitaev 1D ladder defined by the toric code A_v , B_p operators defined on a quasi-1D ladder with periodic boundaries. (b) Consider qubits at the vertices of the zigzag chain. The dashed line represents the region used to compute the entropy which is further divided into three regions to extract TEE via the Kitaev-Preskill prescription.

TEE as described in Chap. 3, in few scenarios, have additional nontopological contributions due to symmetry protected states arising at the choice of the cut [89, 90, 91]. In Ref. [11], the following definition based on circuit depth was proposed i.e., a state is *intrinsic* topologically ordered state, if it cannot be mapped to a product state using local unitaries of finite depth [11]. Though the above definition provides a qualitative insight it is difficult to quantify as it is quantum Kolmogorov complex, which is uncomputable [92]. Modular matrices as a probe have been successful in the context of periodic boundaries [15, 18], while in the open boundary scenario due to anyon condensation numerical recipes for their construction remain unclear. In addition, the notion of mixed topologically ordered states remains unclear. Though there have been several proposals in this direction [93, 94, 95, 96, 97, 98], due to the absence of paradigmatic models hosting such states, the understanding and verification of the above still remains an open challenge. In an attempt to remove the above limitations, we introduce an operational definition to quantify topological order in this chapter. We not only validate the new method by mapping to well established models but also introduce novel scenarios which host topological phases in an open quantum system.

We begin by introducing the perturbed toric code model on a minimal lattice which hosts a quantum phase transition. We then present a general outline of the operational definition, which we validate by accurately detecting the quantum criticality introduced in the above perturbed toric

code model. We then introduce various nonequilibrium transitions, and by engineering suitable collapse operators which encode the rules of the above transitions, we discover mixed states that are topologically ordered.

6.1 Perturbed Toric Code on a minimal lattice

We introduce the toric code Hamiltonian on a minimal lattice as in Fig. 6.2(a). The Hamiltonian consists of three body vertex (face) A_v (B_p) operators, with two body face operators at either ends of the quasi-1D geometry and is given by

$$H_{tc} = - \sum_v A_v - \sum_p B_p - \sum_{p'} B_{p'} \quad (6.3)$$

where $A_v = \prod_{i=1}^3 \sigma_x^{(i)}$, $B_p = \prod_{j=1}^3 \sigma_z^{(j)}$, $B_{p'} = \prod_{k=1}^2 \sigma_z^{(k)}$. The ground state is non-degenerate and as introduced previously, is given by $\mathcal{N} \prod_v (1 + A_v) |\mathbf{0}\rangle$.

We consider the Hamiltonian, as in Eq. 6.3 in the presence of a perturbation, $\sum_k \sigma_x^{(k)}$ applied on the second rail, as in Fig. 6.2(a), leading to Eq. 6.4

$$H_p = H_{tc} - h_x \sum_k \sigma_x^{(k)} \quad (6.4)$$

The perturbation creates B_p violations in pairs as in Fig. 6.2(c). Unlike the previous scenarios, where perturbation on open boundaries led to single excitations, here the perturbation is always contained in the bulk leading to paired excitations with no possibility for single excitations.

6.1.1 Topological Signatures

The perturbation induces strings with excitations at either ends. At low h_x , the system is topologically ordered as the excitations are deconfined, while at high h_x the excitations are confined, hence capturing a topological phase transition. As in the previous section, we compute topological entanglement entropy and expectation value of a non-local open loop operator to further confirm the presence of a criticality.

Topological Entanglement Entropy

We compute the sub-leading constant term using the earlier established method by considering the cut as in Fig. 6.2(b). From Fig. 6.3(a) we note that for $h_x = 0$, the sub-leading constant is $\log 2$ that is the ground state is

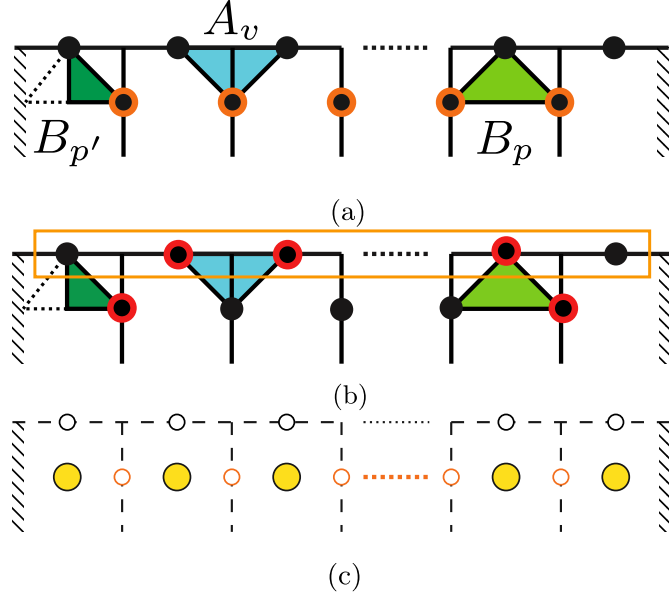


Figure 6.2: (a) Toric Code on a minimal lattice with smooth (rough) boundaries on the top (bottom) and truncated open boundary at either end. The A_v (B_p) operators in the bulk are three body operators and are denoted by light green (blue) triangles. Due to the truncated boundary conditions the interaction at either end is given by $B_{p'}$, denoted by dark green half triangles. The spins on the perturbed rail are highlighted by bold orange outline. (b) The region encompassed by the orange box is used in the computation of entropy. The spins highlighted by bold red outline are used to construct the open loop operator with A_v excitations condensing on the rough lower smooth boundary. (c) The perturbed of the minimal instance maps to the 1D Ising model with the B_p excitations being mapped to the Ising spins.

topologically ordered and as the perturbation strength is increased we notice strong deviations from $\log 2$ confirming the presence of the transition point.

Loop operator expectation value

We construct the open loop operator, obtained by the action of σ_z operator on a sequence of spins as in Fig. 6.2(b). The σ_z operators create A_v violations and these can be condensed at the rough open boundaries on the bottom of the lattice, resulting in an open loop operator. From Fig. 6.3(b), we notice that in the limit of $h_x \rightarrow 0$, the expectation value of the longest open loop operator is 1 while at higher perturbation strength, h_x , there is a drop in the

6.2 Probing Topological Order via Error Correction Statistics

expectation value. The divergence of the expectation value, further confirms the presence of a transition point.

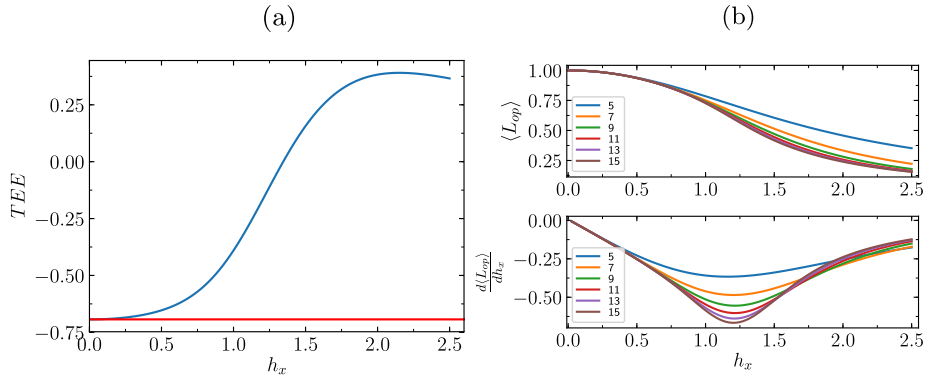


Figure 6.3: (a) Topological entanglement entropy (TEE) as a function of the perturbation strength, h_x , with the red line $y = -\log 2$ denoting the TEE at $h_x = 0$. (b) (Top) Expectation value of the longest open loop operator with respect to h_x . (Bottom) Derivative of the expectation value, with the divergence confirming the presence of criticality.

6.2 Probing Topological Order via Error Correction Statistics

In this section, we introduce a new method to detect the topological phase transition. We sketch a brief outline of the procedure and later apply this to the above introduced perturbed model.

We begin by considering the ground state, $|\psi_p\rangle$, of some perturbed Hamiltonian belonging to the class of toric code Hamiltonians at some perturbation strength, h . The method to detect the phase transition follows the prescription as below:

1. Express the perturbed ground state as a superposition of all the eigenstates of the unperturbed Hamiltonian

$$|\psi_p\rangle = \sum_k c_k |\psi_k\rangle \quad (6.5)$$

2. For each of the excited state $|\psi_k\rangle$, compute the time taken to annihilate all the excitations by using an error correction algorithm which is not necessarily optimal.

3. Consider the error correction circuit to be given by an operator C , then the time correction statistics is given by $\langle \psi_p | C | \psi_p \rangle$ (in other words, we generate the time correction statistics of the error correction by combining $|c_k|^2$ with the error correction time of each excited state).

Any statistical measure of the time statistics, for instance: mean, variance, standard deviation qualitatively captures the phase transition as all the above statistics encode the information on the error correction time, see Fig. 6.5, Appendix. C. That is, in the topologically ordered phase, the above quantities are bounded while in the trivial phase they diverge with increase in system size. Further, implying that a state is topologically ordered if it takes finite time (in system size) to correct its errors while a trivial state cannot correct its errors in finite time. We note that standard deviation has better finite size scaling behavior in comparison to the rest of the measures, see for instance Fig. 6.5 and thus we use the former to effectively capture the criticality. In addition, we also note that we impose no optimality constraints on the choice of the error correction algorithm, as the above measures qualitatively remain the same with respect to any error correction strategy, thereby effectively capturing the phase transition.

6.2.1 Mapping to the Ising 1D chain

We establish a relationship between the perturbed minimal lattice and Ising 1D chain with nearest neighbor interactions. The advantage of such an analysis is two fold, firstly to benchmark the proposed method by comparing the critical strength to that of the Ising 1D chain, secondly to gain access to higher system sizes for the purpose of numerical analysis.

To establish the relationship, we move from the physical spins to the excitation space. In the excitation space, the presence/absence of an excitation can be described by a Ising spin $\frac{1}{2}$. As introduced earlier, we note that the perturbation induces only B_p excitations in pairs while leaving the A_v sector invariant which translates to a nearest neighbor interaction in the excitation space as in Fig. 6.2(c). Therefore, the effective Hamiltonian in the excited space translates to the well known Ising 1D chain

$$H_{is} = -h_x \sum_{i,j} \mu_x^{(i)} \mu_x^{(j)} - \sum_i \mu_z^{(i)} \quad (6.6)$$

In the limit of $h_x \rightarrow 0$, the original model is topologically ordered which maps to the paramagnet of the Ising chain while at $h_x \rightarrow \infty$ the original model is topologically trivial which maps to the ferromagnet of the above Ising chain. It is well established that the quantum criticality of the Ising 1D

chain is at $h_c = 1$. Therefore, in the case of the above perturbed toric code model, the critical strength at which the topological phase transition occurs is given by $h_x = 1$, which can be used to benchmark our new method.

We note two interesting properties, one, the parity conserving symmetry in the above introduced perturbed toric code model, manifests itself as the Z_2 symmetry of the Ising chain. That is the B_p violations which always appear in pairs in the bulk due to the perturbation are not allowed to condense via the boundary which leads to the protection of the Z_2 -Ising symmetry in the excitation space. It is in this context, we note that the perturbed ground state is symmetry protected topologically ordered state as parity of excitations is preserved due to the restriction of anyon condensation. The other interesting observation we note is the entanglement pattern, as introduced in Chap. 1, in the ground state of the original perturbed model, H_p and the Ising mapped equivalent, H_{is} . In the limit of $h_x = 0$, the ground state of H_p is the ground state of the toric code, a highly entangled state, which maps to a product state in the excitation space, i.e., the ground state of H_{is} . In the other limit of $h_x \rightarrow \infty$, the ground state of H_p is a product state which maps to an entangled state in the excitation space. We shall invoke this map later to gain an intuitive understanding of the topological phase transitions in an open setting.

6.2.2 Detecting topological phase transition in the perturbed minimal instance toric code

Having established the equivalence map between the perturbed minimal instance toric code model and Ising 1D chain, we compute the error correction statistics with respect to Ising chain. It is important to note that though the equivalence exists, the unitary connecting both the ground states is highly non-local (as in the CNOT map introduced in Chap. 3) and thereby, these phases are distinct which is as expected (the paramagnet which gets mapped to the toric code ground state is not topologically ordered).

To verify the proposed method, we begin by considering the ground state, $|\psi_{tc}^h\rangle$ of the perturbed toric code Hamiltonian, as in Eq. 6.4 at some perturbation strength, h . We express the perturbed ground state as a superposition of all the eigenstates, $|\psi_{tc}^k\rangle$, of the unperturbed toric code Hamiltonian, the Ising equivalence of the above is captured by the following map

where $|\psi_{tc}^0\rangle$ is the ground state of the toric code, $L = \sigma_x$ being the operator acting on the above ground state generating relevant excited states of the toric code Hamiltonian i.e., excited states with even pairs of B_p violations. In the Ising spin basis, $|\psi_{is}^0\rangle$ corresponds to $|000\dots 0\rangle$, a paramagnet, while

$$\begin{aligned}
 |\psi_{tc}^h\rangle &= \alpha_0 |\psi_{tc}^0\rangle + \sum_i \alpha_i L_i |\psi_{tc}^0\rangle \\
 &\quad \downarrow \qquad \qquad \qquad \downarrow \\
 |\psi_{is}^h\rangle &= \beta_0 |\psi_{is}^0\rangle + \sum_{i,j} \beta_{ij} P_i P_j |\psi_{is}^0\rangle
 \end{aligned}$$

P_i, P_j 's are σ_x resulting in spin flips on the paramagnet corresponding to the even pairs of B_p violations.

We perform the error correction in the Ising spin basis by mapping every excited state to a paramagnet, i.e., $|000\dots 0\rangle$, which in the exact model maps to the ground state of the toric code model.

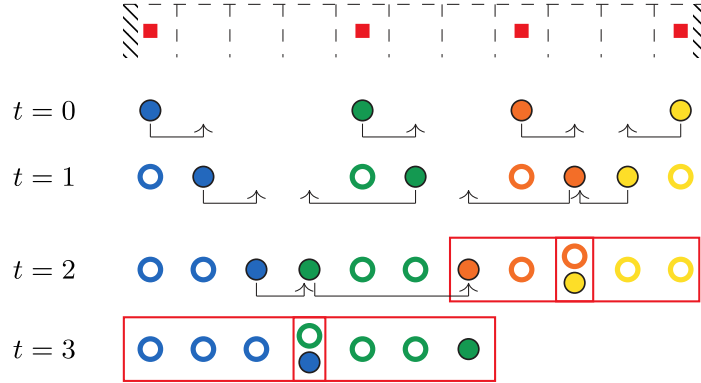


Figure 6.4: Error correction scheme for a 1D Ising chain. The red squares indicate the excitation positions (B_p violations) obtained after a measurement in the Ising basis. Each excitation is associated with a walker (identified by different colored circles) which hops right and left in the bulk, like the green and orange walkers, while the walkers at the boundary move in a single direction, like the blue and yellow walkers, as the the boundaries on either side are truncated. The walkers leave a mark on the site visited starting at $t = 0$, and span the lattice until they cross the path of the another walker, for example orange and yellow, blue and green walkers. The time taken for an excited state to be corrected to the paramagnet is given by the time taken for all walkers to annihilate, in this case it is 3. The annihilation of the violations refers to the fusing of B_p violations in the original toric model with the fusion resulting in the vacuum. In a more general setting, fusion rules form the basis of error correction, with the algorithm designed to fuse excitations to vacuum, thereby leading to the reference state.

6.2 Probing Topological Order via Error Correction Statistics

To perform the error correction, we employ the following scheme: we identify each excitation with a unique walker. Every walker parallelly keeps tracing the lattice until their paths cross, at which point the respective excitations annihilate instantaneously, as in Fig. 6.4. For small system sizes it is possible to compute the exact statistics by computing the time taken for all the excitations to annihilate for all excited states (see Appendix. C). In a more realistic setting, from an experimental viewpoint the statistics is generated by repeated measurements in the Ising basis, that is measurements in the excited basis. We compute the standard deviation (σ) of the above statistics as a function of the perturbation strength, h_x , as in Fig. 6.5 and note that the topological phase transition occurs at $h_x = 1.003(1)$ which is in agreement with the well known 1D Ising transition.

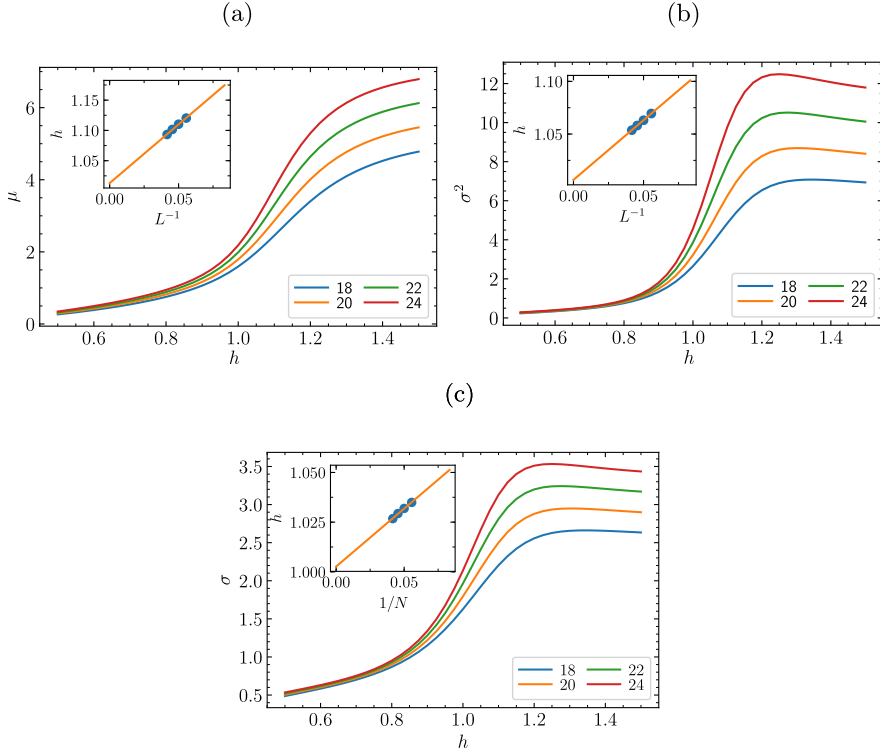


Figure 6.5: Statistical measures of the error correction times. (a) Mean, μ (b) Variance, σ^2 (c) Standard Deviation, σ as a function of the perturbation strength, h . From the Insets of each of the plots we note that the critical strength, h_c , is (a) $h_c^\mu = 1.013(3)$ (b) $h_c^{\sigma^2} = 1.007(3)$ (c) $h_c^\sigma = 1.003(1)$ implying that standard deviation, σ , has better finite size scaling properties.

6.3 Absorbing State Models

Before we extend the above method to open systems, we introduce the notion of absorbing state models [99]. Non-equilibrium phenomenon have been studied extensively in the context of classical dynamical phase transitions. One of the well known phenomenon includes the notion of absorbing state phase transitions, the dynamics of which are controlled by a definite set of rules and are generally parameterized by the *branching rate*.

6.3.1 Directed Percolation in 1D

We briefly introduce the Directed Percolation (DP) class [100, 101]. Consider a set of identical particles labeled by A with the vacuum denoted by \emptyset with the dynamics being governed by the following rules

1. Self annihilation: $A \rightarrow \emptyset$, at a rate γ_{sa}
2. Diffusion: $A + \emptyset \rightarrow \emptyset + A$, at rate γ_d
3. Coagulation: $2A \rightarrow A$, at a rate γ_c
4. Off-spring production $A \rightarrow 2A$, at a rate γ_{op}

The evolution of the system can be cast in terms of a discrete classical master equation in the Lindblad form given by

$$\dot{\rho}(t) = c\rho(t)c^\dagger - \frac{1}{2}\{c^\dagger c, \rho(t)\}, \text{ where } \{A, B\} = AB + BA \quad (6.7)$$

with the collapse operators given by

1. $c_{sa}^i = \gamma_{sa}\sigma_-^{(i)}$
2. $c_d^i = \gamma_d(\sigma_-^{(i)}\sigma_+^{(i+1)} + \sigma_+^{(i)}\sigma_-^{(i+1)})$
3. $c_c^i = \gamma_c\sigma_-^{(i)}(1 - P_1^{(i+1)})(1 - P_1^{(i)})$
4. $c_{op}^i = \gamma_{op}\sigma_+^{(i+1)}(1 - P_1^{(i)})$

where $\sigma_{+(-)}$ are creation (annihilation) operators which (de)-populate a given site by mapping $0(1) \rightarrow 1(0)$ with P_1^i being a projector which projects onto state 1 at site i . The rate at which (4) occur is generally referred to as the branching rate. For the DP universality class, below a critical branching rate the dynamics drive the system into a so called absorbing state which is defined by the absence of particles, while above the critical branching the dynamics drive the system into an active state. The DP process is marked by the presence of absorbing states, that is configurations once reached can never be left.

6.3.2 Branching Annihilating Random Walks in 2D

In this section, we extend the above introduced ideas to 2D models. We build upon the non-equilibrium dynamics of the pair conserving random walks belonging to the class of Branching Annihilating Random Walks (BARW's). We specifically consider the 2-species BARW's [102] with the species denoted by A , B and vacuum denoted by \emptyset . The dynamics of BARW's are governed by the following rules:

1. Diffusion: $A(B) + \emptyset \rightarrow \emptyset + A(B)$ with rate γ_d
2. Diffusion assisted annihilation: $A(B) + A(B) \rightarrow \emptyset$ with rate γ_{da} , i.e., if the site to which the particle diffuses is occupied by a particle of the same type both the particles annihilate
3. Parity conserving off-spring production: $A \rightarrow 2B$ with rate γ_{pcp}

As in the earlier case, the dynamics can be captured by the discrete classical master equation of the Lindblad form, as in Eq. 6.7 with the collapse operators given by

$$\begin{aligned}
 1. \quad c_d^i &= \gamma_d(\sigma_-^{(i)}\sigma_+^{(i+1)} + \sigma_+^{(i)}\sigma_-^{(i+1)}) \\
 2. \quad c_{da}^i &= \gamma_{da}\sigma_-^{(i)}(1 - P_1^{(i)}) \\
 3. \quad c_{pcp}^i &= \gamma_{pcp}\sigma_+^{(i_B+1)}\sigma_+^{(i_B-1)}(1 - P_1^{(i_A)})
 \end{aligned}$$

where $\sigma_{-(+)}$ are as defined in the earlier section, with i_A, i_B indicating the lattice sites traversed by the species A and B respectively. The branching rate is defined as the rate at which off-spring production occurs, for a pictorial representation refer to Fig. 6.10.

6.4 Detecting topological phase transitions in an open quantum setting

Earlier in the introduction of the current chapter, we had mentioned that there have been several approaches to characterize topological order for mixed states. In this section, we begin by presenting these ideas, and also note that most of these definitions are centered around defining topologically trivial states as opposed to topologically ordered states.

6.4.1 Various approaches in identifying topologically trivial mixed states

We begin with the definition introduced by Hastings as in Ref. [93]. We define a topologically trivial pure state as follows

Definition 6.4.1. *Given some Hamiltonian, H , with its ground state denoted by ψ_0 . The state ψ_0 is said to be (R, ϵ) trivial if there exists a unitary quantum circuit U with range R such that $|\psi_0 - U\psi_p| \leq \epsilon$ for some product state ψ_p .*

The above definition implies that a state is topologically trivial if it can be approximated to some product state within some precision ϵ . Unbounding R results in every state being $(L, 0)$ trivial, due to the existence of global unitary circuit connecting any state to product state. The pure state definition can be extended to a general mixed state, ρ , by comparing to a thermal state, $\rho_{cl} = Z^{-1}e^{-H_{cl}}$ where H_{cl} is a sum of local Hamiltonians with locality for each term bounded by a diameter of, at most, R and each one being diagonal in a product basis, which results in the following

Definition 6.4.2. *A density matrix, ρ is (R, ϵ) trivial if it is possible to introduce additional degrees of freedom K_i on each site, defining an enlarged Hilbert space given by $H_i \otimes K_i$ at each site, such that*

$$|\rho - \text{Tr}_{\{K_i\}}(U\rho_{cl}U^\dagger)| \leq \epsilon, \quad (6.8)$$

where $|\cdot|$ denotes the trace norm, U is a unitary quantum circuit with range R , and ρ_{cl} is a thermal state of range R with U and ρ_{cl} defined on an enlarged space and the trace is performed over the additional degrees of freedom K_i .

As in the case of pure states, if H_{cl} and dimension of K_i are unbounded (implying we consider the system, interactions and environment as a single unit) then the above definition implies that a mixed state ρ is (R, ϵ) trivial if it equal to a sum of $(R, 0)$ trivial states upto a precision of ϵ . The above definitions though advantageous in establishing that topologically ordered states cannot survive for $T > 0$ in 2D the main bottleneck is that it is tailored for thermal states [93, 98], and it is unknown whether it can be extended to any general scenario.

Motivated by the above definition, Osborne has suggested similar definitions for topologically trivial mixed state [103].

Definition 6.4.3. *A state ρ is topologically trivial if it can be expressed as a convex combination of topologically trivial pure states i.e.,*

$$\rho = \sum_j p_j |\phi_j\rangle\langle\phi_j| \quad (6.9)$$

where $|\phi_j\rangle$ is topologically trivial according to the definition of Hastings.

The following definition suggested by Osborne is based on purification. The notion of purification is based on the fact that a mixed state is obtained by tracing out additional degrees of freedom of a pure state belonging to an extended Hilbert space. For instance, consider $\rho \in H_A$, let H_B be a Hilbert space with dimensionality no less than H_A then it is always possible to find a state $|\psi\rangle \in H_A \otimes H_B$ such that $\rho = \text{Tr}_B(|\psi\rangle\langle\psi|)$, implying $|\psi\rangle$ purifies ρ .

Definition 6.4.4. *A state ρ is topologically trivial if the local purification of ρ is topologically trivial.*

The above definition implies that, ρ is topologically trivial if the state $|\psi\rangle$ that purifies it is trivial.

One other definition has been based on the notion of extending the definition of topological order based on local unitary transformations. Earlier in Chap. 2, we defined a state to be topologically ordered if it cannot be prepared from a product state via local unitaries of finite depth. In the context of mixed states, a mixed state is said to be topologically trivial if it can be prepared from a product state via local quantum channels [98] (quantum channels are defined as completely positive trace preserving operators mapping different density matrices). In Ref. [97], Grusdt has motivated the notion of topological order for thermal density matrices by studying their spectral properties while for nonequilibrium steady states the definitions are motivated by the gap of the Liouvillian superoperator of the Lindblad master equation.

The above introduced definitions mostly extend the notion of local unitary transformations introduced in the context of pure states, as in Sec. 1.2.2, to mixed states and thereby inherit the computational difficulty. Therefore, due to the lack of computability and also due to the absence of toy models hosting such states the verification of these definitions is quite limited. To this extent, in the following, motivated by the nonequilibrium phenomenon of 1D Directed Percolation and 2D Branching Annihilating Random Walks, we introduce models which host mixed topological states, thereby not only introducing novel topological phases in an open setup but also effectively predict the accompanying topological phase transition by applying the operational definition.

6.4.2 Mapping Dissipative Toric Code models to Directed Percolation in 1D

The excitations in the toric code model are given by A_v, B_p violations and are particle-like identified at the vertices and faces respectively. One of the

striking features of these excitations is that the fusion of the bosonic excitations (mostly abelian anyons) results in a vacuum. This feature has been extensively used in state preparation of topologically ordered ground states. We build on the idea as in Ref. [62] by engineering dissipative collapse operators, as in Eq. 6.10, to drive a product state into highly entangled ground state of the toric code via pure dissipative Lindbladian dynamics.

$$\begin{aligned} c_{cv}^{(i)} &= \frac{\sqrt{\gamma_v}}{2} \sigma_z^{(i)} (\mathbb{1} - A_v) \\ c_{cp}^{(j)} &= \frac{\sqrt{\gamma_p}}{2} \sigma_x^{(j)} (\mathbb{1} - B_p) \end{aligned} \quad (6.10)$$

The motivation behind such a construction is that the projector, $\frac{\mathbb{1}-A_v}{2}$ ($\frac{\mathbb{1}-B_p}{2}$) acts as probe checking whether a particular vertex (face) is excited. If a particular vertex (face) is excited the check operator equals $\mathbb{1}$ and thereby firing the σ_z operator on one of the spins attached to the vertex, which diffuses the excitation on the lattice generating a random walk. The dynamics of such a random walk can be modeled by purely dissipative Lindblad master equation [84], as in Eq. 6.11

$$\dot{\rho}(t) = \sum_n C_n \rho(t) C_n^\dagger - \frac{1}{2} [\rho(t) C_n^\dagger C_n + C_n^\dagger C_n \rho(t)] \quad (6.11)$$

Let us consider the evolution of an initial product state, which is also classical in the current scenario, under the action of the above collapse operators, as in Eq. 6.10. The collapse operators diffuse the excitations around the lattice and depending on the diffusion rate, $\gamma_{v(p)}$, after evolving for a sufficient long enough time the steady state consists of no excitations as all the excitations find a partner and fuse to the vacuum, resulting in the ground state of the toric code. This would imply that the above collapse operators cool (diffuse until fusion) the product state to the toric code ground state.

In the current scenario, to replicate the DP like process, we consider the toric code on a minimal lattice with the perturbation inducing only B_p excitations (leaving A_v sector invariant) along the second rail, as in the earlier Sec. 6.1. We encode the rules of the 1D Directed Percolation into cooling and heating collapse operators. The cooling operators, c_{cp} , are of the form introduced above, as in Eq. 6.10 with the B_p operators being replaced by three (two) boundary interaction in the bulk (boundary). In addition to the cooling operators of the B_p sector, we introduce the heating operators c_{hp} , according to

$$c_{hp}^{(j)} = \frac{\sqrt{\gamma_h}}{2} \sigma_x^{(j+1)} (\mathbb{1} - B_p) \quad (6.12)$$

6.4 Detecting topological phase transitions in an open quantum setting

which perturbs the dynamics by inducing new excitations into the system via the boundary i.e., the check operator checks the face for the presence of an excitation and if present, the adjacent face is excited by pulling an excitation from the boundary. We note that the cooling operators capture self-annihilation and diffusion while the heating operators capture coagulation and off-spring production. In addition, we also note that the excitations are allowed to fuse to the boundary only at the end of the chain, with Figs. 6.6 6.7 summarizing all the collapse operators.

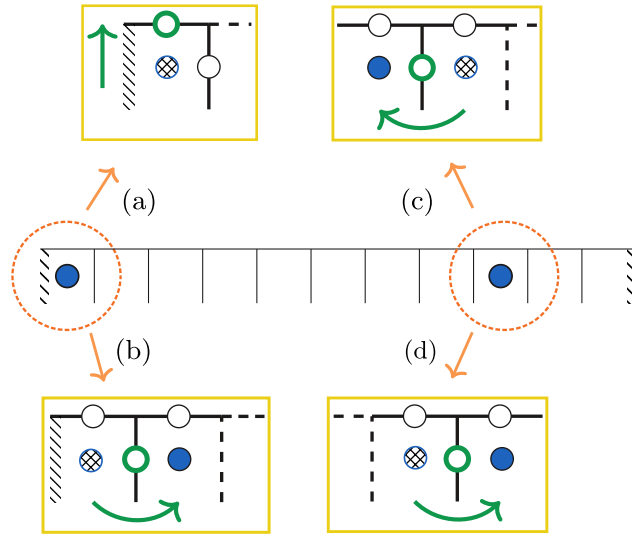


Figure 6.6: Cooling collapse operators which realize diffusion and annihilation facilitating the the dynamics of the 1D Directed Percolation. The middle row represents the position of the excitations at some time, t . The action of the different cooling operators (a) the fusing of the excitation at the end of the chain to the smooth top boundary (b) diffusion of the excitations into the bulk given a excitation sits at the boundary we have restricted movement as the excitations can only hop to the right (left) at the left (right) end. The diffusion of excitations in the bulk towards (c) the left (d) the right. The green arrow indicates the motion of the excitation while the patched circle represents the excitation at a previous time instant before the jump. The spin represented by the green outline is acted upon by the anti-commutators therefore diffusing the excitations in the bulk or fusing them at the boundary.

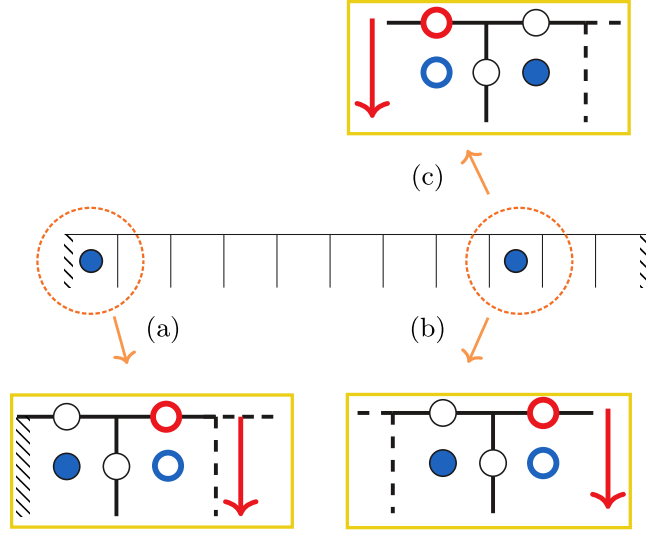


Figure 6.7: Heating collapse operators which introduce additional excitations into the system. The action of the different heating collapse operators is given by pulling B_p excitations from the smooth top boundary (a) at the left (right) ends the excitations are pulled only on the right (left), while in the bulk (b), (c) excitations can be pulled on either side. The red arrow indicates the creation of an excitation in the bulk by the action of anti-commutator on the spin represented by red outline with the position of the excitations given by blue circles and the position of new excitations given by circles with blue outline.

Ising mapped collapse operators

In the previous section, we have introduced collapse operators which extend the classical DP dynamics to the toric code model in an open quantum setting. As in the ground state analysis, we map the exact model to Ising like spins in the excitation space and compute the steady state using the Monte-Carlo Wavefunction Method (MCWF) for the classical master equation (see Appendix. D for details of the algorithm). As we identify each excitation with an Ising spin, μ , the cooling collapse operators map as follows

6.4 Detecting topological phase transitions in an open quantum setting

$$\begin{aligned}
 c_{cp}^{tc} &= \frac{\sqrt{\gamma_c}}{2} \underbrace{\sigma_x^{(i)}}_{\downarrow} \underbrace{(\mathbb{1} - B_p)}_{\swarrow} \\
 c_{cp}^{is} &= \frac{\sqrt{\gamma_c}}{2} \underbrace{\mu_p^x \mu_{p'}^x}_{\downarrow} \underbrace{(\mathbb{1} - \mu_p^z)}_{\swarrow}
 \end{aligned}$$

In the above equation, the spin i belongs to the face p in the original model while $\mu_p, \mu_{p'}$ correspond to the Ising spins in the neighboring faces, p, p' shared by the spin i . The heating collapse operators map as follows

$$\begin{aligned}
 c_{hp}^{tc} &= \frac{\sqrt{\gamma_h}}{2} \underbrace{\sigma_x^{(j+1)}}_{\downarrow} \underbrace{(\mathbb{1} - B_p)}_{\swarrow} \\
 c_{hp}^{is} &= \frac{\sqrt{\gamma_h}}{2} \underbrace{\mu_{p'}^x}_{\downarrow} \underbrace{(\mathbb{1} - \mu_p^z)}_{\swarrow}
 \end{aligned}$$

In the above equation, the spin $(j+1)$ belongs to the smooth boundary of the face neighboring p . p' is Ising spin adjacent to the face p . Therefore, the presence of excitation leads to creation of additional excitation on the neighboring face, thereby heating the system.

Critical strength in the thermodynamic limit and critical exponents

The heating rate of the dissipative dynamics, γ_h , is analogous to the branching rate of the classical DP and effectively parameterizes the dynamical phase transition. At low heating rates, most of the excitations are cooled resulting in a steady state closer to the ground state of the toric code, which in the classical DP phenomenon maps to the absorbing state while at higher heating rates the steady state has a finite density of excitations which maps to the active state of classical DP. Therefore, to capture the dynamical phase transition in thermodynamic limit, we compute the density of excitations, $n_e = \sum_i \text{Tr}(P_1^i \rho)$, where P_1^i is the projector $|1\rangle\langle 1|$ acting at site i , as a function of the time at different heating strength, as in Fig. 6.8(a). The initial state used for evolution is a fully filled state, that is the density of excitations is one at $t = 0$. We note that the curvature of the n_e versus time provides insight the nature of decay thereby allowing us to classify the phase as absorbing, critical or active. For positive (negative) curvature, we conclude that

the phase is active (absorbing or inactive) [99]. To further quantify the decay and thereby characterize the phase transition we compute the quantity, as in Eq. 6.13, which at critical heating strength decays algebraically, that is $\delta_{\text{eff}}(t)$ is a constant [104].

$$\delta_{\text{eff}}(t) = -\frac{1}{\log b} \log \frac{n_{e,\sigma}(bt)}{n_{e,\sigma}(t)} \quad (6.13)$$

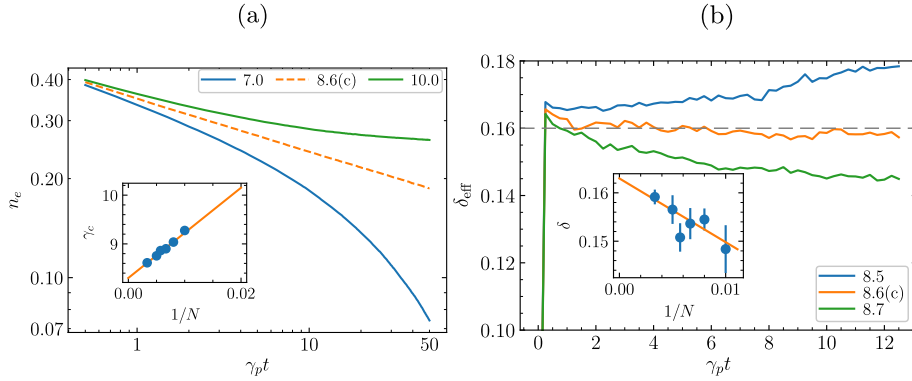


Figure 6.8: (a) Error density n_e for $N = 300$ sites at different values of γ , blue curve showing subcritical behavior, orange curve showing critical, with green curve showing supercritical behavior. Initial states were chosen to have maximum density. (Inset) Finite size scaling leads to $\gamma_c = 8.30(2)$. (b) Effective critical exponents, δ_{eff} at $b = 4$. The critical value of the transition is taken where δ_{eff} remains constant. Error bars correspond to all values consistent with a constant value in the long time limit. (Inset) Finite size scaling leads to $\delta = 0.163(5)$ in the thermodynamic limit. Errors are given by the sum of the uncertainty in the linear fit and the difference in δ between $b = 4$ and $b = 2$.

Topological critical strength, critical exponents

To capture the topological phase transition, we extend the above introduced method of error statistics to the context of mixed steady states. For the mixed steady state given by $\rho = \frac{1}{N} \sum |\psi\rangle_i \langle \psi|_i$, where N is the number of trajectories of the Monte-Carlo simulation and $|\psi\rangle_i$ corresponds to the evolved state for each trajectory. We compute the error-correction statistics averaged over all the trajectories at each time. The error correction algorithm is as outlined earlier, as in Fig. 6.4, involves parallel walkers spanning the

lattice until they meet resulting in the annihilation of the respective excitations. However, the walker annihilation is subtly modified to incorporate the boundary effects, i.e., the excitations can be annihilated at either end of the chain and due to this the walker would cease to proceed further either on crossing the path of another walker or upon meeting the boundary at the ends. As from Fig. 6.9, we note that the standard deviation, n_σ , of the error correction statistics which encodes the topological phase transition closely follows the thermodynamic transition in terms of the critical heating strength. As in the case of the thermodynamic transition, we note that the initial state chosen for evolution has a standard deviation which is maximum (i.e., the initial state used for the evolution involves a mixture of absorbing states and a states which have maximum error correction time).

To gain a more intuitive understanding on the topological phase transition we invoke the Ising duality map established earlier in Sec. 6.2.1. At $\gamma_h = 0$, in the effective Ising model we have an ensemble of product states, i.e., due to cooling we have a steady state that is an absorbing state which is topologically ordered and is reflected in the standard deviation of the time correction statistics being low in the thermodynamic limit. While at $\gamma_h \rightarrow \infty$, the ensemble is mixed (analogous to the highly entangled state in the excitation space as in the ground state analysis) implying the state is topologically trivial which is reflected in the diverging standard deviation in the thermodynamic limit. Therefore, we conclude that standard deviation is an effective signature to detect topological phases of matter and thereby topological phase transitions in an open setup.

6.4.3 Mapping Dissipative Toric Code models to BARW in 2D

In this section, we study the notion of non-equilibrium phenomenon of BARW in 2D, as introduced earlier, in the context of toric code defined on a torus. The two particle like excitations A_v and B_p violations provide a natural setting to study the 2-species BARW. To this extent, excitations of A_v , B_p sectors are identified as two species of the BARW. As in the 1D case, the rules of classical dynamics are encapsulated by engineering suitable collapse operators. The cooling collapse operators are as introduced in earlier Sec. 6.4.2, given by $c_{cv}^{tc}(c_{cp}^{tc})$, as in Eq. 6.10, while the perturbative heating collapse operators are given by

$$\begin{aligned} c_{hv}^{(i)} &= \frac{\sqrt{\gamma_{hv}}}{2} \sigma_x^{(i)} (1 - A_v) \\ c_{hp}^{(j)} &= \frac{\sqrt{\gamma_{hp}}}{2} \sigma_z^{(j)} (1 - B_p) \end{aligned} \tag{6.14}$$

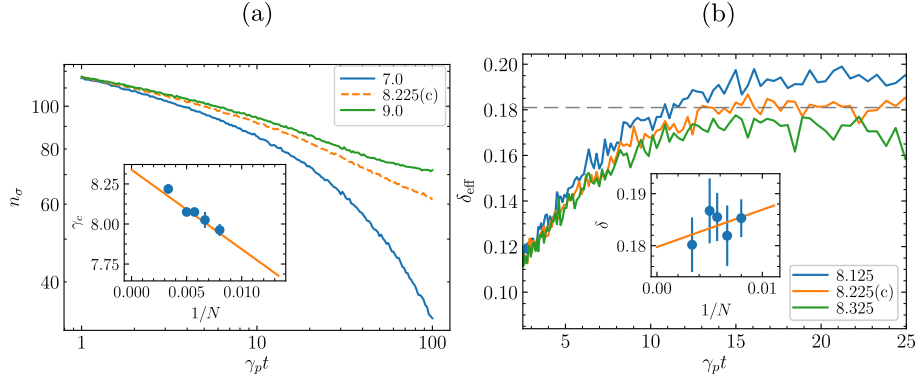


Figure 6.9: (a) Standard deviation, n_σ , of the error correction time statistics for $N = 300$ sites at different values of γ_h , blue curve showing subcritical behavior, orange curve showing critical, with green curve showing supercritical behavior. Initial states are chosen to have maximum standard deviation, therefore trivial states. (Inset) Finite size scaling leads to $\gamma_c = 8.34(5)$. (b) Effective critical exponents, δ_{eff} at $b = 4$. Finite size scaling leads to $\delta = 0.18(2)$ in the thermodynamic limit. Errors are given by the sum of the uncertainty in the linear fit and the difference in δ between $b = 4$ and $b = 2$.

The heating collapse operators generate two excitations of the other sector thereby introducing new excitations at the vertices (faces) or annihilating the already present ones. The heating rates γ_{hv}, γ_{hp} are analogous to the branching rate of the classical BARW and effectively parametrize the dynamical phase transition.

Ising mapped collapse operators

As in the case of the 1D Directed Percolation process we map the collapse operators of the original model to the Ising spins in the excitation space and generate the dynamics using the MCWF method. We identify the dual lattice with Ising spins, μ , but due to the two different sectors we have two different sectors of Ising spins, vertex and face excitations denoted by v and p respectively. The cooling collapse operators of the original model get mapped to the Ising spins as follows

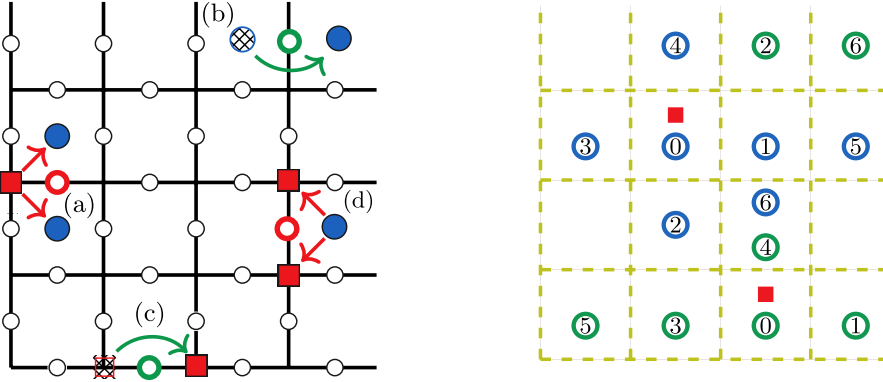


Figure 6.10: (Left) Heating [(a), (d)] and cooling [(b), (c)] collapse operators facilitating the 2-BARW dynamics. Heating collapse operators: (a) A_v violation generates B_p violations in pairs with the spin outlined in red being acted upon by σ_x (d) B_p excitation generates two A_v violations, with the spin outlined in red being acted by σ_z . Cooling collapse operators (b) B_p violations (c) A_v violations diffuse around the lattice. The hashed blue circle, hashed red square denote the position of the excitations at the previous time with the spin outlined in green being acted upon by (b) σ_x (c) σ_z . (Right) Error correction scheme for excitations in 2D. The red squares denote the position of the B_p excitations, we associate each excitation with a walker, denoted here by blue and green walkers, which span the lattice in diamond shaped patterns. We denote the position of the walker at each time instance starting from $t = 0$ to $t = 6$, which is the time taken for the walkers to cross the path of the other. Here we have considered only B_p violations, the same procedure can be extended to A_v violations.

$$\begin{aligned}
 c_{cv}^{tc} &= \frac{\sqrt{\gamma c}}{2} \underbrace{\sigma_z^{(i)}}_{\downarrow} \underbrace{(\mathbb{1} - A_v)}_{\searrow} & c_{cp}^{tc} &= \frac{\sqrt{\gamma c}}{2} \underbrace{\sigma_x^{(i)}}_{\downarrow} \underbrace{(\mathbb{1} - B_p)}_{\searrow} \\
 c_{cv}^{is} &= \frac{\sqrt{\gamma c}}{2} \underbrace{\mu_v^x \mu_{v'}^x}_{\downarrow} \underbrace{(\mathbb{1} - \mu_v^z)}_{\searrow} & c_{cp}^{is} &= \frac{\sqrt{\gamma c}}{2} \underbrace{\mu_p^x \mu_{p'}^x}_{\downarrow} \underbrace{(\mathbb{1} - \mu_p^z)}_{\searrow}
 \end{aligned}$$

where i denotes the spin which belong to the face, p , (vertex) (v), which is being probed for the presence of an excitation. $\mu_{p(v)}, \mu_{p'(v')}$ denote the Ising spins on the adjacent faces (vertices) p, p' (v, v') shared by the spin i of the original model as in Fig. 6.10. The heating collapse operators are given by

$$\begin{array}{ccc}
 c_{cv}^{tc} = \frac{\sqrt{\gamma_h}}{2} \underbrace{\sigma_x^{(i)}}_{\downarrow} \underbrace{(\mathbb{1} - A_v)}_{\searrow} & c_{cp}^{tc} = \frac{\sqrt{\gamma_h}}{2} \underbrace{\sigma_z^{(i)}}_{\downarrow} \underbrace{(\mathbb{1} - B_p)}_{\searrow} \\
 c_{cv}^{is} = \frac{\sqrt{\gamma_h}}{2} \underbrace{\mu_p^x \mu_{p'}^x}_{\downarrow} \underbrace{(\mathbb{1} - \mu_v^z)}_{\searrow} & c_{cp}^{is} = \frac{\sqrt{\gamma_h}}{2} \underbrace{\mu_v^x \mu_{v'}^x}_{\downarrow} \underbrace{(\mathbb{1} - \mu_p^z)}_{\searrow}
 \end{array}$$

where i belongs to the original model, while p, p', v, v' are defined as above. We note that in the above map, the face (vertex) is probed for the presence of an excitation, if present, a pair of adjacent Ising vertices (faces) spins are flipped.

Critical strength in the thermodynamic limit and critical exponents

We consider the dissipative dynamics induced by the above collapse operators. We set the cooling (heating) rate with respect to the vertex and face operators to $\gamma_{c(h)}$. The heating rate, as in the 1D DP, is analogous to the branching rate of the classical BARW and effectively parametrizes the dynamical phase transition. Unlike the DP case, we observe an active phase as soon as the heating is turned on, implying that the system has finite density of excitations at finite γ_h as observed in Fig. 6.11(a). For a general DP process the decay in density at criticality is given by $n_e \sim t^{-\delta}$, which for the 2D BARW reduces to $n_e \propto \log t/t$ as established in Ref. [105] and further numerically verified in Ref. [102]. Here, we reestablish the above results by plotting $n_e t$ vs. t , as in Fig. 6.11, which results in $\delta_c^{\text{thermo}} = 1$ with logarithmic corrections that behave linearly.

Topological critical strength, critical exponents

The dynamics also encode a topological phase transition, as for low heating strength the system cools into the ground state of the toric code as the excitations annihilate due to fusion. At higher heating strength, the perturbation induces additional excitations into the system and thus the steady state is a mixed ensemble. To estimate the topological phase transition, we compute the error-correction time statistics averaged over the trajectories of the MC simulation. The error-correction algorithm closely follows the description of the 1D error-correction algorithm, i.e., we identify each excitation with a unique walker and the walker spans the lattice in diamond shaped patterns corresponding to a constant Manhattan distance from the initial site, until it crosses the path of another walker, see Fig. 6.10(b). The maximum of

6.4 Detecting topological phase transitions in an open quantum setting

the time taken for all the walkers to meet is taken as the error correction time for a given state. For the case of the toric code, the excitations being abelian, braiding introduces only a phase factor which does not influence the statistical properties, as the amplitudes contributing to the statistics remain insensitive to the phase. Due to the above reason the same error correction scheme can be considered for different sectors and also we note that we can extend the above error correction scheme to all topological phases sporting abelian anyons. In a more general context, for non-abelian anyons, the error correction scheme is more sophisticated considering the fact that the braiding results in a non-trivial unitary instead of a phase correction and this would eventually impact the amplitudes and thereby the statistical properties. We compute the standard deviation of the statistics and note that the critical strength for the topological phase transition follows the thermodynamic behavior i.e., the system is topologically ordered for $\gamma_h = 0$, while is trivial for all finite heating strength, see Fig. 6.11(b). From Fig. 6.11(b), we establish that $\delta_c^{\text{topo}} = 1$ with logarithmic corrections that behave in a quadratic fashion. The difference in behavior of the logarithmic corrections distinguishes the topological criticality from the criticality in the thermodynamic limit, further distinguishing the thermodynamic and topological phase transition.

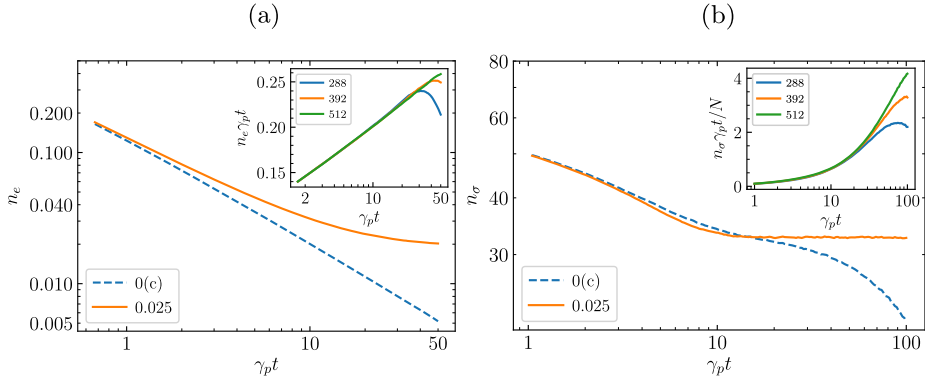


Figure 6.11: Two-dimensional topological criticality. (a) Error density, n_e and (b) circuit depth, n_σ for $N = 512$ sites and $\gamma_h = 0$ (dashed) and $\gamma_h = 0.025 \gamma_c$. (Inset) The logarithmic corrections to a t^{-1} decay, with a linear behavior for the (a) error density and a quadratic behavior for the (b) topological transition before finite size effects become relevant.

Part IV

Robustness of symmetry protected topological order

Chapter 7

Phase transitions in Su-Schrieffer-Heeger models via error correction

In this part, we extend the operational definition to topological insulators [106, 107, 108, 109], by considering variants of the Su-Schrieffer-Heeger (SSH) model [110, 111, 112, 113, 114]. This class of models host phases which are signaled by various topological invariants, for instance Chern number, winding number in the context of periodic boundaries, while giving rise to edge modes in the context of open boundaries and hence are termed as topological phases. These phases are short range entangled in contrast to the long range entangled toric code ground states which we have explored in the previous chapters [11]. The ground states of these phases can be generated from product states using local unitaries of constant depth with the unitaries necessarily breaking the symmetry of the state. If instead symmetry preserving unitaries are considered then the depth of unitaries scales with the system size [115]. We begin by introducing the SSH model taking note of the topological phases in both periodic and open boundary conditions while keeping track of the topological invariants which signal the presence of symmetry protected topological order.

7.1 SSH Model

We begin by introducing the hardcore boson variant of the SSH model, by considering a 1D chain of $2N$ spin-1/2 particles, whose Hamiltonian is given

by

$$\begin{aligned}
 H_{hb} &= v \sum_{i=1}^N \sigma_-^{2i-1} \sigma_+^{2i} + \text{h.c} \\
 &+ w \sum_{i=1}^{N-1} \sigma_-^{2i} \sigma_+^{2i+1} + \text{h.c}
 \end{aligned} \tag{7.1}$$

where $\sigma_+ = (\sigma_x + i\sigma_y)/2$, $\sigma_- = (\sigma_x - i\sigma_y)/2$ which are generally referred to as creation and annihilation operators. As each site in the chain has two levels, the Hamiltonian effectively captures hopping of particles. For example, consider the presence (absence) of a particle to be given by the spin-1/2 state $|0\rangle(|1\rangle)$, the action of the above Hamiltonian flips the spin states on the neighboring sites, thereby effectively capturing the hopping.

The effective particle hopping captured by the above Hamiltonian can be recast as fermions hopping on a $2N$ site chain by using the Jordan-Wigner transformation

$$\begin{aligned}
 \sigma_+^i &= \prod_{j=1}^{i-1} (1 - 2c_j^\dagger c_j) c_i \\
 \sigma_-^i &= \prod_{j=1}^{i-1} (1 - 2c_j^\dagger c_j) c_i^\dagger \\
 \sigma_z^i &= 1 - 2c_i^\dagger c_i
 \end{aligned} \tag{7.2}$$

where c_i and c_i^\dagger are fermionic operators that annihilate and create fermions at site i . The Hamiltonian in the second quantization formalism using the fermionic operators is given by

$$H_{sq} = \left[v \sum_{i=1}^N c_{2i-1}^\dagger c_{2i} + w \sum_{n=1}^{N-1} c_{2n}^\dagger c_{2n+1} \right] + \text{h.c} \tag{7.3}$$

We note that the above Hamiltonian find its origins in describing the electron hopping in insulators such as polyacetylene [110].

The fermionic version of the Hamiltonian in the first quantization formalism is given by

$$H_{pb}^{AB} = v \sum_{n=1}^N (|n, B\rangle\langle n, A| + \text{h.c}) + w \sum_{n=1}^{N-1} (|n+1, A\rangle\langle n, B| + \text{h.c}) \tag{7.4}$$

with N being the position basis and A, B being the internal degrees of freedom at each unit cell. The Hamiltonian for each unit cell can be described as $H = H_{ext} \otimes H_{int}$, with $|N, A\rangle = |N\rangle \otimes |A\rangle$. We note a subtle yet crucial observation regarding the choice of unit cell. There are two choices for the

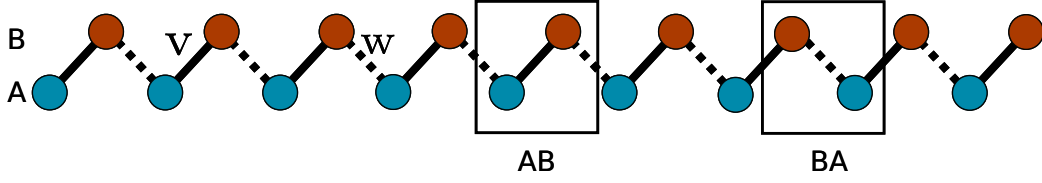


Figure 7.1: SSH chain with hopping denoted by v and w with the external unit cells $N=10$ for the choice of the unit cell AB , each hosting two internal sites labeled by the blue and brown circles. With respect to the AB unit cell, in the limit of $w = 0, v \neq 0$ we have intra-sites dimers with no edge modes while in the limit of $v = 0, w \neq 0$ we have inter-sites dimers resulting with zero energy edge modes. The available choice of the unit cells denoted by AB, BA .

unit cell one involving the sites A, B , the other with sites B, A , as in Fig. 7.1, leading to the Hamiltonian, H_{pb}^{AB} as above in Eq. 7.4 and H_{pb}^{BA} given by

$$H_{pb}^{BA} = w \sum_{n=2}^N (|n, A\rangle\langle n, B| + \text{h.c.}) + v \sum_{n=1}^N (|n+1, B\rangle\langle n, A| + \text{h.c.}) \quad (7.5)$$

The choice of the unit cell plays a major role in defining various topological signatures, therefore an accurate classification of the topological phases should include the information on the unit cell. Having introduced the different variants of the Hamiltonian with open boundaries, we now proceed to discuss the properties of the bulk (by closing the chain) and boundary properties which encode topological invariants thereby characterizing these phases as topological phases.

7.1.1 Topological Invariants

We close the chain of the Hamiltonian in Eq. 7.4 by adding the inter-site hopping between the first site of the first unit cell and the second site of the N^{th} unit cell, i.e., we include the term $\sigma_-^{2N} \sigma_+^1$ and its conjugate scaled by the potential w . The introduction of periodicity leaves the system translational invariant. We perform a Fourier transform on the position basis of Hamiltonian Eq. 7.4 [116]. This gives rise to the band Hamiltonian acting on the internal sites for each unit cell parameterized by momentum, k , as in Eq. 7.6

$$H(k) = \begin{bmatrix} 0 & v + we^{ik} \\ v + we^{-ik} & 0 \end{bmatrix} \quad (7.6)$$

where $k \in \{\delta, 2\delta, \dots, N\delta\}$, where $\delta = \frac{2\pi}{N}$ with eigen energies given by

$$E(k) = |v + e^{-ik}w| = \pm\sqrt{v^2 + w^2 + 2vw \cos(k)} \quad (7.7)$$

We plot the dispersion relation at different v, w , as in Fig. 7.2 and note that at $v \neq w$ there exists a finite energy gap while in the case of $v = w$ the gap closes indicating the presence of a phase transition between the insulating phases defined in the limits of $v < w$ and $v > w$. The phases in the either

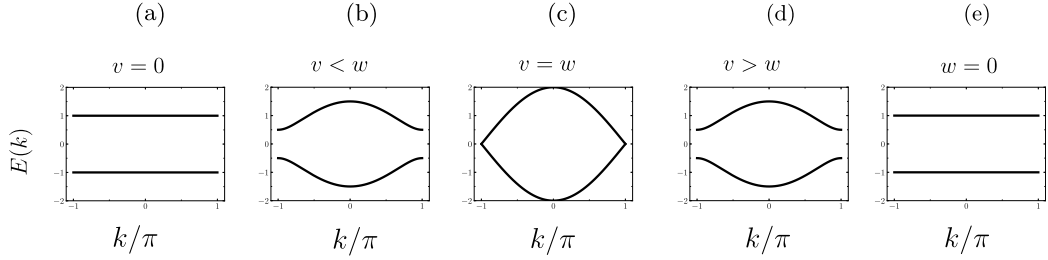


Figure 7.2: Energy bands as a function of the wavenumber, k , for (a) $v = 0$ (b) $v < w$ (c) $v = w$ (d) $v > w$ (e) $w = 0$. We note the closing of the band gap at $v = w$ signaling the presence of a criticality.

limit being distinct we search for properties which vary as we vary v, w . To this extent, we note that the above Hamiltonian can be re-cast as

$$H(k) = d_x(k)\sigma_x + d_y(k)\sigma_y + d_z(k)\sigma_z \quad (7.8)$$

where $d_x(k) = v + w \cos k$, $d_y(k) = -w \sin k$, $d_z(k) = 0$. The vector $\mathbf{d}(k)$ traces out a circle in the xy -plane centered at $(v, 0)$ with radius w . We note that in the limit of $v < w$ the vector winds around the origin, while in the other limit $v > w$ the vector does not include the origin as in Fig. 7.3. This interesting property can be used to distinguish between the different possible phases. To further consolidate the above notion, we introduce the winding number with respect to the the unit cell AB , ν_{AB} as follows [112]

$$\nu_{AB} = \frac{1}{2\pi i} \int_{-\pi}^{\pi} dk \frac{d}{dk} \log h(k) \quad (7.9)$$

where $h(k)$ is the off diagonal element of the momentum Hamiltonian, which in the current scenario is given by $d_x(k) - id_y(k)$. We note that the above is one of the definitions for winding number among many others which are all

7.1 SSH Model

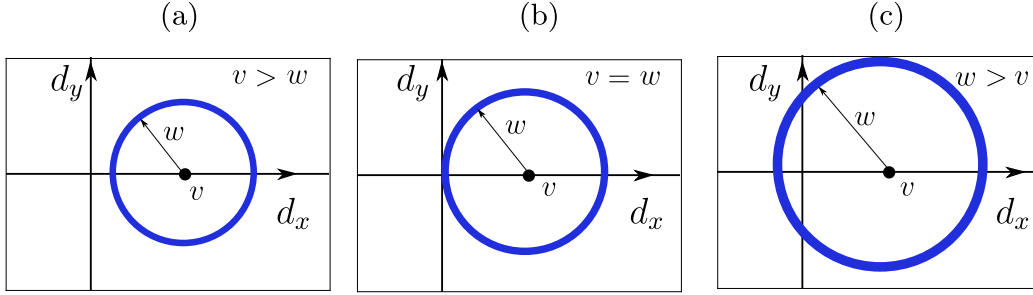


Figure 7.3: The circle traced by the vector $\mathbf{d}(k)$ (a) does not include the origin for $v > w$ (b) passes through the origin for $v = w$ (c) includes the origin for $v < w$ resulting in a winding number of (a) $\nu = 0$ (b) undefined (signaling the presence of a transition, i.e., we have a conductor due to the gap closing) (c) $\nu = 1$, for the choice of the unit cell AB .

equivalent, for an exhaustive list and their equivalence we refer the reader to the Ref. [117]. In the current scenario ν_{AB} reduces to

$$\nu_{AB} = \frac{1}{2\pi} \int_{-\pi}^{\pi} dk \frac{d}{dk} \arg(h) \quad (7.10)$$

The solution of the above integral relies on whether or not the curve $\mathbf{d}(k)$ given by $v + we^{-ik}$ includes the origin (which acts as a pole). For the case of $v < w$ we note that $\nu_{AB} = 1$ while in the limit of $v > w$, $\nu_{AB} = 0$. In a more general context, we note the following equivalent definition of the winding number [112]

$$\nu = \int_{-\pi}^{\pi} \left(\tilde{\mathbf{d}}(k) \times \frac{d}{dk} \tilde{\mathbf{d}}(k) \right)_z dk \quad (7.11)$$

with $\tilde{\mathbf{d}} = \frac{\mathbf{d}}{|\mathbf{d}|}$ which projects the curve $\mathbf{d}(k)$ onto a unit circle. The winding number is topological in nature, as it does not depend on the path traced by $\mathbf{d}(k)$ but rather depends only on whether the origin is enclosed by $\mathbf{d}(k)$ vector. In the current context, the above property of the winding number remains invariant in the limits of $v < w$ (distinct but still invariant in the limits of $w < v$) for a given choice of the unit cell, hence acting as a topological invariant in either limits thereby classifying the distinct phases.

In the above, we have computed the winding number by fixing the choice of the unit cell to be AB . It is also possible to choose the other unit cell, BA , leading to the Hamiltonian as in Eq. 7.5 the band Hamiltonian of which

is given by

$$H(k) = \begin{bmatrix} 0 & w + ve^{-ik} \\ w + ve^{ik} & 0 \end{bmatrix} \quad (7.12)$$

which results in the vector $\mathbf{d}'(k)$, whose components are given by

$$d'_x(k) = w + v \cos k, \quad d'_y(k) = w \sin k, \quad d'_z(k) = 0.$$

In the current scenario, the winding number, ν_{BA} is 1 in the limit of $w > v$ while is 0 in the limit of $w < v$. The phase with the non-vanishing winding number is classified as a topological phase. Due to the choice of the unit cell, the phases in either of the limits are topological in nature and are distinct due to the gap closing at $v = w$.

7.1.2 Edge states

In the open boundary context, the Fourier transform no longer diagonalizes the Hamiltonian and therefore does not provide any additional insight. By observing the Hamiltonian, Eq. 7.4, in the limit of $w \rightarrow 0$, we have fully dimerized states, with eigenstates given by the superposition of the internal sites i.e.,

$$H_{pb}^{AB}(|n, A\rangle \pm |n, B\rangle) = \pm(|n, A\rangle \pm |n, B\rangle) \quad (7.13)$$

this is an insulating phase as the particles cannot hop between sites.

While in the limit of $v \rightarrow 0$, we again have fully dimerized states, with the eigenstates given by the superposition as in Eq. 7.14

$$H_{pb}^{AB}(|n+1, A\rangle \pm |n, B\rangle) = \pm(|n+1, A\rangle \pm |n, B\rangle) \quad (7.14)$$

this is also an insulating phase as the movement of particles is restricted. In this limit, in addition to the above eigenstates we also have two additional states with zero energy i.e.,

$$H_{pb}^{AB}|1, A\rangle = H_{pb}^{AB}|N, B\rangle = 0 \quad (7.15)$$

due to the absence of on-site potential and with no extra energy needed to clamp the electrons we have two zero energy modes at the edges of the chain which is a characteristic of topological order.

To summarize, for the choice of the unit cell denoted by AB in the limit of $v < w$ the phase is SPT while for the choice of the unit cell denoted by BA in the limit of $v > w$ the phase is SPT. This implies that the two insulating phases are SPT ordered and we denote these phases by SPT^{AB} and SPT^{BA} . On a more general note, topological insulators are characterized by insulating bulk and conducting edges, here in the current scenario we have zero energy edge modes which characterize the SSH topological insulator.

7.2 Error correction statistics to probe the phase transition

We extend the operational definition introduced for intrinsic topological order to the case of symmetry protected topological phases by imposing symmetry conditions on the error correction circuit. In this framework, a state is said to be symmetry protected topologically ordered if it can be corrected by a finite depth symmetric error correction circuit. To this extent, we introduce an excitation basis, then represent the ground state of the Hamiltonian, H_{hb} at different v, w as a superposition of the excited states and compute the time taken to annihilate the errors while imposing constraints on the detection of errors which preserve the symmetry of the topological phase.

7.2.1 Excitation space

We consider the map between the states of the excited space, $\{|0\rangle, |+\rangle, |-\rangle, |1\rangle\}$ and the two qubit physical spins given by

$$\begin{bmatrix} |0\rangle \\ |+\rangle \\ |-\rangle \\ |1\rangle \end{bmatrix} = \begin{bmatrix} 1 & 0 & 0 & 0 \\ 0 & \frac{1}{\sqrt{2}} & \frac{1}{\sqrt{2}} & 0 \\ 0 & \frac{1}{\sqrt{2}} & -\frac{1}{\sqrt{2}} & 0 \\ 0 & 0 & 0 & 1 \end{bmatrix} \begin{bmatrix} |00\rangle \\ |01\rangle \\ |10\rangle \\ |11\rangle \end{bmatrix} \quad (7.16)$$

where $|0\rangle, |1\rangle$ denote the presence (absence) of a particle as introduced in Eq. 7.1. The SSH Hamiltonian in the hardcore bosonic limit is given by, H_{hb} , as in Eq. 7.1, which in the excited space translates to H_{hbe}^{AB} by the action of the unitary U on the combined 2-qubit set given by $[1, 2N], [2, 3], \dots, [2N-2, 2N-1]$

$$\begin{aligned} H_{hbe}^{AB} = & \frac{v}{2} \left[T_{1,2N}^{a\dagger} \otimes T_{2,3}^a + \right. \\ & + \sum_{i=2}^{2N-4} T_{i,i+1}^b \otimes T_{i+2,i+3}^a \\ & \left. + T_{1,2N}^{b\dagger} \otimes T_{2N-2,2N-1}^b + \text{h.c} \right] \\ & + w \left[\sum_{i=2}^{2N-2} \left(|+\rangle\langle+| - |-\rangle\langle-| \right)_{i,i+1} \right] \end{aligned} \quad (7.17)$$

with $T_{i,j}^a, T_{i,j}^b$

$$\begin{aligned} T_{i,j}^a &= |0\rangle\langle+| + |+\rangle\langle 1| - |0\rangle\langle-| + |-\rangle\langle 1| \\ T_{i,j}^b &= |+\rangle\langle 0| + |1\rangle\langle+| + |-\rangle\langle 0| - |1\rangle\langle-| \end{aligned} \quad (7.18)$$

with the subscript i, j denoting the physical qubits which are considered together.

For the action of the unitary U on the combined 2-qubit set given by $[1, 2], [3, 4], \dots, [2N - 1, 2N]$ we have the Hamiltonian H_{hbe}^{BA} given by

$$H_{hbe}^{BA} = \frac{w}{2} \left[\sum_{i=1}^{2N-3} T_{i,i+1}^b \otimes T_{i+2,i+3}^a + \text{h.c.} \right] + v \left[\sum_{i=1}^{2N-1} \left(|+\rangle\langle+| - |-\rangle\langle-| \right)_{i,i+1} \right] \quad (7.19)$$

The ground state of the Hamiltonian H_{hbe}^{AB} in the limit of $v \rightarrow 0$ is given by $|-\rangle_{[1,2N]}, |-\rangle_{[2,3]}, \dots, |-\rangle_{[2N-2,2N-1]}$ and the Hamiltonian H_{hbe}^{BA} in the limit of $w \rightarrow 0$ is given by $|-\rangle_{[1,2]}, |-\rangle_{[3,4]}, \dots, |-\rangle_{[2N-1,2N]}$.

Errors and the correction strategy

Having constructed the excitation basis, we now examine the possible errors and relevant error correction strategies in order to successfully capture the phase transition using the operational definition. From the Hamiltonians, H_{hbe}^{AB} , H_{hbe}^{BA} , we note that the excited space consists of phase errors given by $|+\rangle$ and density fluctuations given by $|\mathbf{0}\rangle, |\mathbf{1}\rangle$. The error correction strategy involves correcting the phase and density fluctuations and hence involves two steps as follows:

1. We identify the $|+\rangle$ sites in the excitation space with walkers which annihilate if one of the following conditions is met
 - (a) It crosses the path of another $|+\rangle$ walker which is traversing the ring (the walker traverses on a 1D ring irrespective of whether the original spin chain is periodic or open, (or)
 - (b) It meets a site with density fluctuations ($|\mathbf{0}\rangle, |\mathbf{1}\rangle$) (or)
 - (c) The walker crosses the boundary, the boundary here is identified as the first site and the last site joined together, with no $|+\rangle$ walker at the boundary
2. With the walkers associated to the $|+\rangle$ site being annihilated, say in time t_p , we turn to the density fluctuations and compute the time taken to annihilate the density fluctuations, which involves pairing of $\mathbf{1}$'s and $\mathbf{0}$'s. To this extent, we initiate a unique walker at every site which has $\mathbf{1}$ and $\mathbf{0}$ which parallelly span the 1D ring. The $\mathbf{1}$ walker annihilates with the $\mathbf{0}$ walker when their paths meet. Therefore, the total time of

the error correction is given by time taken for all $\mathbf{1}$ walkers to meet with the corresponding $\mathbf{0}$ walkers, say given by time t_d .

3. The total time for correcting a state is given by $t_p + t_d$.

7.3 Error correction statistics via Matrix Product State simulations

To capture the topological phase transition using the operational definition, we employ the tools of Matrix Product States (MPS) methods to compute the ground state, $|\psi_{vw}\rangle$, given v, w . We then perform a series of measurements in the excitation space (joint physical basis) averaging it over many trajectories, thereby reconstructing the ground state. In other words, we represent the ground state in terms of the excited states. To summarize, the operational definition involves the following procedure:

1. Compute the ground state, $|\psi_{vw}\rangle$, using MPS methods (We use the Density Matrix Renormalization Group (DMRG) algorithm and AutoMPS methods from ITensor package [118])
2. Perform a measurement in the excitation space depending on the reference state, that is either :

$$\begin{aligned}
 & |1, \underbrace{2\ 3}, \dots, \underbrace{2N-2\ 2N-1}, 2N\rangle \rightarrow | \underbrace{1\ 2N}_1, \underbrace{2\ 3}_2, \dots, \underbrace{2N-2\ 2N-1}_N \rangle \\
 & \qquad \qquad \qquad \text{(or)} \\
 & | \underbrace{1\ 2}, \underbrace{3\ 4}, \dots, \underbrace{2N-1\ 2N} \rangle \rightarrow | \underbrace{1\ 2}_1, \underbrace{3\ 4}_2, \dots, \underbrace{2N-1\ 2N}_N \rangle
 \end{aligned}$$

where each of the brackets maps to one of $\{|\mathbf{0}\rangle, |+\rangle, |-\rangle, |\mathbf{1}\rangle\}$. Each measurement is performed by a projection operator, with the MPS wavefunction reconfiguring its correlations after each measurement [119].

3. We repeat the above step over many trajectories, therefore representing the ground state as a superposition of the excited states

$$|\psi_v^p\rangle = \sum c_\gamma |\alpha_1, \alpha_2, \dots, \alpha_N\rangle \quad (7.20)$$

where α_i 's belong to the excitation space.

4. For each trajectory we compute the time taken to correct the phase and density fluctuations, leading to the computation of time statistics obtained by averaging over all the trajectories.

7.3.1 Periodic Boundary

We consider the Hamiltonian, H_{hb} as in Eq. 7.1 with the additional term connecting the first site of the 1st unit cell and the second site of the N^{th} unit cell scaled by the hopping potential w . To establish that the phase SPT^{AB} defined in the limits of $v < w$ is SPT we consider the ground state of the Hamiltonian H_{hbe}^{AB} in the limit of $v \rightarrow 0$, given by $|-_{[1,2N]}, -_{[2,3]}, \dots, -_{[2N-2,2N-1]}\rangle$ as the reference state, this is by observing the Hamiltonian, H_{hb} . We express the ground state at any given v, w as a superposition of the excited states given by the coupling of the form $\{[1, 2N], [2, 3], \dots, [2N - 2, 2N - 1]\}$. We note that in the limit of $v/w < 1$ the phase is SPT ordered as the standard deviation, σ , of the time correction statistics is bounded, while in the limit of $v/w > 1$ the standard deviation diverges, as in Fig. 7.4. The divergence of the standard deviation does not directly imply that the phase is topologically trivial, as to establish topological triviality would imply that the standard deviation should diverge with every other topological phase. On the contrary, in the limit of $v > w$, we know that the phase SPT^{BA} is SPT ordered. To consolidate the above notion, we consider the ground state of the Hamiltonian H_{hbe}^{BA} in the limit of $w \rightarrow 0$, given by $|-_{[1,2]}, -_{[3,4]}, \dots, -_{[2N-1,2N]}\rangle$ as the reference state. We compute the time correction statistics as established for the case of SPT^{AB} and note that the standard deviation is bounded for $v/w > 1$, implying SPT^{BA} is SPT ordered, while it diverges for $v/w < 1$ as in Fig. 7.4. In Fig. 7.4, we compare v_c in the thermodynamic limit obtained via employing (i) the error correction strategy which involves density fluctuations alone while ignoring the phase fluctuations (DP), with (ii) the error correction strategy which involves both density and phase fluctuations (DPF). We note that for higher system sizes both the above strategies result in v_c which are almost the same while for smaller system sizes we notice a deviation. Due to this, we observe that there is an overall deviation at which the transition occurs in the thermodynamic limit which is obtained by performing finite size analysis. We attribute the overall deviation in v_c in the thermodynamic limit to the phase fluctuations which strongly influence the statistics in small system sizes.

7.3.2 Open Boundary

We consider the Hamiltonian, H_{hb} as in Eq. 7.1 with open boundaries. To establish that SPT^{AB} as SPT ordered we follow the same prescription as above, that is perform the error correction with $|-_{[1,2N]}, -_{[2,3]}, \dots, -_{[2N-2,2N-1]}\rangle$ as the reference state. We note that the standard deviation is bounded in the limit of $v/w < 1$ while it diverges in the limit of $v/w > 1$ as in Fig. 7.5,

7.3 Error correction statistics via Matrix Product State simulations

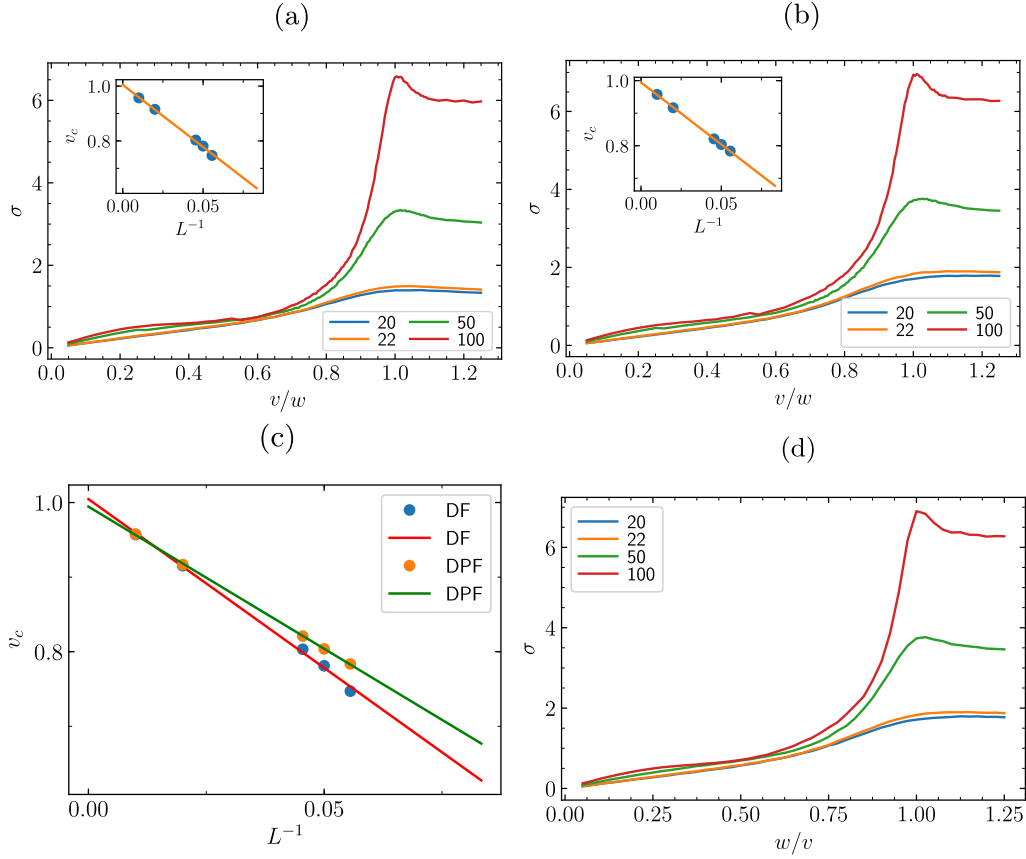


Figure 7.4: Standard deviation, σ , of error correction statistics as a function of v/w in the periodic boundary context. To detect the SPT phase in the limit of $v/w < 1$ we consider the reference state as $|-\lceil_{[1,2N]}, -\lceil_{[2,3]}, \dots, -\lceil_{[2N-2,2N-1]}\rangle$ and compute the error correction statistics by annihilating (a) density fluctuations (DF) alone resulting in $v_c = 1.01(1)$ (b) both density and phase fluctuations (DPF) resulting in $v_c = 1.00(1)$. (c) Finite size scaling analysis with DF alone and DPF both, we note that v_c remains almost the same for large system sizes though in the smaller system sizes the effect of phase fluctuations are pretty strong resulting in a deviation of v_c . (d) Standard deviation as a function of w/v with the reference state as $|-\lceil_{[1,2]}, -\lceil_{[3,4]}, \dots, -\lceil_{[2N-1,2N]}\rangle$ and the error correction strategy involving annihilation of DPF. We note that in the limit of $w/v < 1$ we note that the phase is SPT ordered as σ is bounded.

reconfirming the fact that SPT^{AB} is SPT ordered in the limit of $v/w < 1$. On similar lines we establish that SPT^{BA} is SPT ordered by observing that the

standard deviation of the error correction statistics is bounded in the regime of $v/w > 1$ while is unbounded in $v/w < 1$ with respect to the reference state given by $\{|_{-[1,2]}, |_{-[3,4]}, \dots, |_{-[2N-1,2N]}\rangle$ as in Fig. 7.5. As in the periodic case, we compare the criticality in the thermodynamic limit obtained via employing the error strategies including and excluding phase fluctuations. We note a similar deviation in v_c in the thermodynamic as in the periodic boundary case and attribute this to the strong phase fluctuations in smaller system sizes.

7.4 Extended Bosonic SSH Model

In this section, we consider the extended bosonic SSH model [113, 120] given by the Hamiltonian

$$\begin{aligned}
 H_{eb} = & \frac{v}{2} \sum_{i=1}^N (\sigma_{2i-1}^x \sigma_{2i}^x + \sigma_{2i-1}^y \sigma_{2i}^y + \delta \sigma_{2i-1}^z \sigma_{2i}^z) \\
 & + \frac{w}{2} \sum_{i=1}^{N-1} (\sigma_{2i}^x \sigma_{2i+1}^x + \sigma_{2i}^y \sigma_{2i+1}^y + \delta \sigma_{2i}^z \sigma_{2i+1}^z)
 \end{aligned} \tag{7.21}$$

with N external unit cells each hosting two internal sites. In the limit of $\delta = 0$, the above model reduces to SSH model discussed in the previous section, while in the limit of $\delta = 1$, it reduces to the Heisenberg model. In the limit of $\delta \rightarrow 0$ as analyzed earlier there exists two distinct SPT phases in the limits of $w > v$ and $w < v$. For $\delta \rightarrow \infty$, it is clear that the phase is anti-ferromagnetic, therefore the above Hamiltonian hosts three distinct phases out of which two are symmetry protected topological phases and an anti-ferromagnetic phase characterized by the parameters v , w and δ . We extend the operational definition introduced earlier with an aim to detect the above phases.

7.4.1 Excitation space

The above Hamiltonian hosts atleast three distinct phases, thereby to successfully detect these using the operational definition we need to define atleast three reference states and related error correction strategies.

SPT phases:

From the analysis of the previous section, we have established that the SSH chain has two distinct SPT phases. Therefore in the low δ regime, we expect

7.4 Extended Bosonic SSH Model

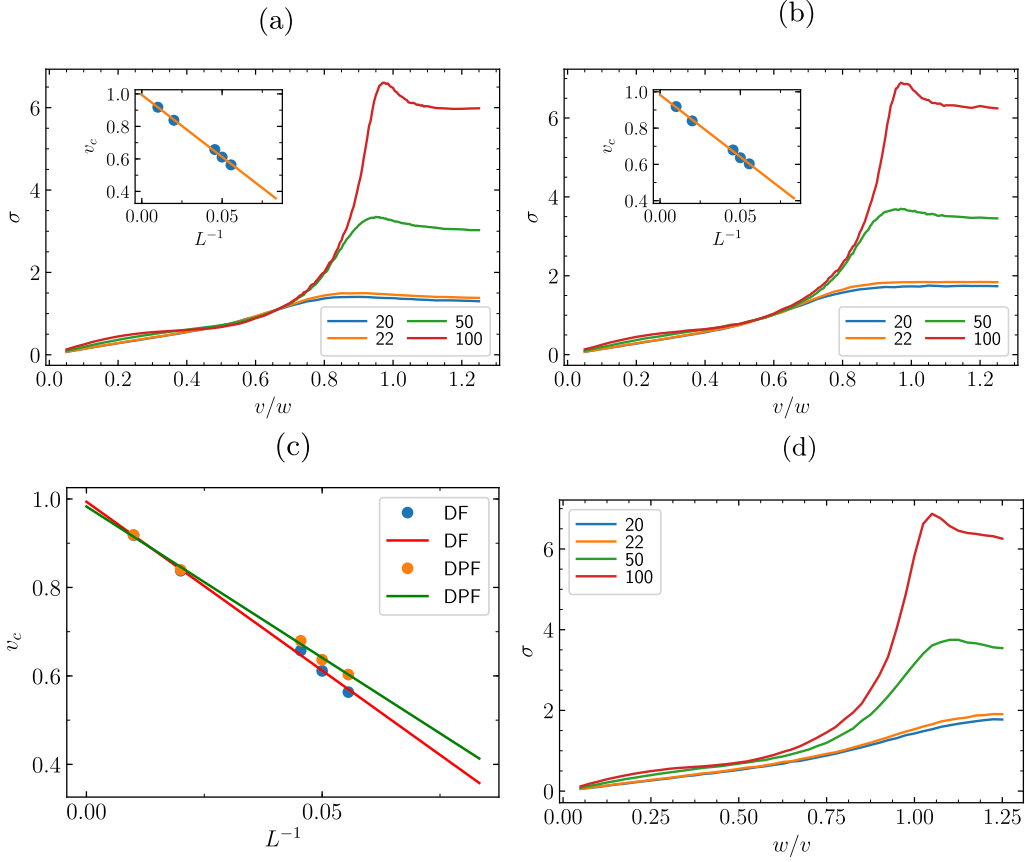


Figure 7.5: Standard deviation, σ , of error correction statistics as a function of v/w in the open boundary context. To detect the SPT phase in the limit of $v/w < 1$ we consider the reference state as $|-_{[1,2N]}, -_{[2,3]}, \dots, -_{[2N-2,2N-1]}\rangle$ and compute the error correction statistics by annihilating (a) density fluctuations (DF) alone resulting in $v_c = 0.99(1)$ (b) both density and phase fluctuations (DPF) resulting in $v_c = 0.98(1)$. (c) Finite size scaling analysis with DF and DPF, as noted in the periodic boundary case, v_c remains almost the same for larger system sizes with phase fluctuations being heavy in the small system sizes leading to the deviation in v_c in the thermodynamic limit obtained via the different error correction strategies. (d) Standard deviation, σ , as a function of w/v with the reference state as $|-_{[1,2]}, -_{[3,4]}, \dots, -_{[2N-1,2N]}\rangle$ and the error correction involving the annihilation of DPF both. In the limit of $w/v < 1$, we note that the phase is SPT ordered as σ is bounded.

to observe these distinct SPT phases in the limits of $w/v > 1$, this is similar to SPT^{AB} at $\delta = 0$ and $v/w > 1$ is similar to SPT^{BA} at $\delta = 0$. To detect the different SPT phases, we consider the excitation space of $\{|\mathbf{0}\rangle, |+\rangle, |-\rangle, |\mathbf{1}\rangle\}$ as established in the earlier section 7.2.1. In the limit of $w/v \gg 1$, motivated by the results from the SSH model we consider the reference state $|_{-[1,2N], -[2,3], \dots, -[2N-2, 2N-1]}\rangle$ while in the other limit of $v/w \gg 1$, we consider the reference state to be given by $|_{-[1,2], -[3,4], \dots, -[2N-1, 2N]}\rangle$.

Anti-Ferromagnetic phase:

For the case of anti-ferromagnetic phase, we consider the excitation space to be given by the notion of domain walls. The ground state in the limit of $\delta \rightarrow \infty$ is given by $|0101\dots 01\rangle/|1010\dots 10\rangle$, the domain walls around each site are computed by observing its neighbors. A domain wall is identified if the site and its neighbor share the same state, for example, consider the state $|\dots 0_i 1_j 0_k \dots\rangle$ somewhere in the bulk, in the excitation space there are no domain walls with respect to the site j and thereby the state is represented by $|\dots 0_{ij} 0_{jk} \dots\rangle$. Instead if the state were given by $|\dots 0_i 0_j 1_k \dots\rangle$, the equivalent excited state is given by $|\dots 1_{ij} 0_{jk} \dots\rangle$. In general, given a state we construct its domain wall representation as follows

$$\dots, \underbrace{0_i, 1_j, 1_k, 0_l, \dots}_{\text{domain wall}} \longrightarrow \dots, 0_{ij}, 1_{jk}, 0_{kl}, \dots$$

As we consider only open chains in our analysis, we note that the number of domain walls are one less compared to the interacting physical spin-1/2 s, arising out of the fact that we do not compare the first and the last site. This indeterminacy leaving the boundary free allows us to define an appropriate error correction strategy in the presence of odd domain walls, which we shall describe in the next section.

7.4.2 Error Correction

Having defined the reference state and the excitation space, we propose appropriate error correction strategies given the reference phase.

SPT phase:

The error correction strategy involves annihilating the $|+\rangle$ phase fluctuations followed by the annihilation of the density fluctuations as outlined in the

7.4 Extended Bosonic SSH Model

Sec. 7.2.1. The standard deviation, σ , of the error statistics obtained by considering the reference state as $|-_{[1,2N]}, -_{[2,3]}, \dots, -_{[2N-2,2N-1]}\rangle$ results in accurately detecting one of the SPT phases at $\delta = 0, 3$ as in Fig. 7.6, while in Fig. 7.7(a) we plot σ as a function of δ, v, w for a system size of $N=100$ and note that the σ is bounded implying the existence of a SPT phase. Motivated by the fact that SSH Hamiltonian encodes two distinct SPT phases, to detect the other SPT phase we compute the error correction statistics with respect to the reference state $|-_{[1,2]}, -_{[3,4]}, \dots, -_{[2N-1,2N]}\rangle$, the standard deviation of which is as in Fig. 7.7(b). From Figs. 7.7(a), (b) we have successfully established the fact that the Extended Bosonic SSH model encodes two distinct SPT phases.

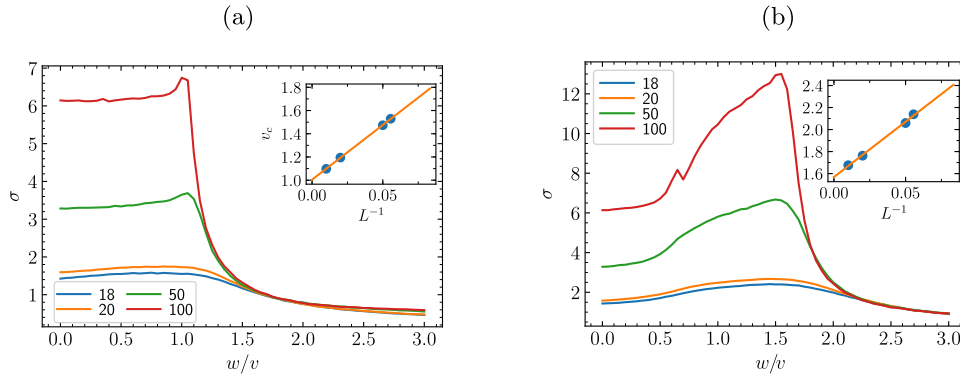


Figure 7.6: Standard deviation, σ , as a function of w/v at (a) $\delta = 0$ (b) $\delta = 3$ with the inset providing estimates for w^c (a) $w^c = 1.005(2)$ (b) $w^c = 1.57(1)$ with $v = 1$.

Anti-Ferromagnetic phase:

Having established the different SPT phases, we now consider the ground state of the anti-ferromagnet as the reference state. As established in the previous section, the error correction procedure involves the annihilation of the domain walls. Given that the presence of domain walls is identified by 1's, the error correction procedure in the excitation space involves identifying each domain wall with a walker which traverses the 1D ring which annihilates when one of the following condition is met:

1. It crosses the path of the another walker which is traversing the chain (or)

2. It crosses the boundary, the boundary is placed at one of the either ends and its state is left unknown, with no walker at the boundary

We apply the above error-correction procedures in the domain wall excitation space to reconfirm the presence of the anti-ferromagnetic phase as in Fig. 7.7(c). From Figs. 7.7(a), (b), (c) we conclude that the full phase diagram involves three distinct phases marked by the presence of two distinct SPT phases and an anti-ferromagnetic phase. The critical values in the full phase diagram in the thermodynamic limit being similar to critical values obtained from the three plots combined, for instance combining Figs. 7.7(a), (b), (c).

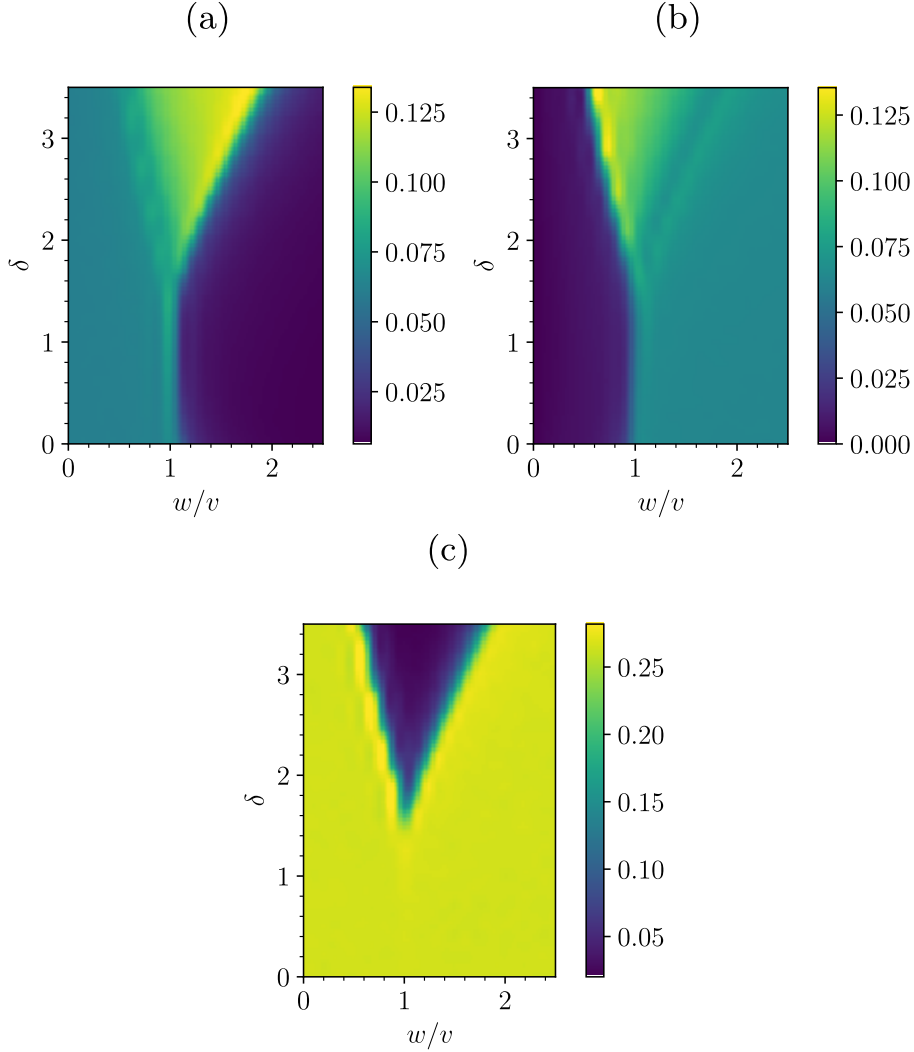


Figure 7.7: Standard deviation, σ , as a function of w/v and δ for a system size of $N=100$ spins. SPT phase with (a) $|-[_{[1,2N]}, -_{[2,3]}, \dots, -_{[2N-2, 2N-1]}]\rangle$ (b) $|-[_{[1,2]}, -_{[3,4]}, \dots, -_{[2N-1, 2N]}]\rangle$ as the reference state with error correction strategy involving both density and phase fluctuations capturing the phase transition between SPT phase (low σ) and anti-ferromagnetic/dual SPT phase (high σ). (c) Anti-ferromagnetic ground state in the excitation space as the reference state with error correction strategy involving domain walls capturing the phase transition between anti-ferromagnetic (low σ) and SPT phase (high σ).

Part V

Experimental realization via ultracold polar molecules

Chapter 8

Quantum simulation platform for topological phases based on ultracold polar molecules

In the previous chapters, having analyzed the nonequilibrium and dissipative quantum many-body phenomena mainly centered around the toric code models, in this chapter we discuss experimental ingredients which further aid in the realization of the above discussed phenomena [121, 122, 123, 62, 124, 125, 126]. To this extent, we consider setups involving ultracold polar molecules [127, 128, 129, 130, 131] along with atoms. As mentioned in Chap. 1, quantum phases are phases of matter at $T \rightarrow 0$, therefore ultracold regimes are a perfect platform hosting these phases. Polar molecules with their wide spectrum of properties which include additional rotational and vibrational degrees of freedom, strong electric dipole moment [132] among others have gained a lot of interest in the recent past. With additional rotational and vibrational degrees of freedom in comparison to their atomic counterparts and with efficient techniques to control these degrees of freedom gaining traction [133] polar molecules are an attractive platform to a wide range of applications ranging from tests of fundamental physics to the realization of many-body physics further to the understanding of chemical reactions [134, 135].

In this section, we mainly focus on the basic ingredients which include efficient detection and control of ultracold molecules, needed to realize the many-body dynamics of the toric code model as outlined in the Ref. [125]. In the above reference, the author has presented an architecture based on ultracold polar molecules to digitally simulate the coherent dynamics of the toric code Hamiltonian in addition to a dissipative protocol which results in

the ground state of the toric code. The digital simulation scheme involves a setup with a single control molecule surrounded by four molecules which realize the A_v, B_p interactions of the toric code. In the current scenario, we replace the control molecule with a control atom, as in Fig. 8.1(a). To realize the dynamics, we need to load the molecules around the control atom. In order to confirm the loading we need to detect the loaded molecules, to this extent we propose an efficient detection scheme which involves the imaging of the atoms. We note that the scheme proposed involves detection of single loaded molecule, and can be tailored for any other general scenario involving the detection of individual molecules. The direct imaging techniques used in the context of the atoms, are generally tailored for the detection of ensemble of molecules and are unreliable in the detection of single molecule. This is due to the fact that each molecule settles into a stable excited state after scattering only a single photon, thereby no longer scattering any photons of the imaging laser [133] required for the imaging process. Further to capture the evolution, we engineer a scheme to entangle the internal degrees of freedom of the atom and the molecule. Next, we introduce a protocol which involves the controlled dissipation of the internal states of the molecule aiding in the dissipative preparation of the toric code ground state. We develop these schemes which are favorable for bi-alkali molecules NaK [136, 137] and Na atoms. NaK molecules are chemically stable in the class of bi-alkali molecules, as most other molecules in the same class are difficult to prepare due to the inter-molecular collisions which result in an exothermic reaction [137]. We also note that the strategies proposed in this chapter are based on strong chemical reactions between the atom and the molecule resulting in a quantum Zeno based collisional blockade.

8.1 Detection of Molecules

We begin by discussing the strategies for the optimal detection of the molecules using atom as a probe. To effectively engineer the four body spin dynamics we need to position the molecules around a control atom. To this extent, we load the polar molecules around the atom as in Fig. 8.1(a). We assume that the lattice potentials can be tuned to strongly suppress the tunneling between the loaded molecular sites. For the purpose of detection, we consider the case where the atom can hop with hopping strength J , while the molecule remains stationary. The chemical reaction between the atom and the molecule introduces the dissipative element which induces a loss with a rate γ [135, 138]. With this setup as the basis, our goal is to efficiently probe the presence of the trapped molecule using the transfer dynamics of the atomic system.

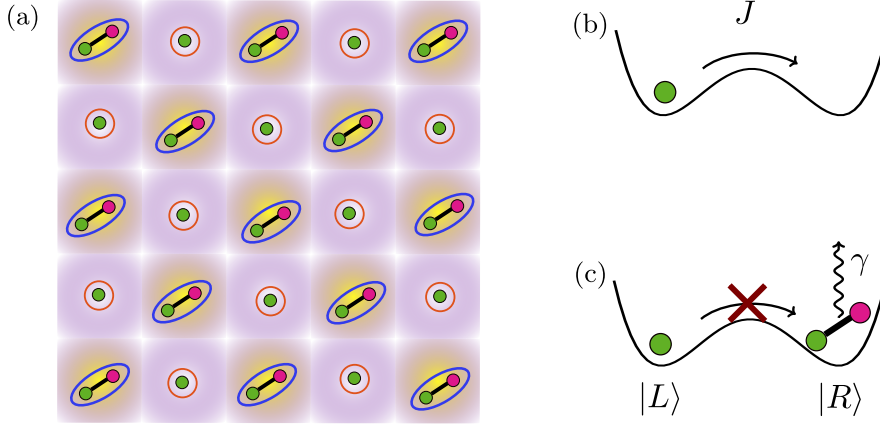


Figure 8.1: Quantum Zeno detection of molecules. (a) Single layer with control atoms surrounded by the molecule ensemble, with the control atoms used for the detection of molecules. (b) In the absence of molecules, the atoms can hop from $|L\rangle$ to $|R\rangle$. (c) The presence of molecules restricts the transfer to $|R\rangle$ due to the strong chemical reaction.

In the absence of the molecule, the dynamics of the atom, captured by the Landau-Zener process successfully transfers the atom which can be detected using quantum gas microscope techniques [139, 140]. On the other hand in the presence of molecule, in the limit where reaction rate becomes stronger than the tunneling, the system is frozen due to the strong chemical reaction between atom and molecule as in the quantum Zeno effect. That is, the coherent evolution of the atom given by the Landau-Zener transition in the absence of the molecule is suppressed in the presence of molecule due to dissipation induced by the strong chemical reactions between the atom and the molecule [141]. Therefore, imaging the atom after the transfer dynamics aids in the detection of the molecule. In order to efficiently detect the molecule, we need to minimize the loss due to the ineffective transfer dynamics of the atom as well as the loss due to the chemical reaction between the atom and the molecule. In the absence of molecule, the two-level atomic Hamiltonian reads as $H_0(t)$ as in Eq. 8.1 whose dynamics are captured by the Landau-Zener formula. While in the presence of molecule the dynamics of the atom are captured by the evolution of the Hamiltonian $H_0(t) + H_1$. The detuning $\Delta(t)$ is time dependent allowing the tunability of external field frequency in an experimental setup, with the intensity of the external field remaining a constant thereby setting the Rabi frequency $\Omega(t)$ to a constant Ω .

$$H_0(t) = \begin{bmatrix} -\Delta(t) & \Omega(t) \\ \Omega(t) & \Delta(t) \end{bmatrix}, H_1 = \begin{bmatrix} 0 & 0 \\ 0 & -i\gamma \end{bmatrix}. \quad (8.1)$$

The detection of trapped molecule by an atom can thus be casted as an optimization problem with the total error in detection given by Eq. 8.2

$$L(c_i, t_i, t_f) = P_0^{\gamma=0} + P_L \quad (8.2)$$

where $P_0^{\gamma=0}$ denotes the loss due to the ineffective transfer, P_L denotes the loss due to chemical reaction between the atom and the molecule, given by $[1 - (P_0^{\gamma \neq 0} + P_1^{\gamma \neq 0})]$, while c_i s being coefficients in $\Delta(t)$ which we fix to be an odd polynomial in t upto fifth order subject to the constraints that $\Delta(0) = 0$, $\Delta(\pm\infty) = \pm\infty$ with (t_i, t_f) being the time period of evolution with $t_f = -t_i$. Fig. 8.2(a) captures the individual losses with the time of evolution being optimal while Fig. 8.2(b) captures optimal $\Delta(t)$ and the error in detection given by $L(c_i, t_i)$. We note that for $\gamma = 50J$, we achieve high detection rates with a loss of around 3%. We arrive at the choice of $\gamma = 50J$ by observing the universal rate coefficient, β , of the chemical reaction between NaK and Na, which is on the order of $\beta = 1.47 \times 10^{-10} \text{cm}^3 \text{s}^{-1}$ [138], which in a potential well with an oscillator length, $a_0 = 100 \text{nm}$, results in a loss rate of $\gamma = 50 \text{kHz}$ [142] with the hopping matrix element J on the order of 100-1000 Hz.

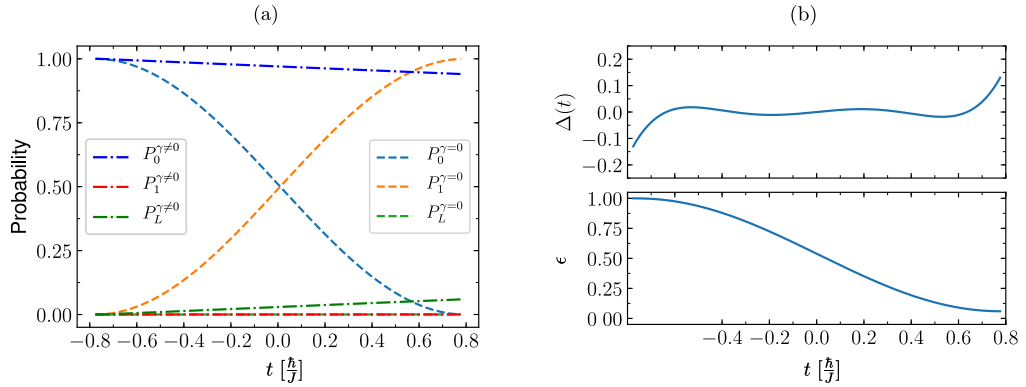


Figure 8.2: (a) Probability of atom in $|L\rangle$, $|R\rangle$, given by P_0 , P_1 and loss given by $P_L = 1 - (P_0 + P_1)$. In the absence of molecule in $|R\rangle$, $\gamma = 0$, the Hamiltonian H is Hermitian and leads to unitary evolution resulting in no loss. In the presence of molecule in $|R\rangle$, the Hamiltonian is non-Hermitian leading to a non-zero loss, P_L (b) Optimal $\Delta(t) = 0.09t - 0.94t^3 + 1.78t^5$ in units of J with optimal time $t_i = 0.78J^{-1}$. (Top) Objective error function $L(c_i, t_i)$ (Bottom) in the optimal time regime at $\gamma = 50J$.

8.2 Entangling Atom-Molecule interaction

Following the efficient detection of molecules, by introducing additional internal degrees of freedom we present a scheme to entangle these internal degrees. The entangling gate plays a major role in realizing the coherent dynamics of the toric code Hamiltonian which we shall present towards the end of the current section. The main idea behind entangling the internal states is to steer the internal state of the molecule via the atom. This would allow us to achieve control on manipulating the quantum states of the molecule by tuning the internal states of the atom. To realize these ideas, we extend the two well system to a three well system, with additional internal degrees of freedom for both atom and molecule as in Fig. 8.3.

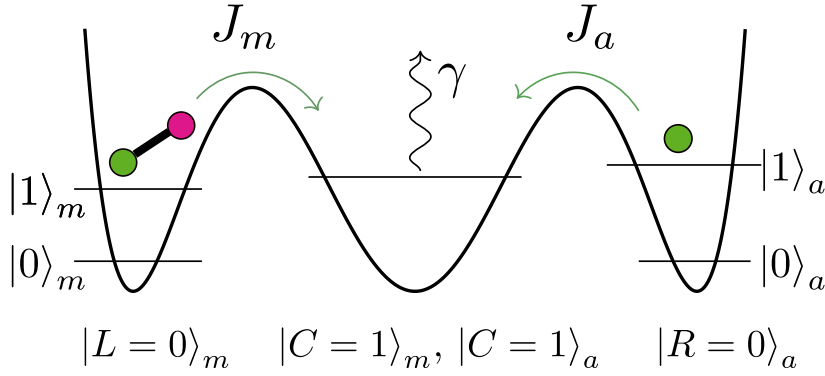


Figure 8.3: System used to entangle the internal states of atom and molecule. A single qubit denoted by $|i\rangle_{m(a)}$ is used to represent the internal states of the molecule (atom). One other qubit denoted by $|k\rangle_{m/a}$ ($k := L, C, R$) is used to represent the position of the molecule/atom. A total of four qubits, two each for the atom and molecule are required to describe the entire system.

The Hamiltonian of the above setup is given by

$$\begin{aligned}
 H = & B|1\rangle\langle 1|_m + E_{HFS}|1\rangle\langle 1|_a \\
 & + \Delta_m(t)|L\rangle\langle L|_m + \Delta_a(t)|R\rangle\langle R|_a \\
 & - \frac{i\gamma}{2}|C\rangle\langle C|_m \otimes |C\rangle\langle C|_a \\
 & - (J_m|1, L\rangle\langle 1, C|_m + J_a|1, R\rangle\langle 1, C|_a + \text{h.c})
 \end{aligned} \tag{8.3}$$

where B is the rotational constant of the molecule, E_{HFS} is the hyperfine splitting of the atom and $\Delta_{m/a}$ correspond to the electric and magnetic field

gradients, with the tunneling between the potential wells given by $J_{m,a}$. We assume $\Delta_m(t) = -\Delta_a(t) = \Delta(t)$ and the hopping strength to be identical i.e., $J_m = J_a = J$. We evolve the above system starting with the initial condition that the molecules occupies the $|L\rangle$ position while the atom occupies the $|R\rangle$ position (irrespective of the internal states). The central position is left vacant for the interaction of the atom and the molecule, with the tunneling to the central position being allowed only when the atom or molecule are excited. The direct hopping between the positions occupied by the atom and the molecule can be negated by shifting the central site (in the current context, the central site is shifted out of plane with respect to the Fig. 8.1). The evolution of Hamiltonian can be approximated to Controlled- Z (CZ) gate, as introduced in Chap. 6, with the atom as the control qubit and the molecule as the target qubit. The internal states of the atom and the molecule act as the computational states, thereby restricting the positional degrees of freedom of both atom and molecule to $|R\rangle$ and $|L\rangle$ respectively. Any occupation of the central well would lead to a chemical reaction resulting in a faulty CZ gate. We capture the quality of the gate using fidelity measures obtained by computing the overlap of the state evolved by the above Hamiltonian with the maximally entangled state given by $\frac{1}{\sqrt{2}}(|0000\rangle + |1010\rangle)$, where the odd qubits represent the internal states and the even qubits represent the position of the molecule and atom. Due to the tunable parameters, $\Delta(t), t_f$, the fidelity of the CZ gate can be optimized subject to the constraints that $\Delta(t)$ is an even function along with $t_i = -t_f$. We report a fidelity of 91.31% for the CZ gate as in Fig. 8.4 with the loss rate set to $\gamma = 50J$. Fig. 8.4 captures the relation between the gate error/detection error and the loss rate γ . We note that with increase in γ , the loss reduces as expected in the Zeno regime.

Following the Ref. [125], we extend the above ideas to simulate the coherent dynamics of the toric code Hamiltonian. We revisit the toric code Hamiltonian given by $H_{tc} = -\sum_v A_v - \sum_f B_f$ as introduced in Chap. 1, the evolution of which is given by $U = e^{-iH_{tc}t} = \prod_v \exp(iA_v t) \prod_f \exp(iB_f t)$. For a single timestep τ , the face f undergoes an evolution $\exp(iB_f \tau)$ which is given by a sequence of CZ and phase gates acting on the control atom and the target molecules surrounding the atom, as in Ref. [125]

$$\begin{aligned} U &= \exp(iB_f \tau) \\ &= U_{\pi/2}^a \prod_{e \in f} CZ^e U_{-\pi/2}^a U(\tau)^a U_{\pi/2}^a \prod_{e \in f} CZ^e U_{-\pi/2}^a \end{aligned} \quad (8.4)$$

where a denotes the qubit representing the internal state of the (control) atom, with $U(\tau)^a = \exp(i\tau\sigma_z^a)$, $U_{\pi/2}^a = \exp(i\sigma_y \pi/4)$, CZ^e is the controlled phase gate, the entangling gate established via the dynamics of the atom and molecule with the internal states of the atom and molecule as the control

8.3 Dissipative Quantum State Engineering

and target qubit respectively. Therefore, following the procedure as outlined in Ref. [125] and using the CZ gate obtained via the evolution of the atom and the molecule we have established a protocol to simulate the coherent dynamics of the toric code Hamiltonian.

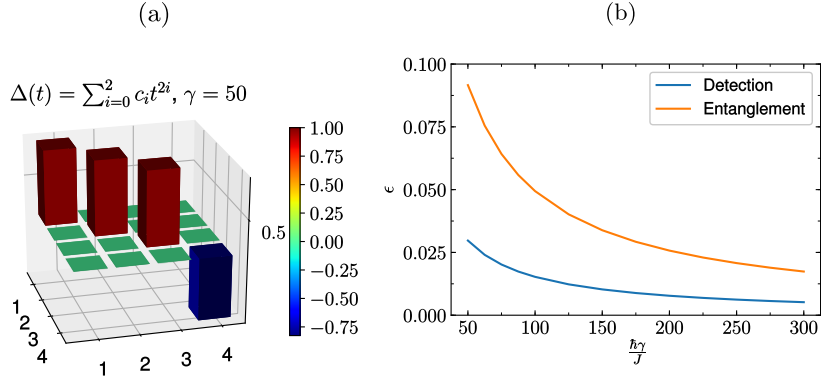


Figure 8.4: CZ gate (fidelity 91.31%) at $\gamma = 50J$ with $\Delta(t) = \sum_{i=0}^2 c_i t^{2i}$ in units of J , $J_m = J_a = 1J$ and $B = 0.5J$, $E_{HFS} = 0.75J$. In the zeno regime, as $\gamma \rightarrow \infty$ both the detection errors and entangling gate errors vanish.

8.3 Dissipative Quantum State Engineering

We extend the entangling CZ gate developed in the earlier section towards controlled dissipation of the internal states of the molecule. To this extent, we introduce two strategies: one, which involves a pulsed sequence realizing a SWAP gate which swaps the internal states of atom and molecule while leaving the state $|0_m 0_a\rangle$ invariant, followed by dissipatively pumping the atom to $|0\rangle_a$. The other strategy is to continuously drive both the molecular and atomic transitions by engineering suitable collapse operators and evolving the open system according to Lindbladian dynamics.

8.3.1 Dissipative Engineering via pulsed sequences

In this section, we construct a SWAP gate, which aims at swapping the internal states of the molecule and atom. The atom-controlled coherent driving in conjugation with the dissipative pumping of the atom to state $|0_a\rangle$ realizes the controlled dissipation of the internal states of the molecule. The quantum circuit, denoted by U , as in Fig. 8.5 performs the SWAP using only

single qubit gates and CZ gates, simultaneously leaving the state $|0\rangle_m|0\rangle_a$ invariant.

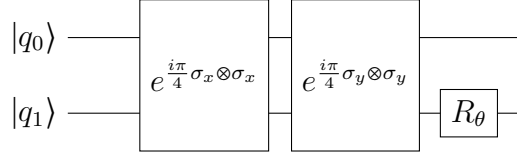


Figure 8.5: Quantum circuit which swaps the internal states of molecule and atom denoted by $|q_0\rangle, |q_1\rangle$ simultaneously leaving the state $|0_m 0_a\rangle$ invariant. The two qubit gates can be decomposed into single qubit gates and a CZ gate.

The unitary, U , is given by

$$U = R_{-\pi/2}^2 T_2 T_1 \quad (8.5)$$

where R_θ^j is the phase shift gate acting on the j^{th} qubit with T_1, T_2 given by

$$\begin{aligned} T_1 &= e^{\frac{i\pi}{4} \sigma_x \otimes \sigma_x} \\ T_2 &= e^{\frac{i\pi}{4} \sigma_y \otimes \sigma_y} \end{aligned} \quad (8.6)$$

The decomposition of the above unitaries in terms of single qubit gates and CZ gate, equivalent upto a global phase, is as follows

$$\begin{aligned} T_1 &= (H^1 \otimes H^2)(CZ)(R_{-\pi/2}^1 \otimes R_{-\pi/2}^2)(H^1 \otimes H^2) \\ T_2 &= (G^1 \otimes G^2)(Z \otimes Z)(T_1)(G^1 \otimes G^2) \end{aligned} \quad (8.7)$$

where $H = \frac{1}{\sqrt{2}} \begin{bmatrix} 1 & 1 \\ 1 & -1 \end{bmatrix}$ denotes the Hadamard gate, Z denotes the Pauli- Z , given by $\begin{bmatrix} 1 & 0 \\ 0 & -1 \end{bmatrix}$ gate with $G = e^{-\frac{i\pi}{4} \sigma_z}$. Under the assumption that the single qubit operations are perfect, the efficiency of the molecular dissipation is directly connected to the fidelity of the transformation U capturing the swap, which is directly proportional to the fidelity of the entangling CZ gate. We capture, in Table. 8.1, the fidelity of the U gate at different γ given by U_γ , by computing $|\langle 01|U_\gamma|10\rangle|^2$ and $|\langle 00|U_\gamma|00\rangle|^2$, giving the fidelity of the underlying CZ gate as the reference.

Having introduced dissipative techniques, we follow the Ref. [125] and prepare the ground state of the toric code by incoherent dynamics, that is

8.3 Dissipative Quantum State Engineering

γ	CZ Fidelity	$ \langle 01 U_\gamma 10\rangle ^2$	$ \langle 00 U_\gamma 00\rangle ^2$
100	94.6	89.6	89.0
150	96.3	92.8	92.5
200	97.2	94.5	94.3
250	97.7	95.5	95.4
∞	100	100.0	100

Table 8.1: Table capturing the fidelity of the transformation, U , at different γ , given by U_γ , with reference to the fidelity of CZ gate which is central to U .

we introduce dissipative operations which cool a product state to the ground state of the toric code. Motivated by the fact that the excitations in the toric code model are identified at the centers of the vertices/faces, we encode the information of the whether an vertex/face is excited in the control atom, the presence (absence) of the excitation is identified by $|1_a\rangle(|0_a\rangle)$ and therefore dissipatively pump the atom to $|0_a\rangle$ if an excitation is present. To map the state of a vertex/face we use the following unitary sequence

$$U_m = \text{CNOT}_i U_{\pi/2}^a CZ^a U_{\pi/2}^c \quad (8.8)$$

where CNOT_i is the Controlled-NOT gate introduced in Chap. 3. with the internal states of the atom and molecule acting as the control and target qubit. The unitaries in U_m can be expressed using single qubit gate operations and the CZ gate engineered in the previous section. As in the previous section, we perform the unitary U_m sequentially over all the edges which define a vertex/face and this operation leaves the control qubit in $|0\rangle$ if there are no excitations while flips it to $|1\rangle$ in the presence of excitations. In the latter, the internal state of the atom can then be dissipatively pumped to $|0\rangle_a$ to cool the system to the ground state of the toric code Hamiltonian. In general, the unitary followed by dissipation can be described by the discrete Lindblad master equation as introduced in Chap. 6 with the collapse operators given by $c_p^i = \sigma_x^i(1 - B_p)$, $c_v^j = \sigma_x^j(1 - A_v)$, as introduced earlier in Chaps. 5 and 6.

8.3.2 Dissipative Engineering via Lindbladian dynamics

In this section, instead of the pulse sequence we introduce a strategy based on continuous driving of both atom and the molecular transitions. The CZ

gate introduced earlier effectively realizes a $\sigma_z\sigma_z$ interaction on the internal states of the atom and molecule with no possibility for energy transfer. By considering the rotation frame of reference, the above interaction translates to a $\sigma_x\sigma_x$ interaction thereby facilitating energy transfer. This energy transfer can be further made efficient by tuning the detuning and Rabi frequency of the individual driving. We analyze the proposed strategy by replacing the non-Hermitian dynamics by Lindbladian dynamics with the interaction captured by the coherent evolution of the Hamiltonian given by

$$\begin{aligned}
 H = & -J(|1, L\rangle\langle 1, C|_m + |1, R\rangle\langle 1, C|_a + \text{h.c}) \\
 & + \Omega(\sigma_x^{(m)} + \sigma_x^{(a)}) + \delta(\sigma_z^{(m)} + \sigma_z^{(a)}) \\
 & - \Delta|L\rangle\langle L| - \Delta|R\rangle\langle R|
 \end{aligned} \tag{8.9}$$

where Ω , δ are the Rabi frequency and detuning used for the driving of the molecule and the atom. We introduce collapse operators which capture the optimal pumping of the atom, $c_\kappa = \sqrt{\kappa}\sigma_-$ from the excited to ground state. In addition, the chemical reaction between the atom and molecule in the central well is captured by $c_\gamma = \sqrt{\gamma} \sum_{\lambda_1, \lambda_2} |\text{sink}\rangle\langle \lambda_1^m C \lambda_2^a C|$, where $|\text{sink}\rangle$ is an additional state accounting for the loss of atom and molecule. Having defined the Hamiltonian and the dissipative collapse operators, the dynamics realizing the state engineering is described by the Lindblad master equation as introduced in Chap. 5, Eq. 5.8. We optimize the parameter set $(\Omega, \delta, \Delta, \kappa)$ such that the initial state $|1\rangle_m|0\rangle_a$ maps to $|0\rangle_m|0\rangle_a$. In Fig. 8.6, we plot the probability of the molecule in $|0\rangle$ and $|1\rangle$, with the former increasing and the latter decreasing we show that the internal state of the molecule dissipates with high probability with the loss due to the chemical reaction remaining low.

To summarize, we have presented a complete simulation toolbox which includes detection of molecules, entangling the internal states of the molecule to an atom, along with dissipative state preparation techniques involving the internal degrees of freedom of the molecules. In addition, we have also presented these schemes tailored to simulate the dynamics of the toric code Hamiltonian as well prepare its ground state by dissipative cooling. These techniques can be further extended to encode the tailored dissipation introduced in Chap. 5 and also the nonequilibrium phenomena introduced in Chap. 6, thereby facilitating the detection of various quantum phase transitions involving topological phases.

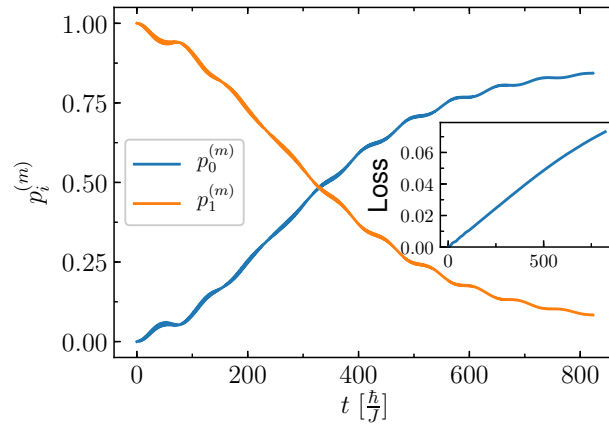


Figure 8.6: The probability of molecule in the excited state $|1\rangle$, $p_1^{(m)}$ closely follows an exponential decay, while the ground state probability $p_0^{(m)}$ increases in a similar way (Inset) The loss due to the chemical reaction with $\gamma = 50J$ which remains low. The optimal parameters are given by $\kappa = 0.007J$, $\Omega = 0.045J$, $\delta = 1.198J$, $\Delta = 1.903J$, with optimal time of evolution as $t_f = 822.95J^{-1}$.

Part VI
Conclusion

Chapter 9

Summary and outlook

To summarize, we have analyzed phase transitions involving topological phases in the context of closed and open environment. The main focus has been to analyze and introduce various signatures capable of detecting topological phases defined on a manifold supporting open boundaries.

While the robustness of topologically ordered states under perturbation on a periodic manifold has been well understood, the introduction of open boundaries which support exotic phenomenon such as anyon condensation has remained unexplored. The understanding of these open boundaries are of much significance as they not only facilitate efficient storing of quantum information but also are more viable to realize experimentally[143, 62, 125, 63]. In Part II, we widely focused on the analysis of phase transitions in closed systems which exhibit topological order defined on a manifold supporting open boundaries in the presence of various perturbations. In Chap. 3, we analyzed the robustness of topological order of the toric code defined a cylinder, sporting identical boundary conditions on either of its boundaries, in the presence of various external magnetic fields. We classified the perturbed models into non-condensing and condensing classes by observing the behavior of excitations. We arrived at the conclusion that non-condensing classes are more robust candidates to store a single logical qubit in comparison to the periodic boundary counterpart. We then analyzed the condensing class by studying various signatures like gap opening in the ground state manifold, TEE and concluded that the topological phase is trivial as soon as the perturbation is turned on. Having established the above result, we then benchmarked MES based method leading to the notion that MES are quantitatively ineffective in precisely capturing the critical strength. In Chap. 4, we analyzed the sensitivity of topological order with respect to the manifold on which the Hamiltonian is defined. Using Hamiltonian interpolation, we

interpolated between different boundary conditions thereby detecting various topological to topological phase transitions (TTPTs). TEE which was an effective signature previously remained insensitive to the change in the boundary conditions and therefore we introduced the notion of open loop operator whose expectation value effectively captures the phase transition.

It would be interesting to study the above introduced phase transitions in a dynamical setting with the perturbation inducing a sudden quench on the ground of the toric code [57, 144]. For example, it would be interesting to study the Loschmidt echo as the unperturbed Hamiltonian is quenched both across a topological-trivial phase transition as well as a topological-topological phase transition [145, 146]. Also, with the excitations being particle like it would be interesting to study the Kibble-Zurek mechanism which relates the density of excitations to the rate of quench when quenched across the transition to uncover possible universality classes [147, 148]. The notion of time crystals has gained importance in the recent times, where the order parameter of a periodically driven Hamiltonian shares a different period with respect to the period of the Hamiltonian [149]. Though the notion of topologically ordered time crystals has been hinted at in Ref. [150] it would be interesting to investigate the same with the boundaries being periodically modulated.

In Part. III, we discussed the notion of topological phase transitions in various open quantum setups. In Chap. 5, motivated by TTPT's of Chap. 4, we introduced dissipative collapse operators whose effective rates are controlled by an interpolation parameter. The collapse operators cool the product state to distinct topologically ordered states at either end of the interpolation thereby resulting in a TTPT. Established signatures being inconsistent in detecting topological order across varied scenarios and also with the notion of topological order for mixed states being elusive, in Part III, we propose an operational definition for topological order. The above definition not only enables the detection of novel topological phases but also provides a unified framework to quantify topologically ordered states across various scenarios. In Chap. 6, we successfully verify the above definition by mapping and comparing the criticality of a perturbed minimal instance toric code to that of an 1D Ising chain. Further, we introduce topologically ordered states in an open system by engineering suitable collapse operators to mimic the 1D Directed Percolation and 2D Branching Annihilating Random Walks nonequilibrium phenomena. The phase transitions in these systems are parameterized by the heating rate which when low cools the system to a topologically ordered state while higher heating rates drive it into a topologically trivial state.

In Part. IV, we extend the operational definition to SPT phases by studying two variants of the SSH model. To this extent, we compute the ground

state using tensor network algorithms and via measurements which are simulated using Monte-Carlo sampling we compute the error correction time statistics. A key difference between the operational definition introduced for intrinsic topological order and the current case of SPT lies in the fact that in the former there were no symmetry constraints on the error correction strategy while in the latter we impose additional constraints.

With quantum phase transitions being analyzed from quantum information viewpoint, it would be interesting to further probe the fundamental question on whether error correction strategies can detect different phases and their associated phase transitions, not being restricted to the case of topologically ordered phases. From the topological order viewpoint, we have used the depth of the detection circuits for classification of phases with the correction time being instantaneous, the statistics of number of unitaries required to correct the error might also be an interesting parameter capturing the phase transition [151]. Establishing the correspondence with nonequilibrium phenomenon opens up a lot of avenues to discover topological phases in an open setting, for example: one interesting direction would be to explore whether cellular automaton rules can generate topological phases and the possibility of construction of a quantum version of a cellular automaton. In addition, in a dynamical setting it would be interesting to study the possibility of realizing topological time crystals in an open setting [152] by modulating the dissipative rates in a periodic fashion. Some of the immediate directions would be to analyze various entanglement signatures of these mixed topologically ordered states. With the recent advancement in both numerical and experimental techniques, optimal state preparation using variational circuits has gained traction [153]. It would be interesting to pursue the preparation of mixed states and also detect the phase transitions by computing the complexity, based on the depth of the variational circuits. On similar lines, on a numerical front with the advancement in machine learning algorithms and their applications to state preparation and phase detection [154, 155, 156], it would be interesting to study the closed and open setup phase transitions introduced in this work using these techniques. With the notion of topological order in 3D captured by various fracton models [157, 158], it would be interesting to extend the operational definition to not only compute the robustness of these phases in a closed setting [159] but also to analyze these phases in an open setting with an aim to store robust quantum memories. One other important direction would be pursue the notion of open boundaries both in 2D and 3D topologically ordered systems to gain further insight into distinct topological phases which act as a testbed for storing logical qubits thereby providing platforms for topological quantum computation.

In part V, with ultra cold molecules as the basic ingredients we propose strategies which would further aid in the realization of the quantum many-body phenomena as discussed above. To this extent, we have presented an optimal strategy for the efficient detection of molecules using atoms as a probe. Further, by extending the internal degrees of both atoms and molecules we have presented a strategy to entangle them, thereby providing a means to control the molecule using the atom. Finally, we present two strategies for dissipative state engineering of the molecular internal states, one involving a pulsed sequence which swaps the internal states of atom and molecule in conjugation with optical pumping of the atomic state. The other strategy centered around engineering suitable collapse operators to efficiently dissipate the internal states of the molecule.

Part VII
Appendices

Appendix A

Condensation at the boundary of the quantum double

We cite the main results of Ref. [40] which provide a recipe to compute the condensation properties of the excitations obtained by the inner product of characters related to the irreps of excitations and the corresponding boundary. As introduced in the Chap. 2, the boundaries of a quantum double $D(G)$ are characterized by the subgroup of $K \subseteq G$ along with a 2-cocycle of K , $H^2(K, \mathbb{C})$. The excitations are identified by the irreps, π , of the centralizers of the conjugacy class, \bar{a} , of G , denoted by the pair (\bar{a}, π) . Let us denote the character of the irreps by $\chi_{(\bar{a}, \pi)}$ which is given by

$$\chi_{(\bar{a}, \pi)}(gh^*) = \delta_{h \in \bar{a}} \delta_{gh, hg} \text{tr}_\pi(k_h^{-1} g k_h) \quad (\text{A.1})$$

We define the modular S -matrix whose rows and columns are indexed by irreps of $D(G)$ which provide insight into the braiding statistics

$$S_{(\bar{a}, \pi)(\bar{a}', \pi')} = \frac{1}{|Z(a)| \cdot |Z(a')|} \sum_{h: ha'h^{-1} \in Z(a)} \text{tr}_\pi(ha'^{-1}h^{-1}) \text{tr}_{\pi'}(h^{-1}a^{-1}h) \quad (\text{A.2})$$

The fusion rules between (\bar{a}, π) and (\bar{a}', π') are given by

$$(\bar{a}, \pi) \otimes (\bar{a}', \pi') \simeq \bigoplus_{\bar{h}, \rho} N_{(\bar{a}, \pi)(\bar{a}', \pi')}^{(\bar{h}, \rho)} (\bar{h}, \rho) \quad (\text{A.3})$$

where (\bar{h}, ρ) denote excitations of the fusion outcome.

In the above, N_{XY}^Z is given as follows

$$N_{XY}^Z = \sum_U \frac{S_{XU} S_{YU} S_{ZU}^*}{S_{0U}} \quad (\text{A.4})$$

where $\mathbf{0} = (\bar{e}, 1)$ is the trivial representation.

Given that the boundary is decorated by subgroup $K \subseteq G$ along with a trivial 2-cocycle, the associated character with respect to the boundary, $\chi_{A(K)}(hg^*)$, where the irrep $A(K)$ is as defined in Ref. [40], is given by

$$\chi_{A(K)}(hg^*) = \frac{1}{|K|} \delta_{gh,hg} \sum_{x \in G} \delta_{xhx^{-1} \in K} \delta_{xhx^{-1} \in K} \quad (\text{A.5})$$

The inner product between characters χ_1, χ_2 is given by

$$\langle \chi_1, \chi_2 \rangle = \frac{1}{|G|} \sum_{g,h} (\chi_1(gh^*)) \chi_2(gh^*) \quad (\text{A.6})$$

An anyon indexed by (\bar{a}, π) condenses on a boundary decorated by elements of K , if

$$\langle \chi_{A(K)}, \chi_{(\bar{a}, \pi)} \rangle > 0 \quad (\text{A.7})$$

If in the above, the 2-cocycle is non-trivial, say φ , then the character associated with the boundary, $\chi_{A(K, \varphi)}$ is given by

$$\chi_{A(K, \varphi)}(gh^*) = \frac{1}{|K|} \delta_{gh,hg} \sum_{x \in G} \delta_{xgx^{-1} \in K} \delta_{xhx^{-1} \in K} \varphi(xgx^{-1} | xhx^{-1}) \quad (\text{A.8})$$

where $\varphi(k|l) = \varphi(k, l) \varphi(klk^{-1}, k)^{-1}$.

Appendix B

CNOT mechanism in the context of open boundaries

We present the CNOT mechanism which maps the Hamiltonian H_{grpx} to the equivalent Ising picture along with the topological spins and vacancy. This section heavily relies on the derivation mentioned in Ref. [64, 160]. We begin by defining the CNOT operation which involves a control (c) qubit and a target (t) qubit and is given by

$$\text{CNOT}_{c\otimes t} = |0\rangle\langle 0| \otimes \mathbb{1} + |1\rangle\langle 1| \otimes \sigma_x \quad (\text{B.1})$$

From the above it is clear that given the control qubit is $|0\rangle$, the target qubit remains invariant while if it is $|1\rangle$, the target qubit is flipped by the action of σ_x . We note the following relations involving CNOT's

$$\begin{aligned} \text{CNOT}(\mathbb{1} \otimes \sigma_z)\text{CNOT} &= \sigma_z \otimes \sigma_z \\ \text{CNOT}(\sigma_z \otimes \mathbb{1})\text{CNOT} &= \sigma_z \otimes \mathbb{1} \\ \text{CNOT}(\sigma_x \otimes \mathbb{1})\text{CNOT} &= \sigma_x \otimes \sigma_x \\ \text{CNOT}(\mathbb{1} \otimes \sigma_x)\text{CNOT} &= \mathbb{1} \otimes \sigma_x \end{aligned} \quad (\text{B.2})$$

New faces/vertices can either be added or existing faces/vertices can be shrunk by the application of the CNOTs. We shall present both the techniques where additional (existing) qubits can be induced (expelled) thereby leading to the increase (decrease) of the A_v, B_p operators. Following Ref. [160], consider the ground state of the toric code $|\psi_{tc}\rangle$, and consider a face as in Fig. B.1. Initially the purple spin, $|0\rangle_p$, is attached to the lattice at a singular point, it forms a face by itself. To integrate this new spin we begin by applying a CNOT

$$\begin{aligned} \text{CNOT}_{14}(|\psi_{tc}\rangle \otimes |0\rangle_p^4) &= \text{CNOT}(\mathbb{1} \otimes \sigma_z^4)(|\psi_{tc}\rangle \otimes |0\rangle_p^4) \\ &= (\sigma_z^1 \otimes \sigma_z^4)\text{CNOT}(|\psi_{tc}\rangle \otimes |0\rangle_p^4) \end{aligned} \quad (\text{B.3})$$

B. CNOT mechanism in the context of open boundaries

The successive application proceeds as in Fig. B.1 leading to the splitting of a single face into two faces

$$\text{CNOT}_{34}\text{CNOT}_{24}\text{CNOT}_{14}(|\psi_{tc}\rangle \otimes |0\rangle_p^4) = (\sigma_z^{123} \otimes \sigma_z^4)\text{CNOT}_{321,4}(|\psi_{tc} \otimes |0\rangle_p\rangle) \quad (\text{B.4})$$

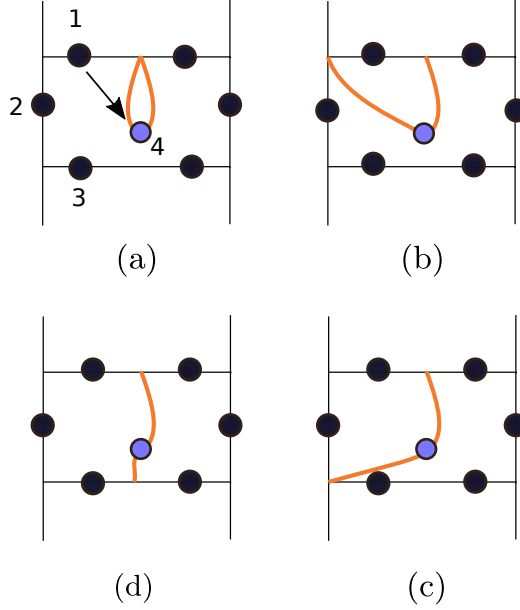


Figure B.1: The purple spin in $|0\rangle$ is being added to create two faces from a single face. The action of CNOT on qubits (a) 1_c and 4_t (b) 2_c and 4_t (c) 3_c and 4_t

As CNOT is a unitary, the above procedure is reversible, that is it is possible to shrink the existing faces by the action of CNOT. Consider the action of CNOT on $|\psi_{tc}\rangle$, for the removal we have

$$\begin{aligned} \text{CNOT}(|\psi_{tc}\rangle) &= \text{CNOT}(\sigma_z^1 \otimes \sigma_z^4)|\psi_{tc}\rangle \\ &= (\mathbf{1} \otimes \sigma_z^4)\text{CNOT}(|\psi_{tc} \otimes |0\rangle_p^4\rangle) \end{aligned} \quad (\text{B.5})$$

Here we have discussed the extension(shrinking) of the faces, similar techniques can be applied for the vertices. We now extend this to the case of H_{grpx} closely following the Ref. [64]. In the above, the authors have introduced the CNOT map as reorienting the edges of the target qubits, implying a shrink in the B_p operators by applying consecutive CNOTs until each physical spin is an independent face all by itself. As each spin forms an independent face, the Hamiltonian reduces to $\sum_p \mu_p^z$ along with a vacancy

and additional topological spins. In the thermodynamic limit, these additional features can be ignored as these are sub-leading. The ground state of the toric code thus maps to the paramagnet in the approximated Ising equivalent. In the presence of perturbation, we note that as the CNOT is performed the perturbation spreads leading to nearest neighbor interaction, thereby the perturbed toric code model is approximated by the transverse field Ising model.

B. CNOT mechanism in the context of open boundaries

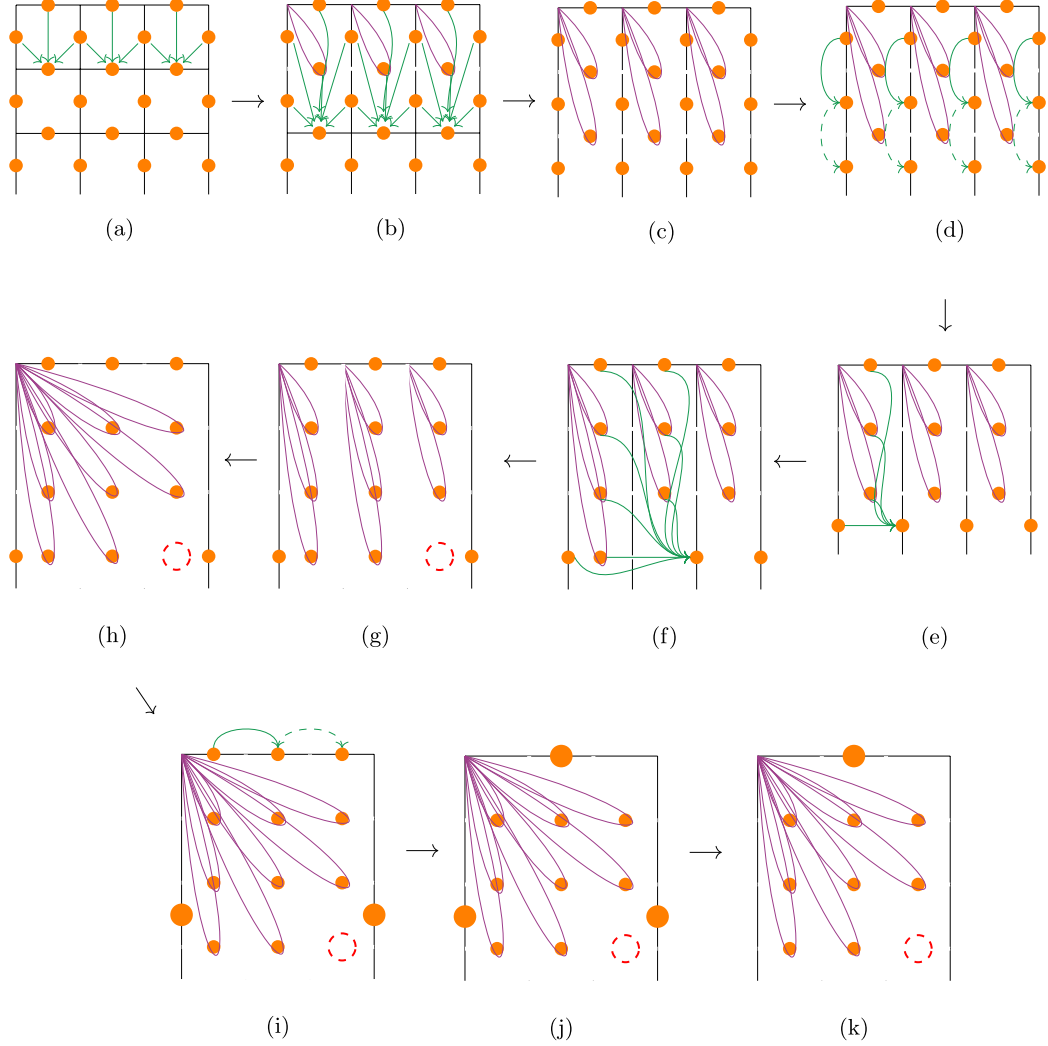


Figure B.2: Ising map along with the topological spins (denoted by large orange dots) and the vacancy (denoted by dashed red circle) for Hamiltonian H_{grpx} . The difference between the map in the periodic case and the open boundary case arises in (f), where the last rung is retained because of the boundary. Step (j) is equivalent to (k) since the action of two vertical non-trivial loop operators (homotopic loop operators) on the system have no effective action, $L_{topological}^2 = \mathbb{I}$, where $L_{topological}$ is the non-trivial loop operator in the vertical direction. Thereby the only loop operator remaining is in the horizontal direction connecting both the boundaries as indicated in (k). The topological spin in the horizontal direction couples the Ising spins on either side of the shorter boundary.

Appendix C

Error-Correction Statistics for 1D Ising chain

We present the error correction time statistics of the perturbed ground state of the transverse field Ising model with the perturbation strength on the nearest neighbor for a system size of $N = 24$. The spread in the statistics implies an increase in time to correct the errors.

C. Error-Correction Statistics for 1D Ising chain

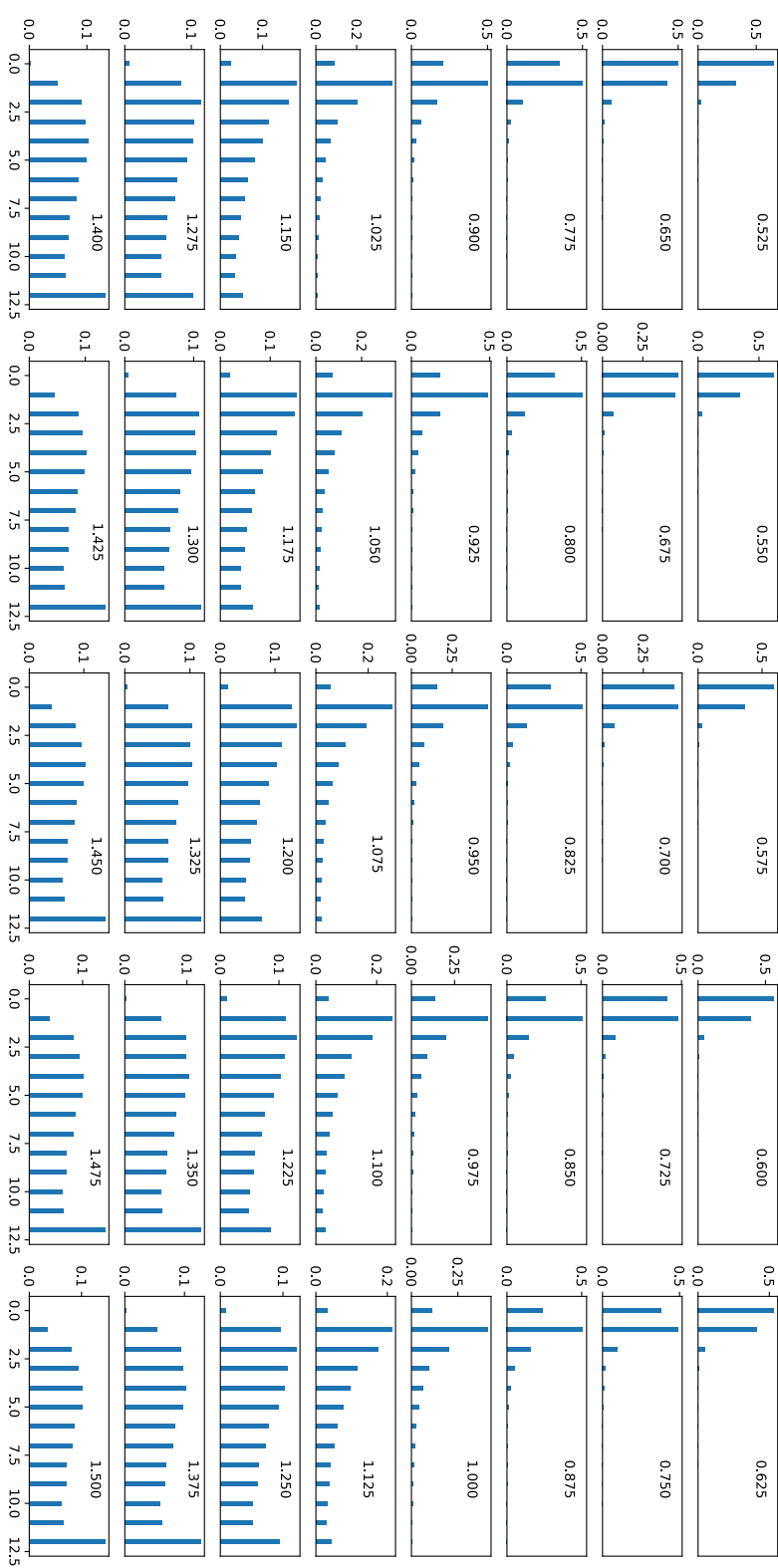


Figure C.1: The error correction time statistics for a system size of $N = 24$ with the perturbation strength at the top right corner of each subplot. We note that with increase in perturbation strength we are more likely to see states with higher correction times.

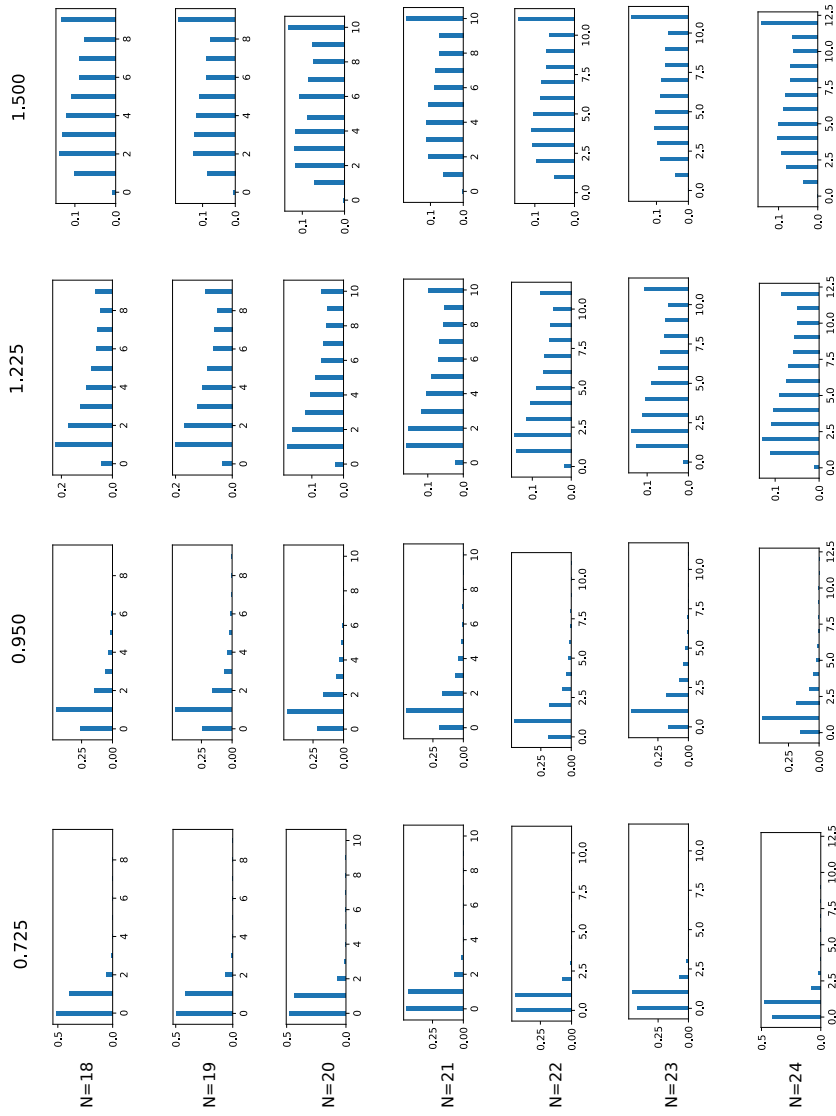


Figure C.2: Scaling of the error correction statistics for different system sizes at perturbation strengths given by 0.725, 0.950, 1.225, 1.500.

Appendix D

Monte-Carlo simulation of classical master equation

We sketch the steps behind the Monte-Carlo simulations involving the dissipative collapse operators which encode the rules of 1D DP and 2D BARW. We consider the collapse operators in the Ising basis (excitation basis) which are of the form

$$C_n = \frac{\sqrt{\gamma}}{2} P(\mu^x) (1 - \mu_p^z) \quad (\text{D.1})$$

where $P(\mu^x) = \prod_{p_j} \mu_{p_j}^x$, with the effective Hamiltonian for evolution given by, as in Eq. D.2,

$$H_{\text{eff}} = H_c - \frac{i}{2} \sum_n C_n^\dagger C_n \quad (\text{D.2})$$

We consider pure dissipative setups, i.e., $H_c = 0$. The MCWF method used to compute the steady state has the following procedure for a single trajectory, as in Ref. [85], where the steady state itself is obtained by averaging the evolved state over many trajectories

1. Choose a random number, r , between 0 and 1 representing the probability of the occurrence of a quantum jump
2. Evolve the system using the above introduced effective Hamiltonian upto a time t_j such that $\langle \psi_{t_j} | \psi_{t_j} \rangle = r$ at which the jump occurs
3. Choose the collapse operator, C_i , such that $P_i \geq r$ with

$$P_i = \sum_{k=1}^i \langle \psi(t_j) | C_k^\dagger C_k | \psi(t_j) \rangle / \delta p, \text{ where } \delta p = \sum_n \langle \psi(t_j) | C_n^\dagger C_n | \psi(t_j) \rangle$$

In this particular scenario due to the structure of the collapse operators it is possible to compute the time at which jump occurs analytically. The key ingredients for the MCWF method are as follows:

D. Monte-Carlo simulation of classical master equation

- $C_n^\dagger C_n = \frac{\gamma}{2}(\mathbb{1} - \mu_p^z)$
- $\delta p_n = \langle \psi(t) | C_n^\dagger C_n | \psi(t) \rangle = \delta_{n,1} \gamma_n$ for n^{th} qubit in $|\psi(t)\rangle$.

As per step. 2 above, we evolve the Schrödinger equation with H_{eff} introduced earlier

$$\begin{aligned}
 |\psi(t)\rangle &= e^{-iH_{\text{eff}}t} |\psi(0)\rangle \\
 &= e^{-\frac{t}{2} \sum_n C_n^\dagger C_n} |\psi(0)\rangle \\
 &= e^{-\frac{\gamma t}{2} \sum_i \frac{1-\mu_i^z}{2}} |\psi(0)\rangle \\
 &= e^{-\frac{\gamma_{\text{eff}} t}{2}} |\psi(0)\rangle
 \end{aligned} \tag{D.3}$$

where $\gamma_{\text{eff}} = \sum_i \delta_{i,1} \gamma_i$ for i in $|\psi(0)\rangle$.

We compute the inner product

$$\begin{aligned}
 \langle \psi(t_j) | \psi(t_j) \rangle &= e^{-\gamma_{\text{eff}} t_j} \\
 r &= e^{-\gamma_{\text{eff}} t_j} \\
 t_j &= -\frac{\log(r)}{\gamma_{\text{eff}}}
 \end{aligned} \tag{D.4}$$

Appendix E

Extension of operational definition for fracton order

In this appendix, we discuss the possible extensions of the operational definition to the case of fracton topological order. These phases of matter are beyond the conventional paradigm of topological orders with their classification currently being actively pursued. For our current discussion, we consider lattice spin systems in 3D exhibiting such orders. Broadly, these phases of matter are classified into type-I and type-II fracton orders. We consider the X-Cube model and Cubic code model which are paradigmatic models exhibiting the above orders. We also note that we closely follow the Ref. [159] in the construction of these models.

E.1 X-cube model

We consider a 3D cubic lattice with spin-1/2's on the edges of the lattice. The Hamiltonian is given by

$$H_{xc} = - \sum_v A_v - \sum_p B_p \quad (\text{E.1})$$

where $A_v = A_v^{xy} + A_v^{yz} + A_v^{zx}$ with $A_v^k = \prod_{i=1}^4 \sigma_x^i$ as defined in Fig. E.1. $B_p = \prod_k \sigma_z^k$ where k belongs to the edges of the cube. The ground state is given by

$$|\psi\rangle_{xc} = \mathcal{N} \prod_{v,k} (\mathbb{1} + A_v^k) |\mathbf{0}\rangle, \quad \text{for } k \in \{xy, yz, zx\} \quad (\text{E.2})$$

with the ground state degeneracy given by 2^{6L-3} defined on a $L \times L \times L$ cube placed on a 3-torus.

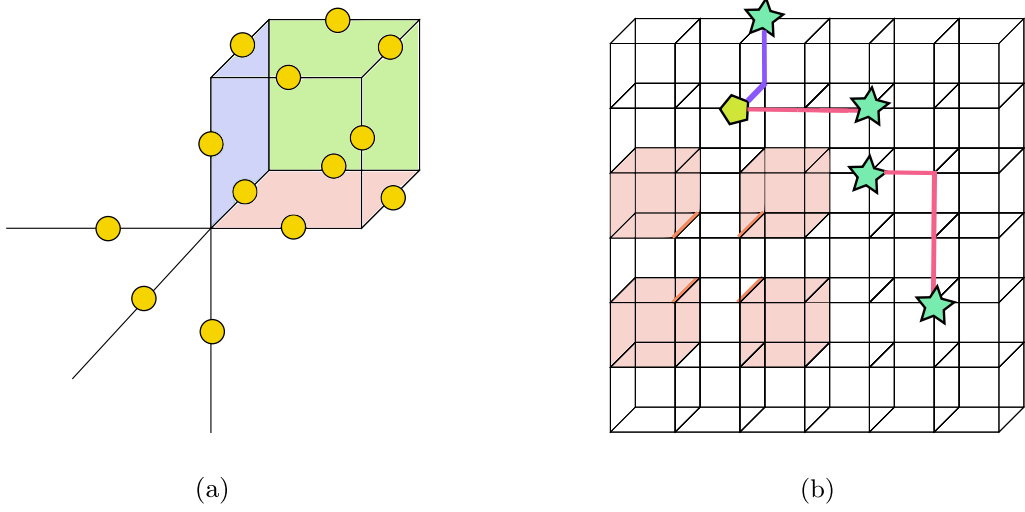


Figure E.1: (a) A_v operator is given by the sum of A_v^k 's in each plane, while B_p is defined on the 12 edges that define the cube. (b) Excitations in the system consist of B_p violations (denoted by colored cubes) which appear four at a time while A_v excitations in the same plane appear as pairs (denoted by stars) while moving them across planes i.e., by taking a turn results in an additional excitation (denoted by pentagon) at the bend.

The excitations in the system are given by the action of anti-commutators σ_z and σ_x which anti-commute with A_v and B_p operators respectively. While A_v violations, which are identified at the vertices, when in plane appear in pairs but when moved in/out of plane additional excitations appear at the bent vertex which can be derived from the A_v structure. B_p excitations identified at the center of the cubes appear four at a time as a single edge is shared between four cubes. These models under perturbation can be mapped to Ising models in 3D as in Ref. [159], with the Ising spins sitting at the either the vertices or at the center of the 3D faces or both, depending on the perturbation. The operational definition of topological order can be extended to effectively detect fracton phases, where a phase exhibits fracton topological order if its errors can be corrected by finite depth error correction circuits. In other words, the statistical properties encoding the error correction time statistics are bounded in the case of fracton phases while they diverge in the trivial phase. Error correction being central to the operational definition we propose an outline for the same. The error correction strategy for the B_p excitations would involve the parallel detection of the four excited cubes. For the case of A_v violations in the same plane the error correction strategy is

same as in the case of toric code in 2D while it has to be further adapted for efficient detection of A_v violations in and out of plane due to the additional excitations appearing at the bends as in Fig. E.1(b).

E.2 Cubic code model

We consider a 3D cubic lattice with two spin-1/2's placed at the vertices of the cube. The Hamiltonian of the Cubic code model (also known as Haah's code) is given by

$$H_{cc} = - \sum_c (A_c + B_c) \quad (\text{E.3})$$

where A_c, B_c are as defined in Fig. E.2

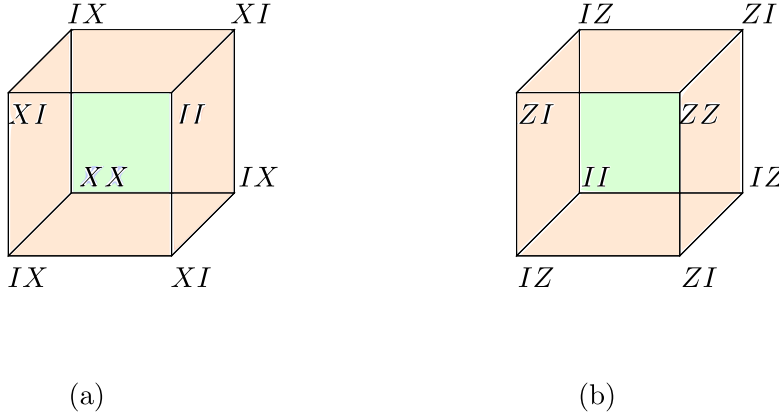


Figure E.2: (a) A_c operator (b) B_c operator

The ground state is given by

$$|\psi\rangle_{cc} = \mathcal{N} \prod_c (1 + B_c)(1 + A_c)|\mathbf{0}\rangle \quad (\text{E.4})$$

with the ground state degeneracy having a lower bound of 4 and upper bound of 2^{4L} . The excitations are given by the action of anti-commutators σ_x and σ_z acting on the spin-1/2's at the vertices and are identified at the center of the cube. These excitations appear four at a time at the corners of a tetrahedron. These models under various perturbation have been recently studied in the Ref. [159] by mapping to Ising models in 3D with the excitations being identified by the Ising spins at the corners of the tetrahedrons. As in the X-cube model, the operational definition can be applied to the current scenario, where we expect that errors in the fracton phase can be corrected by finite

E. Extension of operational definition for fracton order

depth circuits, with the statistical properties of time correction statistics being bounded in the fracton phase while they diverge in the trivial phase. The error correction strategy in the current scenario would involve the detection of tetrahedrons. A sketch of the error detection might be as follows: given the excited cubes, we start with the smallest tetrahedron, as in Fig. E.3(a) and observe if the excited cubes can be annihilated, else we increase the size of tetrahedron, as in Fig. E.3(b) until all the excited cubes are annihilated. The time of detection is captured by the size of tetrahedron.

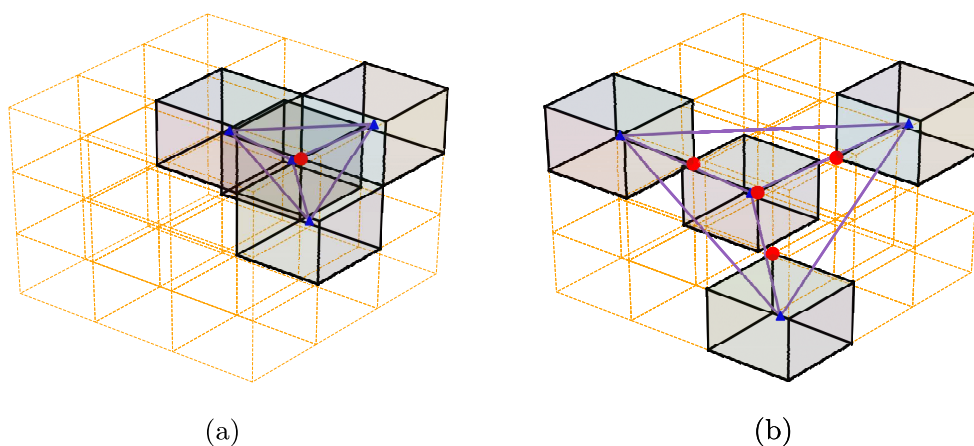


Figure E.3: (a) The excited cubes are situated at the corners of a smaller tetrahedron, which can be detected in a single time step and annihilated by applying σ_z on the first qubit at the vertex denoted by the red dot. (b) The excited cubes are at the corners of a larger tetrahedron, the detection of which requires atleast two time steps and can be annihilated by applying σ_z on the first qubit of the vertices denoted by the red dots.

Bibliography

- [1] X.-G. Wen, Topological order: From long-range entangled quantum matter to a unified origin of light and electrons, *ISRN Condensed Matter Physics 2013* (2013) 1–20. doi:10.1155/2013/198710.
URL <http://dx.doi.org/10.1155/2013/198710>
- [2] L. Landau, On the theory of phase transitions, *Ukr. J. Phys.* 53 (2008) 25–35, originally published in *Zh. Eksp. Teor. Fiz.* **7**, 19–32 (1937).
- [3] M. Cyrot, Ginzburg-landau theory for superconductors, *Rep. Prog. Phys.* 36 (2) (1973) 103–158. doi:10.1088/0034-4885/36/2/001.
URL <https://doi.org/10.1088/0034-4885/36/2/001>
- [4] B. Zeng, X. Chen, D.-L. Zhou, X.-G. Wen, Quantum information meets quantum matter – from quantum entanglement to topological phase in many-body systems (2018). arXiv:1508.02595.
- [5] A. Y. Kitaev, Fault-tolerant quantum computation by anyons, *Ann. Phys. (N. Y.)* 303 (2003) 2–30.
- [6] X.-G. Wen, Modular transformation and bosonic/fermionic topological orders in abelian fractional quantum hall states (2012). arXiv:1212.5121.
- [7] S. Simon, *Topological Quantum: Lecture Notes*, 2016.
URL <http://www-thphys.physics.ox.ac.uk/people/SteveSimon/topological2016/TopoBook.pdf>
- [8] S. Bravyi, M. B. Hastings, S. Michalakis, Topological quantum order: Stability under local perturbations, *Journal of Mathematical Physics* 51 (9) (2010) 093512. arXiv:<https://doi.org/10.1063/1.3490195>, doi:10.1063/1.3490195.
URL <https://doi.org/10.1063/1.3490195>

-
- [9] S. Bravyi, M. B. Hastings, A short proof of stability of topological order under local perturbations, *Communications in Mathematical Physics* 307 (3) (2011) 609–627. doi:10.1007/s00220-011-1346-2.
URL <http://dx.doi.org/10.1007/s00220-011-1346-2>
- [10] S. X. Cui, D. Ding, X. Han, G. Penington, D. Ranard, B. C. Rayhaun, Z. Shangnan, Kitaev’s quantum double model as an error correcting code, *Quantum* 4 (2020) 331. doi:10.22331/q-2020-09-24-331.
URL <https://doi.org/10.22331/q-2020-09-24-331>
- [11] X. Chen, Z.-C. Gu, X.-G. Wen, Local unitary transformation, long-range quantum entanglement, wave function renormalization, and topological order, *Phys. Rev. B* 82 (2010) 155138. doi:10.1103/PhysRevB.82.155138.
URL <https://link.aps.org/doi/10.1103/PhysRevB.82.155138>
- [12] A. Kitaev, J. Preskill, Topological entanglement entropy, *Phys. Rev. Lett.* 96 (2006) 110404. doi:10.1103/PhysRevLett.96.110404.
URL <https://link.aps.org/doi/10.1103/PhysRevLett.96.110404>
- [13] M. Levin, X.-G. Wen, Detecting topological order in a ground state wave function, *Phys. Rev. Lett.* 96 (2006) 110405. doi:10.1103/PhysRevLett.96.110405.
URL <https://link.aps.org/doi/10.1103/PhysRevLett.96.110405>
- [14] H.-C. Jiang, Z. Wang, L. Balents, Identifying topological order by entanglement entropy, *Nature Phys.* 8 (2012) 902–905. doi:10.1038/nphys2465.
- [15] Y. Zhang, T. Grover, A. Turner, M. Oshikawa, A. Vishwanath, Quasi-particle statistics and braiding from ground-state entanglement, *Phys. Rev. B* 85 (2012) 235151. doi:10.1103/PhysRevB.85.235151.
URL <https://link.aps.org/doi/10.1103/PhysRevB.85.235151>
- [16] W. Zhu, D. N. Sheng, F. D. M. Haldane, Minimal entangled states and modular matrix for fractional quantum hall effect in topological flat bands, *Phys. Rev. B* 88 (2013) 035122. doi:10.1103/PhysRevB.88.035122.
URL <https://link.aps.org/doi/10.1103/PhysRevB.88.035122>
- [17] H. He, H. Moradi, X.-G. Wen, Modular matrices as topological order parameter by a gauge-symmetry-preserved tensor renormalization

Bibliography

- approach, Physical Review B 90 (20). doi:10.1103/physrevb.90.205114.
URL <http://dx.doi.org/10.1103/PhysRevB.90.205114>
- [18] S. C. Morampudi, C. von Keyserlingk, F. Pollmann, Numerical study of a transition between F_2 topologically ordered phases, Phys. Rev. B 90 (2014) 035117. doi:10.1103/PhysRevB.90.035117.
URL <https://link.aps.org/doi/10.1103/PhysRevB.90.035117>
- [19] M. Atiyah, Topological quantum field theories, Publications Mathématiques de l'Institut des Hautes Études Scientifiques 68 (1988) 11. doi:10.1007/BF02698547.
URL <https://doi.org/10.1007/BF02698547>
- [20] M. E. Beverland, O. Buerschaper, R. Koenig, F. Pastawski, J. Preskill, S. Sijher, Protected gates for topological quantum field theories, Journal of Mathematical Physics 57 (2) (2016) 022201. doi:10.1063/1.4939783.
URL <http://dx.doi.org/10.1063/1.4939783>
- [21] A. Smith, O. Golan, Z. Ringel, Intrinsic sign problems in topological quantum field theories, Phys. Rev. Research 2 (2020) 033515. doi:10.1103/PhysRevResearch.2.033515.
URL <https://link.aps.org/doi/10.1103/PhysRevResearch.2.033515>
- [22] S. D. Geraedts, Numerical studies of topological phases, California Institute of Technology (7). doi:doi:10.7907/Z9668B3N.
URL <https://resolver.caltech.edu/CaltechTHESIS:05282015-205532544>
- [23] X.-G. Wen, Topological order: From long-range entangled quantum matter to a unified origin of light and electrons, ISRN Cond. Mat. Phys. 2013 (2013) 20.
URL <http://dx.doi.org/10.1155/2013/198710>
- [24] C. Z. Xiong, Classification and construction of topological phases of quantum matter (2019). arXiv:1906.02892.
- [25] E. Dennis, A. Kitaev, A. Landahl, J. Preskill, Topological quantum memory, J. Math. Phys. 43 (9) (2002) 4452–4505. doi:10.1063/1.1499754.

-
- [26] S. Bravyi, Universal quantum computation with the $\nu=5/2$ fractional quantum hall state, *Physical Review A* 73 (2006) 042313.
- [27] C. Nayak, S. H. Simon, A. Stern, M. Freedman, S. Das Sarma, Non-abelian anyons and topological quantum computation, *Rev. Mod. Phys.* 80 (2008) 1083–1159. doi:10.1103/RevModPhys.80.1083.
URL <https://link.aps.org/doi/10.1103/RevModPhys.80.1083>
- [28] Z. Wang, *Topological Quantum Computation*, Vol. 112, American Mathematical Society, 2010.
URL <http://www-thphys.physics.ox.ac.uk/people/SteveSimon/topological2016/TopoBook.pdf>
- [29] J. K. Pachos, *Introduction to Topological Quantum Computation*, Cambridge University Press, 2012. doi:10.1017/CB09780511792908.
- [30] J. K. Pachos, S. H. Simon, Focus on topological quantum computation, *New Journal of Physics* 16 (6) (2014) 065003. doi:10.1088/1367-2630/16/6/065003.
URL <http://dx.doi.org/10.1088/1367-2630/16/6/065003>
- [31] V. Lahtinen, J. K. Pachos, A Short Introduction to Topological Quantum Computation, *SciPost Phys.* 3 (2017) 021. doi:10.21468/SciPostPhys.3.3.021.
URL <https://scipost.org/10.21468/SciPostPhys.3.3.021>
- [32] Z. Wang, Mathematics of topological quantum computing, arxiv.org.
URL <https://www.microsoft.com/en-us/research/publication/mathematics-topological-quantum-computing/>
- [33] H. Bombin, Topological order with a twist: Ising anyons from an abelian model, *Physical Review Letters* 105 (3). doi:10.1103/physrevlett.105.030403.
URL <http://dx.doi.org/10.1103/PhysRevLett.105.030403>
- [34] B. J. Brown, K. Laubscher, M. S. Kesselring, J. R. Wootton, Poking holes and cutting corners to achieve clifford gates with the surface code, *Phys. Rev. X* 7 (2017) 021029. doi:10.1103/PhysRevX.7.021029.
URL <https://link.aps.org/doi/10.1103/PhysRevX.7.021029>
- [35] J. Alicea, Y. Oreg, G. Refael, F. von Oppen, M. P. A. Fisher, Non-abelian statistics and topological quantum information processing in 1d wire networks, *Nature Physics* 7 (5) (2011) 412–417. doi:10.1038/

Bibliography

- nphys1915.
URL <http://dx.doi.org/10.1038/nphys1915>
- [36] R. S. Mong, D. J. Clarke, J. Alicea, N. H. Lindner, P. Fendley, C. Nayak, Y. Oreg, A. Stern, E. Berg, K. Shtengel, et al., Universal topological quantum computation from a superconductor-abelian quantum hall heterostructure, *Physical Review X* 4 (1). doi:10.1103/physrevx.4.011036.
URL <http://dx.doi.org/10.1103/PhysRevX.4.011036>
- [37] C. G. Brell, S. T. Flammia, S. D. Bartlett, A. C. Doherty, Toric codes and quantum doubles from two-body hamiltonians, *New Journal of Physics* 13 (5) (2011) 053039. doi:10.1088/1367-2630/13/5/053039.
URL <http://dx.doi.org/10.1088/1367-2630/13/5/053039>
- [38] S. Bravyi, A. Kitaev, Quantum codes on a lattice with boundary, arXiv:quant-ph/9811052.
URL [arXiv:quant-ph/9811052v1](http://arxiv.org/abs/quant-ph/9811052v1)
- [39] H. Bombin, M. A. Martin-Delgado, Family of non-abelian kitaev models on a lattice: Topological condensation and confinement, *Physical Review B* 78 (11). doi:10.1103/physrevb.78.115421.
URL <http://dx.doi.org/10.1103/PhysRevB.78.115421>
- [40] S. Beigi, P. W. Shor, D. Whalen, The quantum double model with boundary: Condensations and symmetries, *Commun. Math. Phys.* 306 (3) (2011) 663–694. doi:10.1007/s00220-011-1294-x.
URL <https://doi.org/10.1007/s00220-011-1294-x>
- [41] B. Yoshida, Gapped boundaries, group cohomology and fault-tolerant logical gates, *Ann. Phys. (N. Y.)* 377 (Supplement C) (2017) 387 – 413. doi:<https://doi.org/10.1016/j.aop.2016.12.014>.
URL <http://www.sciencedirect.com/science/article/pii/S0003491616302858>
- [42] Y. Hu, Y. Wan, Y.-S. Wu, Boundary hamiltonian theory for gapped topological orders, *Chinese Physics Letters* 34 (2017) 077103.
- [43] I. Cong, M. Cheng, Z. Wang, Topological quantum computation with gapped boundaries and boundary defects, arXiv:1710.07197.
URL <https://arxiv.org/abs/1710.07197>
- [44] I. Cong, M. Cheng, Z. Wang, Universal quantum computation with gapped boundaries, *Phys. Rev. Lett.* 119 (2017) 170504.

- doi:10.1103/PhysRevLett.119.170504.
URL <https://link.aps.org/doi/10.1103/PhysRevLett.119.170504>
- [45] M. S. Kesselring, F. Pastawski, J. Eisert, B. J. Brown, The boundaries and twist defects of the color code and their applications to topological quantum computation, *Quantum* 2 (2018) 101. doi:10.22331/q-2018-10-19-101.
URL <http://dx.doi.org/10.22331/q-2018-10-19-101>
- [46] J. Lou, C. Shen, L. Hung, Ishibashi states, topological orders with boundaries and topological entanglement entropy. part i, *Journal of High Energy Physics* 2019 (2019) 1–34.
- [47] L. Kong, Anyon condensation and tensor categories, *Nuclear Physics B* 886 (2014) 436–482. doi:10.1016/j.nuclphysb.2014.07.003.
URL <http://dx.doi.org/10.1016/j.nuclphysb.2014.07.003>
- [48] F. Burnell, Anyon condensation and its applications, *Annual Review of Condensed Matter Physics* 9 (1) (2018) 307–327. doi:10.1146/annurev-conmatphys-033117-054154.
URL <http://dx.doi.org/10.1146/annurev-conmatphys-033117-054154>
- [49] Y. Hu, Y. Wan, Y.-S. Wu, Twisted quantum double model of topological phases in two dimensions, *Phys. Rev. B* 87 (2013) 125114. doi:10.1103/PhysRevB.87.125114.
URL <https://link.aps.org/doi/10.1103/PhysRevB.87.125114>
- [50] M. A. Levin, X.-G. Wen, String-net condensation: A physical mechanism for topological phases, *Phys. Rev. B* 71 (2005) 045110. doi:10.1103/PhysRevB.71.045110.
URL <https://link.aps.org/doi/10.1103/PhysRevB.71.045110>
- [51] B. J. Brown, W. Son, C. V. Kraus, R. Fazio, V. Vedral, Generating topological order from a two-dimensional cluster state using a duality mapping, *New Journal of Physics* 13 (6) (2011) 065010. doi:10.1088/1367-2630/13/6/065010.
URL <https://doi.org/10.1088%2F1367-2630%2F13%2F6%2F065010>
- [52] A. G. Fowler, M. Mariantoni, J. M. Martinis, A. N. Cleland, Surface codes: Towards practical large-scale quantum computation, *Phys. Rev. A* 86 (2012) 032324. doi:10.1103/PhysRevA.86.032324.
URL <http://link.aps.org/doi/10.1103/PhysRevA.86.032324>

Bibliography

- [53] A. Kitaev, L. Kong, Models for gapped boundaries and domain walls, *Commun. Math. Phys.* 313 (2) (2012) 351–373. doi:10.1007/s00220-012-1500-5.
URL <https://doi.org/10.1007/s00220-012-1500-5>
- [54] A. Bullivant, Y. Hu, Y. Wan, Twisted quantum double model of topological order with boundaries, *Physical Review B* 96 (16). doi:10.1103/physrevb.96.165138.
URL <http://dx.doi.org/10.1103/PhysRevB.96.165138>
- [55] D. Bulmash, T. Iadecola, Braiding and gapped boundaries in fracton topological phases, *Physical Review B* 99 (2018) 125132.
- [56] S. Trebst, P. Werner, M. Troyer, K. Shtengel, C. Nayak, Break-down of a topological phase: Quantum phase transition in a loop gas model with tension, *Phys. Rev. Lett.* 98 (2007) 070602. doi:10.1103/PhysRevLett.98.070602.
URL <http://link.aps.org/doi/10.1103/PhysRevLett.98.070602>
- [57] A. Hamma, D. A. Lidar, Adiabatic preparation of topological order, *Phys. Rev. Lett.* 100 (2008) 030502. doi:10.1103/PhysRevLett.100.030502.
URL <https://link.aps.org/doi/10.1103/PhysRevLett.100.030502>
- [58] S. Dusuel, M. Kamfor, R. Orús, K. P. Schmidt, J. Vidal, Robustness of a perturbed topological phase, *Phys. Rev. Lett.* 106 (2011) 107203. doi:10.1103/PhysRevLett.106.107203.
URL <https://link.aps.org/doi/10.1103/PhysRevLett.106.107203>
- [59] C. Castelnovo, C. Chamon, Quantum topological phase transition at the microscopic level, *Phys. Rev. B* 77 (2008) 054433. doi:10.1103/PhysRevB.77.054433.
URL <https://link.aps.org/doi/10.1103/PhysRevB.77.054433>
- [60] J. Vidal, S. Dusuel, K. P. Schmidt, Low-energy effective theory of the toric code model in a parallel magnetic field, *Phys. Rev. B* 79 (3) (2009) 033109. doi:10.1103/PhysRevB.79.033109.
- [61] F. Wu, Y. Deng, N. Prokof'ev, Phase diagram of the toric code model in a parallel magnetic field, *Phys. Rev. B* 85 (2012) 195104. doi:10.1103/PhysRevB.85.195104.
URL <https://link.aps.org/doi/10.1103/PhysRevB.85.195104>

-
- [62] H. Weimer, M. Müller, I. Lesanovsky, P. Zoller, H. P. Büchler, A rydberg quantum simulator, *Nature Phys.* 6 (2010) 382–388. doi:10.1038/NPHYS1614.
- [63] M. Sameti, A. Potočnik, D. E. Browne, A. Wallraff, M. J. Hartmann, Superconducting quantum simulator for topological order and the toric code, *Phys. Rev. A* 95 (2017) 042330. doi:10.1103/PhysRevA.95.042330.
URL <https://link.aps.org/doi/10.1103/PhysRevA.95.042330>
- [64] L. Tagliacozzo, G. Vidal, Entanglement renormalization and gauge symmetry, *Phys. Rev. B* 83 (2011) 115127. doi:10.1103/PhysRevB.83.115127.
URL <https://link.aps.org/doi/10.1103/PhysRevB.83.115127>
- [65] M. Schuler, S. Whitsitt, L.-P. Henry, S. Sachdev, A. M. Läuchli, Universal signatures of quantum critical points from finite-size torus spectra: A window into the operator content of higher-dimensional conformal field theories, *Phys. Rev. Lett.* 117 (2016) 210401. doi:10.1103/PhysRevLett.117.210401.
URL <https://link.aps.org/doi/10.1103/PhysRevLett.117.210401>
- [66] J. L. Cardy, *Scaling and Renormalization in Statistical Physics*, Cambridge University Press, Cambridge, 1996.
- [67] S. Sachdev, *Quantum Phase Transitions*, Cambridge University Press, Cambridge, 1999.
- [68] J. C. Wang, X.-G. Wen, Boundary degeneracy of topological order, *Phys. Rev. B* 91 (2015) 125124. doi:10.1103/PhysRevB.91.125124.
URL <https://link.aps.org/doi/10.1103/PhysRevB.91.125124>
- [69] C. Chen, L.-Y. Hung, Y. Li, Y. Wan, Entanglement entropy of topological orders with boundaries, arXiv:1804.05725.
URL <https://arxiv.org/abs/1804.05725>
- [70] M. H. Zarei, Quantum phase transition from $z_2 \times z_2$ to z_2 topological order, *Physical Review A* 93 (4). doi:10.1103/physreva.93.042306.
URL <http://dx.doi.org/10.1103/PhysRevA.93.042306>
- [71] Y. Hu, Y. Wan, Y.-S. Wu, From effective hamiltonian to anomaly inflow in topological orders with boundaries, *Journal of High Energy Physics*

Bibliography

- 2018 (8). doi:10.1007/jhep08(2018)092.
URL [http://dx.doi.org/10.1007/JHEP08\(2018\)092](http://dx.doi.org/10.1007/JHEP08(2018)092)
- [72] M. Iqbal, K. Duivenvoorden, N. Schuch, Study of anyon condensation and topological phase transitions from a z_4 topological phase using the projected entangled pair states approach, *Physical Review B* 97 (19). doi:10.1103/physrevb.97.195124.
URL <http://dx.doi.org/10.1103/PhysRevB.97.195124>
- [73] C. Castelnovo, S. Trebst, M. Troyer, Topological order and quantum criticality, *Understanding Quantum Phase Transitions* (2010) 169–192 doi:10.1201/b10273-10.
URL <http://dx.doi.org/10.1201/b10273-10>
- [74] B. Yoshida, Classification of quantum phases and topology of logical operators in an exactly solved model of quantum codes, *Annals of Physics* 326 (1) (2011) 15–95. doi:10.1016/j.aop.2010.10.009.
URL <http://dx.doi.org/10.1016/j.aop.2010.10.009>
- [75] J. C. Y. Teo, Globally symmetric topological phase: from anyonic symmetry to twist defect, *Journal of Physics: Condensed Matter* 28 (14) (2016) 143001. doi:10.1088/0953-8984/28/14/143001.
URL <http://dx.doi.org/10.1088/0953-8984/28/14/143001>
- [76] S. Diehl, A. Micheli, A. Kantian, B. Kraus, H. P. Büchler, P. Zoller, Quantum states and phases in driven open quantum systems with cold atoms, *Nature Phys.* 4 (2008) 878–883.
- [77] F. Verstraete, M. M. Wolf, J. Ignacio Cirac, Quantum computation and quantum-state engineering driven by dissipation, *Nature Phys.* 5 (9) (2009) 633–636. doi:10.1038/nphys1342.
- [78] G. Dagvadorj, J. M. Fellows, S. Matyjaśkiewicz, F. M. Marchetti, I. Carusotto, M. H. Szymańska, Nonequilibrium phase transition in a two-dimensional driven open quantum system, *Phys. Rev. X* 5 (2015) 041028. doi:10.1103/PhysRevX.5.041028.
URL <https://link.aps.org/doi/10.1103/PhysRevX.5.041028>
- [79] H. Weimer, Variational principle for steady states of dissipative quantum many-body systems, *Phys. Rev. Lett.* 114 (2015) 040402. doi:10.1103/PhysRevLett.114.040402.

-
- [80] V. R. Overbeck, M. F. Maghrebi, A. V. Gorshkov, H. Weimer, Multi-critical behavior in dissipative Ising models, arXiv:1606.08863arXiv:1606.08863.
- [81] M. Raghunandan, J. Wrachtrup, H. Weimer, High-density quantum sensing with dissipative first order transitions, Phys. Rev. Lett. 120 (2018) 150501. doi:10.1103/PhysRevLett.120.150501.
URL <https://link.aps.org/doi/10.1103/PhysRevLett.120.150501>
- [82] S. Helmrich, A. Arias, S. Whitlock, Uncovering the nonequilibrium phase structure of an open quantum spin system, Physical Review A 98 (2). doi:10.1103/physreva.98.022109.
URL <http://dx.doi.org/10.1103/PhysRevA.98.022109>
- [83] P. Cappellaro, Lecture notes: Quantum theory of radiation interactions, mit fall 2012.
URL <https://ocw.mit.edu/courses/nuclear-engineering/22-51-quantum-theory-of-radiation-interactions-fall-2012/lecture-notes/>
- [84] H.-P. Breuer, F. Petruccione, The Theory of Open Quantum Systems, Oxford University Press, Oxford, 2002.
- [85] J. Johansson, P. Nation, F. Nori, Qutip 2: A python framework for the dynamics of open quantum systems, Comp. Phys. Comm. 184 (4) (2013) 1234–1240. doi:http://dx.doi.org/10.1016/j.cpc.2012.11.019.
URL <http://www.sciencedirect.com/science/article/pii/S0010465512003955>
- [86] A. Langari, A. Mohammad-Aghaei, R. Haghshenas, Quantum phase transition as an interplay of kitaev and ising interactions, Physical Review B 91 (2). doi:10.1103/physrevb.91.024415.
URL <http://dx.doi.org/10.1103/PhysRevB.91.024415>
- [87] L. Zou, J. Haah, Spurious long-range entanglement and replica correlation length, Physical Review B 94 (7). doi:10.1103/physrevb.94.075151.
URL <http://dx.doi.org/10.1103/PhysRevB.94.075151>
- [88] T. Grover, A. M. Turner, A. Vishwanath, Entanglement entropy of gapped phases and topological order in three dimensions, Phys. Rev.

Bibliography

- B 84 (2011) 195120. doi:10.1103/PhysRevB.84.195120.
URL <https://link.aps.org/doi/10.1103/PhysRevB.84.195120>
- [89] J. Cano, T. L. Hughes, M. Mulligan, Interactions along an entanglement cut in $2+1$ dabelian topological phases, *Physical Review B* 92 (7). doi:10.1103/physrevb.92.075104.
URL <http://dx.doi.org/10.1103/PhysRevB.92.075104>
- [90] L. H. Santos, J. Cano, M. Mulligan, T. L. Hughes, Symmetry-protected topological interfaces and entanglement sequences, *Physical Review B* 98 (7). doi:10.1103/physrevb.98.075131.
URL <http://dx.doi.org/10.1103/PhysRevB.98.075131>
- [91] D. J. Williamson, A. Dua, M. Cheng, Spurious topological entanglement entropy from subsystem symmetries, *Physical Review Letters* 122 (14). doi:10.1103/physrevlett.122.140506.
URL <http://dx.doi.org/10.1103/PhysRevLett.122.140506>
- [92] C. E. Mora, H. J. Briegel, B. Kraus, Quantum kolmogorov complexity and its applications, *Int. J. Quant. Inf.* 05 (05) (2007) 729–750. arXiv:<https://doi.org/10.1142/S0219749907003171>, doi:10.1142/S0219749907003171.
URL <https://doi.org/10.1142/S0219749907003171>
- [93] M. B. Hastings, Topological order at nonzero temperature, *Physical Review Letters* 107 (21). doi:10.1103/physrevlett.107.210501.
URL <http://dx.doi.org/10.1103/PhysRevLett.107.210501>
- [94] C.-E. Bardyn, M. A. Baranov, C. V. Kraus, E. Rico, A. İmamoğlu, P. Zoller, S. Diehl, Topology by dissipation, *New J. Phys.* 15 (8) (2013) 085001. doi:10.1088/1367-2630/15/8/085001.
- [95] O. Viyuela, A. Rivas, M. A. Martin-Delgado, Two-dimensional density-matrix topological fermionic phases: Topological uhlmann numbers, *Phys. Rev. Lett.* 113 (2014) 076408. doi:10.1103/PhysRevLett.113.076408.
URL <https://link.aps.org/doi/10.1103/PhysRevLett.113.076408>
- [96] Z. Huang, D. P. Arovas, Topological indices for open and thermal systems via uhlmann’s phase, *Phys. Rev. Lett.* 113 (2014) 076407. doi:10.1103/PhysRevLett.113.076407.
URL <https://link.aps.org/doi/10.1103/PhysRevLett.113.076407>

-
- [97] F. Grusdt, Topological order of mixed states in correlated quantum many-body systems, *Phys. Rev. B* 95 (2017) 075106. doi:10.1103/PhysRevB.95.075106.
URL <https://link.aps.org/doi/10.1103/PhysRevB.95.075106>
- [98] C. Brell, What is topological order? (2017).
URL <http://www.physics.usyd.edu.au/quantum/Coogee2017/Presentations/CBrell.pdf>
- [99] H. Hinrichsen, Non-equilibrium critical phenomena and phase transitions into absorbing states, *Adv. Phys.* 49 (2000) 815–958.
- [100] M. Henkel, H. Hinrichsen, S. L. Lubbe, Directed Percolation, Springer Netherlands, Dordrecht, 2008, pp. 59–100. doi:10.1007/978-1-4020-8765-3_3.
URL https://doi.org/10.1007/978-1-4020-8765-3_3
- [101] G. Lemoult, L. Shi, K. Avila, S. V. Jalikop, M. Avila, B. Hof, Directed percolation phase transition to sustained turbulence in Couette flow, *Nature Physics* 12 (3) (2016) 254–258. doi:10.1038/nphys3675.
- [102] G. Ódor, Critical branching-annihilating random walk of two species, *Phys. Rev. E* 63 (2001) 021113. doi:10.1103/PhysRevE.63.021113.
URL <https://link.aps.org/doi/10.1103/PhysRevE.63.021113>
- [103] T. J. Osborne, Topological order for mixed states (2013).
URL <https://tjoresearchnotes.wordpress.com/2013/05/29/topological-order-for-mixed-states/>
- [104] F. Carollo, E. Gillman, H. Weimer, I. Lesanovsky, Critical behavior of the quantum contact process in one dimension, *Phys. Rev. Lett.* 123 (2019) 100604. doi:10.1103/PhysRevLett.123.100604.
URL <https://link.aps.org/doi/10.1103/PhysRevLett.123.100604>
- [105] J. L. Cardy, Field theory of branching and annihilating random walks, *Journal of Statistical Physics* 90 (1/2) (1998) 1–56. doi:10.1023/a:1023233431588.
URL <http://dx.doi.org/10.1023/A:1023233431588>
- [106] C. L. Kane, E. J. Mele, Quantum spin hall effect in graphene, *Physical Review Letters* 95 (22). doi:10.1103/physrevlett.95.226801.
URL <http://dx.doi.org/10.1103/PhysRevLett.95.226801>

Bibliography

- [107] J. Moore, The birth of topological insulators, *Nature* 464 (2010) 194–198.
- [108] M. Z. Hasan, C. L. Kane, Colloquium: Topological insulators, *Rev. Mod. Phys.* 82 (2010) 3045–3067. doi:10.1103/RevModPhys.82.3045
URL <https://link.aps.org/doi/10.1103/RevModPhys.82.3045>
- [109] B. A. BERNEVIG, T. L. Hughes, *Topological Insulators and Topological Superconductors*, student edition Edition, Princeton University Press, 2013.
URL <http://www.jstor.org/stable/j.ctt19cc2gc>
- [110] W. Su, J. Schrieffer, A. Heeger, Soliton excitations in polyacetylene, *Phys. Rev. B* 22 (1980) 2099–2111. doi:10.1103/PhysRevB.22.2099.
- [111] E. J. Meier, F. An, B. Gadway, Observation of the topological soliton state in the su–schrieffer–heeger model, *Nature Communications* 7.
- [112] J. K. Asbóth, L. Oroszlány, A. Pályi, *A short course on topological insulators*, *Lecture Notes in Physics*doi:10.1007/978-3-319-25607-8.
URL <http://dx.doi.org/10.1007/978-3-319-25607-8>
- [113] K. Hida, Crossover between the haldane-gap phase and the dimer phase in the spin-1/2 alternating heisenberg chain, *Phys. Rev. B* 45 (1992) 2207–2212. doi:10.1103/PhysRevB.45.2207.
URL <https://link.aps.org/doi/10.1103/PhysRevB.45.2207>
- [114] S. de Léséleuc, V. Lienhard, P. Scholl, D. Barredo, S. Weber, N. Lang, H. P. Büchler, T. Lahaye, A. Browaeys, Observation of a symmetry-protected topological phase of interacting bosons with rydberg atoms, *Science* 365 (6455) (2019) 775–780. doi:10.1126/science.aav9105.
URL <http://dx.doi.org/10.1126/science.aav9105>
- [115] Y. Huang, X. Chen, Quantum circuit complexity of one-dimensional topological phases, *Physical Review B* 91 (19). doi:10.1103/physrevb.91.195143.
URL <http://dx.doi.org/10.1103/PhysRevB.91.195143>
- [116] N. Batra, G. Sheet, Physics with coffee and doughnuts, *Resonance* 25 (6) (2020) 765–786. doi:10.1007/s12045-020-0995-x.
URL <http://dx.doi.org/10.1007/s12045-020-0995-x>
- [117] F. Roser, *Symmetry Protected Topological Phases for Interacting Bosons*, 2020.

- URL https://www.itp3.uni-stuttgart.de/downloads/theses/Roser_-_2019_-_Symmetry_Protected_Topological_Phases_for_Interacting_Bosons.pdf
- [118] M. Fishman, S. R. White, E. M. Stoudenmire, The itensor software library for tensor network calculations (2020). [arXiv:2007.14822](https://arxiv.org/abs/2007.14822).
- [119] Z.-Y. Han, J. Wang, H. Fan, L. Wang, P. Zhang, Unsupervised generative modeling using matrix product states, *Phys. Rev. X* 8 (2018) 031012. [doi:10.1103/PhysRevX.8.031012](https://doi.org/10.1103/PhysRevX.8.031012).
URL <https://link.aps.org/doi/10.1103/PhysRevX.8.031012>
- [120] A. Elben, J. Yu, G. Zhu, M. Hafezi, F. Pollmann, P. Zoller, B. Vermersch, Many-body topological invariants from randomized measurements in synthetic quantum matter, *Science Advances* 6 (15). [arXiv:https://advances.sciencemag.org/content/6/15/eaaz3666.full.pdf](https://arxiv.org/abs/https://advances.sciencemag.org/content/6/15/eaaz3666.full.pdf), [doi:10.1126/sciadv.aaz3666](https://doi.org/10.1126/sciadv.aaz3666).
URL <https://advances.sciencemag.org/content/6/15/eaaz3666>
- [121] A. Micheli, G. K. Brennen, P. Zoller, A toolbox for lattice-spin models with polar molecules, *Nature Phys.* 2 (2006) 341–347. [arXiv:arXiv:quant-ph/0512222](https://arxiv.org/abs/quant-ph/0512222), [doi:10.1038/nphys287](https://doi.org/10.1038/nphys287).
- [122] M. Aguado, G. K. Brennen, F. Verstraete, J. I. Cirac, Creation, manipulation, and detection of abelian and non-abelian anyons in optical lattices, *Phys. Rev. Lett.* 101 (26) (2008) 260501. [doi:10.1103/PhysRevLett.101.260501](https://doi.org/10.1103/PhysRevLett.101.260501).
URL <http://link.aps.org/abstract/PRL/v101/e260501>
- [123] B. P. Lanyon, C. Hempel, D. Nigg, M. Müller, R. Gerritsma, F. Zähringer, P. Schindler, J. T. Barreiro, M. Rambach, G. Kirchmair, M. Hennrich, P. Zoller, R. Blatt, C. F. Roos, Universal Digital Quantum Simulation with Trapped Ions, *Science* 334 (2011) 57–. [arXiv:1109.1512](https://arxiv.org/abs/1109.1512), [doi:10.1126/science.1208001](https://doi.org/10.1126/science.1208001).
- [124] J. T. Barreiro, M. Müller, P. Schindler, D. Nigg, T. Monz, M. Chwalla, M. Hennrich, C. F. Roos, P. Zoller, R. Blatt, An open-system quantum simulator with trapped ions, *Nature* 470 (2011) 486.
- [125] H. Weimer, Quantum simulation of many-body spin interactions with ultracold polar molecules, *Mol. Phys.* 111 (12-13) (2013) 1753–1758. [arXiv:http://www.tandfonline.com/doi/pdf/10.1080/00268976.2013.789567](https://arxiv.org/abs/http://www.tandfonline.com/doi/pdf/10.1080/00268976.2013.789567), [doi:10.1080/00268976.2013.789567](https://doi.org/10.1080/00268976.2013.789567).

Bibliography

- URL <http://www.tandfonline.com/doi/abs/10.1080/00268976.2013.789567>
- [126] G. K. Brennen, M. Aguado, J. I. Cirac, Simulations of quantum double models, *New Journal of Physics* 11 (5) (2009) 053009. doi:10.1088/1367-2630/11/5/053009.
URL <http://dx.doi.org/10.1088/1367-2630/11/5/053009>
- [127] B. Gadway, B. Yan, Strongly interacting ultracold polar molecules, *Journal of Physics B: Atomic, Molecular and Optical Physics* 49 (15) (2016) 152002. doi:10.1088/0953-4075/49/15/152002.
URL <http://dx.doi.org/10.1088/0953-4075/49/15/152002>
- [128] S. A. Moses, J. P. Covey, M. T. Miecnikowski, D. S. Jin, J. Ye, New frontiers for quantum gases of polar molecules, *Nature Phys.* 13 (1) (2017) 13–20. arXiv:1610.07711, doi:10.1038/nphys3985.
- [129] A. Kruckenhauser, L. M. Sieberer, L. De Marco, J.-R. Li, K. Matsuda, W. G. Tobias, G. Valtolina, J. Ye, A. M. Rey, M. A. Baranov, P. Zoller, Quantum many-body physics with ultracold polar molecules: Nanostructured potential barriers and interactions, *Phys. Rev. A* 102 (2020) 023320. doi:10.1103/PhysRevA.102.023320.
URL <https://link.aps.org/doi/10.1103/PhysRevA.102.023320>
- [130] J. L. Bohn, A. M. Rey, J. Ye, Cold molecules: Progress in quantum engineering of chemistry and quantum matter, *Science* 357 (6355) (2017) 1002–1010. arXiv:<https://science.sciencemag.org/content/357/6355/1002.full.pdf>, doi:10.1126/science.aam6299.
URL <https://science.sciencemag.org/content/357/6355/1002>
- [131] I. Bloch, J. Dalibard, S. Nascimbène, Quantum simulations with ultracold quantum gases, *Nature Physics* 8 (2012) 267–276.
- [132] J. Doyle, B. Friedrich, R. V. Krems, F. Masnou-Seeuws, Editorial: Quo vadis, cold molecules?, *The European Physical Journal D* 31 (2) (2004) 149–164. doi:10.1140/epjd/e2004-00151-x.
URL <http://dx.doi.org/10.1140/epjd/e2004-00151-x>
- [133] S. Ospelkaus, K.-K. Ni, G. Quéméner, B. Neyenhuis, D. Wang, M. H. G. de Miranda, J. L. Bohn, J. Ye, D. S. Jin, Controlling the hyperfine state of rovibronic ground-state polar molecules, *Phys. Rev. Lett.* 104 (2010) 030402.

-
- [134] D. S., J. Ye, Polar molecules in the quantum regime, *Physics Today* 64 (2011) 27–31. doi:10.1063/1.3592002.
URL <https://doi.org/10.1063/1.3592002>
- [135] S. Ospelkaus, K.-K. Ni, D. Wang, M. H. G. de Miranda, B. Neyenhuis, G. Quémener, P. S. Julienne, J. L. Bohn, D. S. Jin, J. Ye, Quantum-State Controlled Chemical Reactions of Ultracold Potassium-Rubidium Molecules, *Science* 327 (2010) 853–. arXiv:0912.3854, doi:10.1126/science.1184121.
- [136] K. K. Voges, P. Gersema, T. Hartmann, T. A. Schulze, A. Zenesini, S. Ospelkaus, A pathway to ultracold bosonic $^{23}\text{Na}^{39}\text{K}$ ground state molecules, *New Journal of Physics* 21 (12) (2019) 123034. doi:10.1088/1367-2630/ab5f31.
URL <https://doi.org/10.1088/1367-2630/ab5f31>
- [137] K. K. Voges, P. Gersema, M. Meyer zum Alten Borgloh, T. A. Schulze, T. Hartmann, A. Zenesini, S. Ospelkaus, Ultracold gas of bosonic $^{23}\text{Na}^{39}\text{K}$ ground-state molecules, *Phys. Rev. Lett.* 125 (2020) 083401. doi:10.1103/PhysRevLett.125.083401.
URL <https://link.aps.org/doi/10.1103/PhysRevLett.125.083401>
- [138] Z. Idziaszek, P. S. Julienne, Universal rate constants for reactive collisions of ultracold molecules, *Phys. Rev. Lett.* 104 (2010) 113202. doi:10.1103/PhysRevLett.104.113202.
URL <https://link.aps.org/doi/10.1103/PhysRevLett.104.113202>
- [139] W. S. Bakr, J. I. Gillen, A. Peng, S. Fölling, M. Greiner, A quantum gas microscope for detecting single atoms in a Hubbard-regime optical lattice, *nat* 462 (2009) 74–77. doi:10.1038/nature08482.
- [140] J. F. Sherson, C. Weitenberg, M. Endres, M. Cheneau, I. Bloch, S. Kuhr, Single-atom-resolved fluorescence imaging of an atomic Mott insulator, *Nature* 467 (2010) 68–72. doi:10.1038/nature09378.
- [141] B. Zhu, B. Gadway, M. Foss-Feig, J. Schachenmayer, M. Wall, K. Hazard, B. Yan, S. Moses, J. Covey, D. Jin, et al., Suppressing the loss of ultracold molecules via the continuous quantum zeno effect, *Physical Review Letters* 112 (7). doi:10.1103/physrevlett.112.070404.
URL <http://dx.doi.org/10.1103/PhysRevLett.112.070404>

Bibliography

- [142] A. Jamadagni, S. Ospelkaus, L. Santos, H. Weimer, Quantum zeno-based detection and state engineering of ultracold polar molecules (2019). [arXiv:1906.09263](https://arxiv.org/abs/1906.09263).
- [143] C.-Y. Lu, W.-B. Gao, O. Gühne, X.-Q. Zhou, Z.-B. Chen, J.-W. Pan, Demonstrating anyonic fractional statistics with a six-qubit quantum simulator, *Phys. Rev. Lett.* 102 (2009) 030502. doi:10.1103/PhysRevLett.102.030502.
URL <http://link.aps.org/doi/10.1103/PhysRevLett.102.030502>
- [144] D. I. Tsomokos, A. Hamma, W. Zhang, S. Haas, R. Fazio, Topological order following a quantum quench, *Phys. Rev. A* 80 (2009) 060302. doi:10.1103/PhysRevA.80.060302.
URL <https://link.aps.org/doi/10.1103/PhysRevA.80.060302>
- [145] M. Heyl, Dynamical quantum phase transitions: a review, *Reports on Progress in Physics* 81 (5) (2018) 054001. doi:10.1088/1361-6633/aaaf9a.
URL <http://dx.doi.org/10.1088/1361-6633/aaaf9a>
- [146] V. Srivastav, U. Bhattacharya, A. Dutta, Dynamical quantum phase transitions in extended toric-code models, *Physical Review B* 100 (14). doi:10.1103/physrevb.100.144203.
URL <http://dx.doi.org/10.1103/PhysRevB.100.144203>
- [147] A. Chandran, F. J. Burnell, V. Khemani, S. L. Sondhi, Kibble–zurek scaling and string-net coarsening in topologically ordered systems, *Journal of Physics: Condensed Matter* 25 (40) (2013) 404214. doi:10.1088/0953-8984/25/40/404214.
URL <http://dx.doi.org/10.1088/0953-8984/25/40/404214>
- [148] S.-F. Liou, K. Yang, Quench dynamics across topological quantum phase transitions, *Physical Review B* 97 (23). doi:10.1103/physrevb.97.235144.
URL <http://dx.doi.org/10.1103/PhysRevB.97.235144>
- [149] F. Wilczek, Quantum time crystals, *Physical Review Letters* 109 (16). doi:10.1103/physrevlett.109.160401.
URL <http://dx.doi.org/10.1103/PhysRevLett.109.160401>
- [150] V. Khemani, C. W. von Keyserlingk, S. L. Sondhi, Defining time crystals via representation theory, *Physical Review B* 96 (11). doi:

- 10.1103/physrevb.96.115127.
URL <http://dx.doi.org/10.1103/PhysRevB.96.115127>
- [151] F. Liu, S. Whitsitt, J. B. Curtis, R. Lundgren, P. Titum, Z.-C. Yang, J. R. Garrison, A. V. Gorshkov, Circuit complexity across a topological phase transition, *Phys. Rev. Research* 2 (2020) 013323. doi:10.1103/PhysRevResearch.2.013323.
URL <https://link.aps.org/doi/10.1103/PhysRevResearch.2.013323>
- [152] A. Riera-Campenya, M. Moreno-Cardoner, A. Sanpera, Time crystallinity in open quantum systems, *Quantum* 4 (2020) 270. doi:10.22331/q-2020-05-25-270.
URL <http://dx.doi.org/10.22331/q-2020-05-25-270>
- [153] C. Kokail, C. Maier, R. van Bijnen, T. Brydges, M. K. Joshi, P. Jurcevic, C. A. Muschik, P. Silvi, R. Blatt, C. F. Roos, P. Zoller, Self-verifying variational quantum simulation of lattice models, *Nature* 569 (2019) 355–360. doi:10.1038/s41586-019-1177-4.
URL <https://doi.org/10.1038/s41586-019-1177-4>
- [154] D.-L. Deng, X. Li, S. Das Sarma, Machine learning topological states, *Physical Review B* 96 (19). doi:10.1103/physrevb.96.195145.
URL <http://dx.doi.org/10.1103/PhysRevB.96.195145>
- [155] I. Cong, S. Choi, M. D. Lukin, Quantum convolutional neural networks, *Nature Physics* 15 (12) (2019) 1273–1278. doi:10.1038/s41567-019-0648-8.
URL <http://dx.doi.org/10.1038/s41567-019-0648-8>
- [156] K. Beer, D. Bondarenko, T. Farrelly, T. J. Osborne, R. Salzmann, D. Scheiermann, R. Wolf, Training deep quantum neural networks, *Nature Communications* 11 (1). doi:10.1038/s41467-020-14454-2.
URL <http://dx.doi.org/10.1038/s41467-020-14454-2>
- [157] R. M. Nandkishore, M. Hermele, Fractons, *Annual Review of Condensed Matter Physics* 10 (1) (2019) 295–313. doi:10.1146/annurev-conmatphys-031218-013604.
URL <http://dx.doi.org/10.1146/annurev-conmatphys-031218-013604>
- [158] M. Pretko, X. Chen, Y. You, Fracton phases of matter, *International Journal of Modern Physics A* 35 (06) (2020) 2030003. doi:10.1142/S0217751x20300033.
URL <http://dx.doi.org/10.1142/S0217751X20300033>

Bibliography

- [159] M. Mühlhauser, M. R. Walther, D. A. Reiss, K. P. Schmidt, Quantum robustness of fracton phases, *Phys. Rev. B* 101 (2020) 054426. doi: 10.1103/PhysRevB.101.054426.
URL <https://link.aps.org/doi/10.1103/PhysRevB.101.054426>
- [160] J. M. Oberreuter, S. Kehrein, Representation of excited states and topological order of the toric code in mera (2015). arXiv:1510.08126.

*Dedicated
to
Shunya and Purna*

Publications

Parts of the content of this thesis has been published previously in the following manuscripts:

- Amit Jamadagni and Hendrik Weimer
"An Operational Definition of Topological Order"
Submitted (arxiv:2005.06501)
- Amit Jamadagni and Arpan Bhattacharyya
"Topological Phase Transitions Induced by Varying Topology and Boundaries in the Toric Code"
Submitted (arxiv:2004.03614)
- Amit Jamadagni, Silke Ospelkaus, Luis Santos and Hendrik Weimer
"Quantum Zeno-based Detection and State Engineering of Ultracold Polar Molecules"
Submitted (arxiv:1906.09263)
- Amit Jamadagni, Hendrik Weimer and Arpan Bhattacharyya
"Robustness of topological order in the toric code with open boundaries"
Physical Review B (arxiv:1804.09718)

Contents of Chap. 7 will be published in the following manuscript which is currently in preparation:

- Amit Jamadagni and Hendrik Weimer
"Error Correction Statistics as a probe for detecting phase transitions in SPT phases"
(to be submitted)

Curriculum Vitae

Amit Jamadagni Gangapuram
Limmerst. 2D,
30451 Hannover,
Lower Saxony, Germany

Email: amit.jamadagni@itp.uni-hannover.de
Mobile: +49 15207561611

Personal details

Date of birth	:	04.09.1992
Place of birth	:	Hyderabad, India
Gender	:	Male
Nationality	:	Indian

Education

since Nov 2016	:	Doctoral student in Physics, Leibniz University Hannover
2012 - 2016	:	B.E.Electronics and Electrical, BITS Pilani, India
2011 - 2016	:	M.Sc.Mathematics, BITS Pilani, India
2008 - 2010	:	Pre-University College, Hyderabad, India

Selbstständigkeitserklärung

Hiermit versichere ich, die vorliegende Doktorarbeit selbstständig und unter ausschließlicher Verwendung der angegebenen Hilfsmittel angefertigt zu haben.

Amit Jamadagni Gangapuram

Hannover, Jan 2021